

Grid and Inverter-Fed Induction Machine Emulation

Seyedeh Nazanin Afrasiabi

A Thesis

in

The Department

of

Electrical and Computer Engineering

Presented in Partial Fulfillment of the Requirements

For the Degree of

Doctor of Philosophy of Applied Science (Electrical and Computer
Engineering) at

Concordia University

Montréal, Québec, Canada

December 2024

© Seyedeh Nazanin Afrasiabi, 2024

CONCORDIA UNIVERSITY
SCHOOL OF GRADUATE STUDIES

This is to certify that the thesis prepared

By: Seyedeh Nazanin Afrasiabi

Entitled: Grid and Inverter-Fed Induction Machine Emulation

and submitted in partial fulfillment of the requirements for the degree of

Doctor of Philosophy (Electrical and Computer Engineering)

complies with the regulations of this University and meets the accepted standards with respect to originality and quality.

Signed by the final examining committee:

_____ Chair
Dr. Jassim Hassan

_____ External Examiner
Dr. Raghav Khanna

_____ External to Program
Dr. Ramin Sedaghati

_____ Examiner
Dr. Luiz. A. C. Lopes

_____ Examiner
Dr. Shahin Hashtrudi Zad

_____ Thesis Supervisor
Dr. Chunyan Lai

_____ Thesis Supervisor
Dr. Pragasen Pillay

Approved by: _____

Dr. Jun Cai, Graduate Program Director

December 5, 2024 _____

Dr. Mourad Debbabi, Dean,
Gina Cody School of Engineering and Computer Science

ABSTRACT

Grid and Inverter-Fed Induction Machine Emulation

Seyedeh Nazanin Afrasiabi, Ph.D.

Concordia University, 2024

Power-hardware-in-the-loop (PHIL) based machine emulation is increasingly being used as an effective approach for simplifying the testing of electric drive systems. The PHIL-based machine emulator systems control the power converters or power amplifiers in order to mimic machine behavior. Control of the machine emulator is achieved with the help of a machine model running on a real-time controller. Utilizing a motor emulator allows performance testing of the physical machine and its controller before the manufacturing process, reducing risks and costs. This methodology enables testing of different drive inverter faults, including diode rectifier faults, transistor switch faults, and line-to-line faults, without risking damage to the machine. Moreover, it can be applied to test various faulty machines and grid faults, such as open circuits, short circuits, and unbalanced faults. Therefore, this approach finds extensive application in diverse industrial sectors, including military, aerospace, and electric vehicles.

Various open research challenges exist in this domain, all of which aim to improve the accuracy and utility of this test methodology. Emulation accuracy depends on various factors, namely the detailed mathematical model of the electrical machine, the design and selection of the control for the emulation system, and the selection of emulator hardware technologies. Since PHIL-based machine emulation is a relatively novel testing methodology, there is a need to develop a high-performance, highly accurate test bench. Therefore, this PhD work aims to develop an accurate motor emulation test bench to truly validate the performance of the motor, drive inverter, and drive inverter control prior to manufacturing the prototype motor.

A reliable and flexible grid is crucial for PHIL-based machine emulation system test benches. To achieve this, grid emulators are introduced to enhance the reliability and flexibility of motor emulation systems. Currently, power amplifiers are popular choices for emulators due to their high bandwidth, compact size, and ease of control. However, amplifiers are designed for specific voltage ratings, and when higher voltage is required, a step-up transformer is added to the amplifier output. The connection of the transformer at the output of the amplifier can impact the performance and characteristics of the grid emulator system. Therefore, this research work aims

to characterize the grid emulator system with an amplifier and transformer under various operating conditions.

Machine emulation accuracy depends on various factors, with one of the key factors being the selection of emulator hardware technology. Thus, this research compares three types of machine emulation systems: one utilizing a conventional IGBT-based hard switching power converter, another employing a high-bandwidth soft switching power converter, and the third using a linear amplifier. Detailed configurations and control descriptions for these systems are provided in this work. Comparative experimental studies are conducted, and the obtained results are then compared with those of the physical induction motor (IM) to verify the emulation performance.

The typical voltage source inverter is employed as an emulator converter in motor emulation systems. However, this converter introduces various harmonics into the motor emulation system, primarily attributed to dead time, switching components, and control signals. These harmonics can deteriorate motor emulation accuracy. Therefore, it is important to investigate and compensate for emulator converter harmonics in the motor emulation system. Hence, this PhD work will also explore this topic.

The induction motor drive with an LC filter configuration enables smooth pulse width modulation (PWM) output voltages of the motor drives. Moreover, employing high-performance, high-bandwidth class D power amplifiers as emulator converters enhances the system's bandwidth, thereby ensuring accurate machine emulation. Another open research topic that could improve motor emulation systems is testing electric drives with filters. Testing such a machine drive using conventional emulator structures would be challenging. Therefore, this PhD work will also investigate this topic.

Acknowledgment

First and foremost, I would like to express my deepest gratitude to my supervisors, Professor Chunyan Lai and Professor Pragasen Pillay, for their invaluable guidance, encouragement, and unwavering support throughout the course of my PhD. Their mentorship has been instrumental in shaping both my research and academic growth.

I am sincerely grateful to Dr. Raghav Khanna, Dr. Jassim Hassan, Dr. Shahin Hashtrudi-Zadeh, and Dr. Luiz A. C. Lopes for generously serving on my committee and for their valuable time, insightful feedback, and contributions to this work.

My heartfelt thanks go to my colleagues and friends at Concordia University, especially Dr. Mathew, Dr. Akram, Amir, Yupeng, Dwaipayan, Neetusha, Solihah, Bassam, Ashutosh, Rao, Hani, Abraham, and Jay. Your support, friendship, and the many meaningful conversations we shared made this journey not only productive but also truly enjoyable. Thank you for creating such a collaborative and friendly lab environment.

I also deeply appreciate my colleagues at OPAL-RT Technology. In particular, I would like to thank Amit, Rajendra, Mohammad, and Eric for their collaboration, technical insights, and for providing a stimulating and supportive work environment during a critical phase of my research.

To my beloved parents, your unwavering love and encouragement have been the foundation of this journey. My mother, Sohila, through her boundless care, sacrifices, and wisdom, has been my greatest source of strength and resilience. My father, Hossein, has always inspired me to grow and improve. My sisters, Niloofar and Negar, have brought constant strength and light into my life, not only as family but as trusted companions whose belief in me has meant more than words can express. I am especially indebted to Negar, whose steady presence and dedication from the very beginning helped me navigate the most difficult moments of this journey.

Contents

List of Figures	ix
List of Tables	xv
Chapter 1 Introduction	1
1.1. Grid and machine emulation	1
1.2. Literature review and motivation	3
1.3. Research objective.....	6
1.4. Contributions.....	7
1.5. Organization of this thesis.....	8
Chapter 2 The grid emulator	10
2.1. Overview of the grid emulator system with transformer	10
2.2. Analysis on power amplifier based grid emulator system with transformer interconnection	12
2.2.1. System description	12
2.2.2. Analysis of the impacts on transformer	13
2.2.3. Performance evaluation of the grid emulator.....	15
2.2.4. Grid emulator and transformer soft energizing.....	17
2.2.5. Transformer choice evaluation	17
2.2.6. Transformer Model Verification.....	18
2.3. Simulation and experimental test results on the grid emulation system with a step-up transformer	19
2.3.1. Experimental setup and test results.....	19
2.3.2. Experimental results on the impacts of transformer	21
2.3.3. Experimental results on performance evaluation of the grid emulator.....	28
2.3.4. Experimental results on inrush current mitigation.....	31

2.4. Summary	34
Chapter 3 Comparative study on machine emulation systems based on linear power amplifiers and switching converters.....	36
3.1. Configurations and fundamentals of the emulator systems	36
3.1.1. Motor emulation system description.....	36
3.1.2. Motor emulation system with an IGBT inverter.....	37
3.1.3. Motor emulation system with power amplifier.....	39
3.1.4. Motor emulation system with linear power amplifier.....	40
3.1.5. Comparative analysis between three emulation systems	41
3.2. Experimental setups and results	43
3.2.1. Experimental setups	43
3.2.2. Comparative result	46
3.3. Summary	51
Chapter 4 Harmonic compensation of a power-hardware-in-the-loop based emulator for induction machines	53
4.1. System description of the IM emulator	53
4.2. Harmonic on motor emulator	56
4.2.1. The main harmonic component in the motor emulation system.....	56
4.2.2. Motor emulator controller design	58
4.3. Harmonic compensation for motor emulator	59
4.3.1. PI and PR -based dead time compensation	59
4.3.2. ANN-based harmonics compensation.....	62
4.4. Experimental results	67
4.4.1. Computational time.....	67
4.4.2. Steady state results on no-load and load condition.....	67
4.4.3. Transient results	71

4.4.4.	Harmonic analysis results	75
4.5.	Summary	76
Chapter 5	PHIL based induction motor emulator with LC filter	78
5.1.	System description of IM emulator	78
5.1.1.	Emulator control design	80
5.1.2.	Drive inverter control design	82
5.1.3.	Zero sequence control design.....	84
5.2.	Control in the loop simulation.....	85
5.3.	Experimental setups and results	87
5.3.1.	Experimental setups	87
5.3.2.	Zero sequence controller results	89
5.3.3.	Step change results.....	90
5.3.4.	Harmonic analysis results	94
5.4.	Summary	95
Chapter 6	Conclusion and future works.....	96
6.1.	Conclusion.....	96
6.1.1.	Reviewed grid emulation and induction machine emulation.....	96
6.1.2.	The grid emulator.....	97
6.1.3.	Comparative study on machine emulation systems based on linear power amplifiers and switching converters	97
6.1.4.	Harmonic compensation of a power-hardware-in-the-loop based emulator for induction machines	98
6.1.5.	PHIL based induction motor emulator with LC filter.....	98
6.2.	Future work	98
References.....		100

List of Figures

Fig 1.1 Typical industrial drive testing 2

Fig 1. 2 Machine emulator diagram 3

Fig 2. 1 Schematic diagram of the PHIL grid emulator system with a power amplifier connected to the transformer setting 12

Fig 2. 2 Electrical circuit model of the step-up transformer with DC offset 13

Fig 2. 3 Transformer core and the flux density counter and vector (a) normal condition (b) saturation 18

Fig 2. 4 Experimental setup of grid emulator system with transformer 20

Fig 2. 5 Power amplifier output voltages and currents while it is connected to the transformer. (a) simulation (b) experiment 20

Fig 2. 6 Transformer secondary side phase current (10A/div, top blue line) and voltage (220V/div, bottom red line) when connected to the amplifier (a) simulation (b) experiment 21

Fig 2. 7 Transformer secondary side phase current (10A/div, top blue line) and voltage (220V/div, bottom red line) under sudden load disconnection (a) simulation (b) experiment 21

Fig 2. 8 The measured output current and voltage DC offsets of the amplifier (a) The fundamental frequency changes from 50Hz to 3kHz. (b) The reference phase voltage is changing from 20V to 170V (c) The load changes from 2 A_{RMS} to 10A_{RMS} 22

Fig 2. 9 Transformer temperature measurements (a) The transformer temperature map while the input phase voltage is 170V peak and 120 Hz, under load condition of 10A_{RMS}. (b) temperature measurement setup (1) step up transformer (2) thermocouples 23

Fig 2. 10 The measured transformer temperature while the input phase voltage is 170V peak and 120 Hz, under load condition of 10A_{RMS} (a) winding (b) core 24

Fig 2. 11 The transformer iron loss density at an operating frequency of (a) 60 Hz and (b) 1 kHz 25

Fig 2. 12 The transformer iron loss simulation results with the input voltage set to 170V and a load of 10 A RMS, as the fundamental frequency changes from 60 Hz to 1 kHz 25

Fig 2. 13 The measured transformer primary current while the input voltage is set to 170V with a constant load and fundamental frequency changes from 60Hz to 1kHz 26

Fig 2. 14 The transformer copper loss simulation and experimental results with the input voltage set to 170V and a load of 10 A RMS, as the fundamental frequency changes from 60 Hz to 1 kHz 26

Fig 2. 15 The measured transformer primary current while the input voltage is set to 170V with a constant current and variable resistive load while fundamental frequency changes from 60Hz to 1kHz..... 27

Fig 2. 16 (a) The measured THD when the phase voltage is 170 V peak at load current of 10A_{RMS} and the fundamental frequency changes from 50 Hz to 3 kHz. (a) Measured THD from the output of the amplifier. (b) Measured THD from the output of the transformer 28

Fig 2. 17 The measured bandwidth when the voltage is 170 V peak at load current of 5A_{RMS} and the fundamental frequency changes from 50 Hz to 3 kHz. (a) Measured bandwidth from the output of the amplifier. (b) Measured bandwidth from the output of the transformer (c) The measured bandwidth from the output of the amplifier and the secondary side of the transformer..... 29

Fig 2. 18 (a) Phase current waveform under a voltage step change of amplifier from 30V to 170V at the fundamental frequency of 60Hz. (b). Phase current waveform under a voltage step change of amplifier from 0V to 60V at the fundamental frequency of 60Hz 30

Fig 2. 19 The transformer is energized using the proposed soft magnetizing method with different ramp times. (a) Ramp time: 0.1s. (b) Ramp time: 0.4s..... 31

Fig 2. 20 The transformer is energized using the proposed soft magnetizing method step change from 0 to 60V at the fundamental frequency of 60Hz, Transformer secondary side phase current (I_s , top pink line), Transformer primary side voltage (V_p , middle blue line), and secondary side voltage (bottom green line). (a) resistive load (b) resistive load zoom version..... 32

Fig 2. 21 The transformer is energized using the proposed soft magnetizing method step change from 0 to 60V at the fundamental frequency of 60Hz, Transformer secondary side phase current (I_s , top pink line), Transformer primary side voltage (V_p , middle blue line), and secondary side voltage (bottom green line). (a) nonlinear load (b) nonlinear load zoom version 33

Fig 2. 22 The transformer is energized using the proposed soft magnetizing method step change from 0 to 60V at the fundamental frequency of 60Hz, Transformer secondary side phase current (I_s , top pink line), Transformer primary side voltage (V_p , middle blue line), and secondary side voltage (bottom green line). (a) grid harmonic (b) grid harmonic zoom version 34

Fig 3. 1 Machine emulator block diagram	37
Fig 3. 2 IGBT inverter for machine emulation	38
Fig 3. 3 Open loop magnitude and phase plots for the emulator current control	39
Fig 3. 4 Power amplifier with soft switching for machine emulation	40
Fig 3. 5 Linear power amplifier for machine emulation.....	40
Fig 3. 6 Open loop bode plots design for the current controller of the linear amplifier based emulator system	41
Fig 3. 7 Experimental setup of IM emulator system with (1), (2A), (3), (4), and (5) used for IGBT inverter based emulator system, and (1), (2A), (2B), (4) and (6) used for power amplifier based emulator system	44
Fig 3. 8 Experimental setup of the linear amplifier-based IM emulator system. (1) Linear amplifiers (2) link inductors (3) real time simulator (4) protection circuitry (5) isolation transformer	45
Fig 3. 9 Experimental setup for the physical IM	46
Fig 3. 10 The Experimental results obtained from IM startup condition (a) IGBT based emulator (b) power amplifier based emulator (c) linear amplifier based (d) physical IM (blue emulated machine phase A current, red reference current for emulation generated within the real-time controller, green machine speed)	48
Fig 3. 11 The Experimental results obtained from IM startup condition zoom version (a) IGBT based emulator (b) power amplifier emulator (c) linear amplifier based (d) physical IM (blue emulated machine phase A current, green machine speed Scale:100rpm/div).....	49
Fig 3. 12 Comparative peak fundamental current results between the physical motor, IGBT inverter, power amplifier, and linear amplifier based emulator systems	49
Fig 3. 13 Comparative THD% results between the physical motor, IGBT inverter, power amplifier, and linear amplifier based emulator systems	50
Fig 3. 14 Comparative harmonic current results between the IGBT inverter and power amplifier/linear power amplifier based emulator systems	50
Fig 4. 1 Schematic diagram of the PHIL-based IM emulator system.....	54
Fig 4. 2 Experimental setup of the proposed IM emulator system	55
Fig 4. 3 Experimental setup for the physical IM	55
Fig 4. 4 5th and 7th harmonic comparison between the PI method, and physical machine	55

Fig 4. 5 (a) Per-phase equivalent circuit of the emulation system. (b) The basic configuration of one phase leg of the emulator converter. (c) Switching pattern of the switching devices considering the ideal and actual conditions.....	57
Fig 4. 6 The emulator converter current controller block diagram.....	59
Fig 4. 7 The proposed dead time compensation control scheme. (a) Modified controller for compensating dead time in emulator inverter. (b) Proposed implantation for PR controller	61
Fig 4. 8 Open loop magnitude and phase plots for the proposed PI –PR dead time compensation method compared with the PI controller.....	61
Fig 4. 9 Neural network configuration for the proposed MLPC.....	62
Fig 4. 10 MLPC training loop including the RCD-based controller, the Levenberg-Marquardt optimization algorithm, the mean squared error cost function, and the neural network	65
Fig 4. 11 Regression analysis for training, validation, and testing data	65
Fig 4. 12 Histogram analysis of the training and testing errors	66
Fig 4. 13 (a) Diagram of the proposed ANN-based controller for IM emulation (b) the measured input and output of ANN	67
Fig 4. 14 Experimental results obtained for steady state condition (a) PI based method (b) PI and PR method (c) ANN method (d) prototype IM (Time scale:4 ms/div).....	69
Fig 4. 15 Experimental results measured dq axis emulated current (a) PI-based method (b) PI-PR-based method (c) ANN-based method.....	70
Fig 4. 16 Comparison of the measured phase A current and speed in load condition (a) PI-based (b) PI-PR-based (c) ANN-based (d) Physical machine (Time scale:4 ms/div)	71
Fig 4. 17 Experiment results during startup, (a) PI-based (b) PI-PR-based (c) ANN-based (d) Physical machine (Time scale:500 ms/div)	72
Fig 4. 18 Experimental results obtained for run down (a) PI based method (b) PI and PR method (c) ANN method (d) prototype IM (Time scale:4 s/div).....	73
Fig 4. 19 Experimental results obtained for sudden load increase (a) PI based method (b) PI and PR method (c) ANN method (d) prototype IM (Time scale:4 s/div).....	74
Fig 4. 20 Experimental results obtained for sudden load reduction (a) PI based method (b) PI and PR method (c) ANN method (d) prototype IM (Time scale:4 s/div).....	75

Fig 5. 1 Schematic diagram of the proposed power amplifier-based IM emulator system considering drive with LC filter.....	80
Fig 5. 2 Block diagram of the cascaded power amplifier current control loop within the driving inverter current control loop	81
Fig 5. 3 Magnitude and phase plots for the emulator current control open-loop transfer function	81
Fig 5. 4 LC filter along with three phase IM dq axis equivalent circuit.....	83
Fig 5. 5 Magnitude and phase plots for the driving inverter current control open-loop transfer function	84
Fig 5. 6 CHIL setup (a)-(1) RTS, (a)-(2) DSP, (b) connection of RTS and DSP.....	85
Fig 5. 7 Machine emulator response for a fixed emulator current bandwidth and varying the drive-inverter current-loop bandwidth	86
Fig 5. 8 Machine emulator response for a fixed emulator current bandwidth and varying the LC filter drive-inverter current-loop bandwidth.....	87
Fig 5. 9 Experimental setup of IM emulator system.....	88
Fig 5. 10 Experimental setup for the prototype squirrel-cage induction IM coupled to induction motor dynamometer	88
Fig 5. 11 Experimental results obtained for IM emulator before and after applying zero sequence current controller. (a) phase A emulated current (b) emulator q axis current (c) drive inverter terminal line–line voltage (d) machine speed	89
Fig 5. 12 Experimental results obtained for IM emulator with LC filter drive before and after applying zero sequence current controller. (a) phase A emulated current (b) emulator q axis current (c) drive inverter terminal line–line voltage (d) machine speed.....	90
Fig 5. 13 Experimental results of emulator response for a step change in torque (a) emulated machine q axis reference generated within the real time and q axis emulated current (b) emulated machine speed.....	90
Fig 5. 14 Experimental results of prototype IM response for a step change in torque (a) machine q axis reference generated within the real time and q axis machine current (b) machine speed	91
Fig 5. 15 Experimental results of emulator with LC filter response for a step change in torque (a) emulated machine q axis reference generated within the real time and q axis emulated current (b) emulated machine speed	91

Fig 5. 16 Experimental results of emulator response for a step change in torque (a) phase A emulated machine current (b) q axis emulated current (c) emulated machine speed (d) drive inverter terminal line-line voltage..... 92

Fig 5. 17 Experimental results of prototype IM with response for a step change in torque (a) phase A machine current (b) q axis machine current (c) machine speed (d) drive inverter terminal line-line voltage..... 93

Fig 5. 18 Experimental results of emulator with LC filter response for a step change in torque (a) phase A emulated machine current (b) q axis emulated current (c) emulated machine speed (d) drive inverter terminal line-line voltage 93

Fig 5. 19 Experimental results of prototype IM with LC filter response for a step change in torque (a) phase A machine current (b) q axis machine current (c) machine speed (d) drive inverter terminal line-line voltage 94

List of Tables

Table 2. 1 Specification of transformer selection 18

Table 2. 2 The measured transformer core and winding temperature increases..... 24

Table 2. 3 The simulation results on transformer core and winding temperature increase under grid harmonic injection 26

Table 2. 4 The simulation results on transformer core and winding temperature increase under nonlinear load condition 27

Table 2. 5 The simulation results on transformer core and winding temperature increase under constant current condition..... 28

Table 3. 1 Squirrel cage induction machine parameters 45

Table 3. 2 Qualitative analysis between switched based and linear power amplifier based emulator 51

Table 4. 1 Training parameters 64

Table 4. 2. Execution time for different control methods..... 67

Table 4. 3 Comparative THD% analysis of phase A emulated current and motor..... 76

Table 4. 4 Comparative 5th and 7th harmonic analysis of phase A emulated current and motor 76

Table 5. 1 Comparative THD% analysis of phase A emulated current and motor..... 95

Chapter 1 Introduction

This chapter introduces a grid emulator and power hardware-in-the-loop (PHIL) emulation systems for AC machines. It begins by discussing the basic ideas and importance of grid emulators and PHIL-based machine emulation. Next, it reviews past research in grid emulation and PHIL-based motor emulation, aiming to identify the challenges and progress made in this area. Based on this literature survey, the objectives of this thesis are identified and explained. Finally, the chapter outlines the contributions of this research work and the structure of the thesis

1.1. Grid and machine emulation

In the last century, electrical machines have undergone significant development. They are widely applied in various industrial applications such as electric vehicles, elevators, home appliances, and power plants [1]-[9]. Common types of electric machines utilized in these applications include direct current machines (DCM), induction machines (IM) [3]-[6], permanent magnet synchronous machines (PMSM) [8], and switched reluctance machines (SRM) [1], among others. These machines can operate at various speeds with the aid of a variable frequency drive (VFD). Control methods for these machines typically fall into two main categories: open-loop control and closed-loop control. Depending on the specific application, one of these control methodologies is developed to test electrical machines.

One of the simplest open-loop approaches for testing electrical machines involves directly connecting the electrical machine to the grid. However, for grid-connected machines, the reliability and robustness of the grid during testing are crucial, as grid faults can potentially cause permanent damage to the expensive machine under test. To address this challenge, a grid emulator is introduced. A grid emulator is designed to produce sinusoidal voltage waveforms with flexible magnitudes and various frequencies for grid-connected applications. Conventionally, grid emulators are realized through voltage source inverters (VSIs) and passive filters. However, power amplifiers are now extensively used due to their bandwidth, size, and ease of control. These grid emulators ensure the safe operation of grid-connected electrical machines during testing [10]-[15].

The closed-loop control of electrical machines is essential in any electric machine testing. The conventional drive testing methodology consists of a test motor, an inverter, a load mechanically connected to the motor shaft, and a drive inverter controller [5]. A typical drive

testing diagram is shown in Fig.1-1. As seen in the typical traction drive test setup, AC voltages from the grid pass through the diode bridge rectifier to convert to DC voltage. The rectified DC voltage typically has some ripple, which are smoothed by capacitors located in the DC link. Then, the smoothed DC link voltage is inverted back to alternating voltages with the help of the PWM inverter. A three-phase PWM inverter generally contains six transistors and six anti-parallel diodes. The transistor switches are controlled according to the PWM switching dictated by the required control strategy. All these components are made by different manufacturers with different lead times. Motors usually have a longer lead time compared to the other elements. Therefore, testing of the electrical drive may be delayed due to the manufacturing of the machine [16].

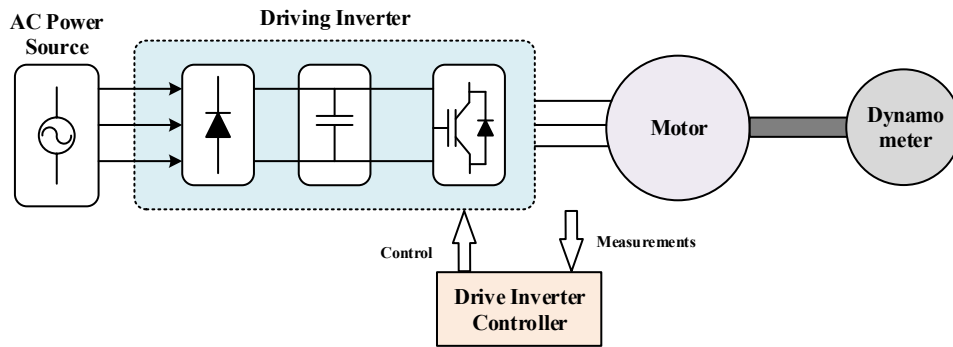


Fig 1.1 Typical industrial drive testing

Power-hardware-in-the-loop (PHIL) based machine emulation is a testing methodology that accelerates the process of testing electrical motors. Machine emulation enables the testing of associated driving inverters and controllers for novel machines in a PHIL environment before the development of the electrical machine. In machine emulation, a set of power converters is controlled to mimic machine behavior. The control of the machine emulator is achieved with the help of a detailed machine model running in a real-time simulator [17],[18]. With a machine emulator system, several machine types and ratings can be emulated without the need for a physical dynamometer test bench for loading the machine. Load torque can be simply applied to the machine model used in the emulator system. This allows for the study of different motor types with various ratings and their corresponding impact on driving inverters and controllers prior to the physical machine being manufactured. Moreover, with the emulator system, testing of driving inverters and controllers can be conducted for severe transient conditions such as faults, reducing the chance of machine damage [16]. A schematic of the machine emulator for electrical drive

testing is shown in Fig. 2. The PHIL-based emulator system mainly consists of an emulator converter, filter elements, and a controller.

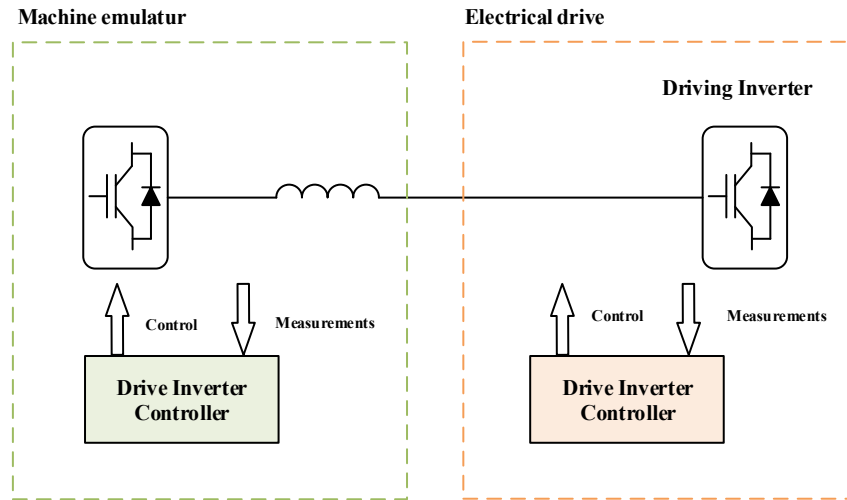


Fig 1. 2 Machine emulator diagram

1.2. Literature review and motivation

The design and development of the machine emulator system are highly important for testing various control methodologies and motor inverters with different power ratings. Therefore, it is essential to develop an accurate emulator system platform. While several research works have been conducted on motor emulator systems, there are still several problems that need to be addressed in this domain to achieve an accurate and reliable motor emulator system. Some of these improvements include:

a. Machine model accuracy

The emulator system relies on an accurate machine model, which is implemented in the real-time simulator system (RTS). In the literature, most research works utilize simple lump motor models for various types of motors, including permanent magnet synchronous machines (PMSMs) [19]-[23], induction motors (IM) [24],[25], variable flux machines (VFM) [26], open-winding PM motors [27], brushless DC (BLDC) motor [28], and switched reluctance machines [29]. However, these simplified motor models neglect details associated with the geometry and magnetic characteristics of the motor, making them unsuitable for accurately mimicking machine behavior, especially during faults and transient conditions.

In [30], a PHIL-based PMSM emulation system is proposed, utilizing lookup table data generated from finite element analysis tools. These machine models incorporate the machine's magnetic characteristics (e.g., saturation) and geometric features (e.g., cogging torque) of the physical machine. In [31], an IM emulator based on a power electronic converter is developed, and magnetic saturation effects are considered in the model, allowing for accurate operation during severe transients, particularly during starting. However, the models proposed in [30] and [31] do not include machine losses and thermal behavior.

b. Drive inverter fault and motor fault emulation

Previous studies have attempted to investigate various faults associated with inverters and motors. Different motor faults have been emulated in the literature, such as stator resistive unbalance faults [32], induction motor rotor cage faults [33], and stator winding faults [34],[35]. Moreover, various drive inverter faults like drive inverter open circuit faults [36], drive inverter single switch faults [37], or multiple switch faults [38] have been studied. Additionally, different grid faults, such as short-circuit grid faults [39], unbalanced grid faults [40], and grid harmonics [41], have been investigated for induction machine emulation. However, some other machine and inverter faults, such as demagnetization, eccentricity, core-related faults, gate driver faults, etc., can also be studied.

c. Precise control structure for the emulator system

Designing and selecting the control structure for the machine emulation system is crucial. The motor drive inverter typically operates in current control mode, and the simplest option for operating the emulator inverter is also in the current control structure. However, this can lead to control conflicts in the emulator system. This issue has been addressed with different approaches in the literature [30], [42], [43]. In [43], the current-in-voltage-out machine model is used to avoid control conflicts. However, using a simplified motor model may reduce the accuracy of the machine emulator. In [42], a different filter element configuration is used, resulting in a more complicated control structure. In [30], a new control structure is proposed where the emulator control is nested within the test inverter current controller loop. This approach addresses control interaction between the test inverter and emulator converter, thereby increasing emulation accuracy.

Moreover, the conventional emulator control structure will need to be modified according to the type of drive being tested. For instance, a motor drive control topology with an LC filter can be tested with the help of an emulator system. However, testing such a drive introduces a new challenge to conventional emulator system approaches because the drive itself incorporates an additional passive filter. Therefore, the conventional emulator structure cannot be used to investigate this type of drive. Consequently, the conventional motor emulator structure will need to be adapted or modified according to the specific drive being tested.

d. Test bench accuracy for the motor emulator

Machine emulators are utilized to test the performance of motor drive inverters and control algorithms. Therefore, the development of an accurate motor emulator test bench is essential to truly validate the required inverter and control performance. The accuracy of the motor emulator system largely depends on the selection of the emulator converter or linear amplifiers. The emulator bandwidth is designed based on the converter switching frequency, with higher switching frequencies resulting in higher emulator bandwidths. Additionally, various power amplifiers with different power ratings and bandwidths exist, which can enhance emulator accuracy. Thus, selecting the emulator device is critical for emulation performance. In the literature, power switch-based inverters [33],[32],[44] and linear amplifiers [40],[41] are commonly used to emulate different machines with varying power ratings. However, the process of selecting the most suitable emulator device has not been extensively studied in the literature. Moreover, the performance and limitations of emulator devices need to be investigated and compared.

Another important factor that can enhance the safety, reliability, and flexibility of emulator test benches is maintaining a reliable grid. In the literature, various grid emulator systems have been proposed [46]-[50]. These grid emulators typically consist of voltage source inverters (VSIs) outputted by passive filters. While these filters reduce switching harmonics, they introduce resonance into the system, leading to a reduction in controller bandwidth. Recently, power amplifiers have been utilized in grid emulator systems to offer high bandwidth with low total harmonic distortion in the output voltage [50]. However, these power amplifiers are designed for specific output voltage levels, making testing at higher voltage levels impossible. Additionally, most power networks, except in North America, operate at 400 V line-to-line voltage, rendering power amplifiers designed for 208V unusable in some regions. While the output voltage of the

amplifier can be increased by adding a step-up transformer at the amplifier output terminals, the impact of this transformer connection on the amplifier and transformer characteristics has not been investigated or characterized in the literature.

While the factors mentioned above can enhance the accuracy of motor emulators to some extent, they are often insufficient. Most emulator systems comprise an emulator converter, typically voltage source inverters (VSIs). However, these converters struggle to accurately mimic machine behavior, primarily due to the inherent nature of VSIs. The voltage and current produced by VSIs contain harmonics, typically arising from dead time, switching components, control signals, etc [51]-[56]. These unwanted harmonics can deteriorate the performance of the emulation system. In the current literature, the effect of harmonic distortion on emulator converters is often overlooked, and compensation for these harmonics is not thoroughly investigated. Therefore, investigating and compensating for emulator converter harmonics has the potential to significantly increase emulator test bench accuracy.

Another crucial component of the emulator system is the filter element located between the emulator converter and the device under test. This filter is responsible for filtering out the switching harmonics from the emulator converter. In many current research papers, a simple inductor is chosen for this purpose [27]-[35]. Selecting a simple inductor allows for a straightforward control structure for the emulator system. However, using a simple inductor may not fully eliminate all the switching and control harmonics generated by the emulator converter. As an alternative, other types of passive filters, such as the LCL filter, have been used to improve the accuracy of motor emulator systems [42]. While the LCL filter can enhance performance and accuracy in the emulator system, it may also reduce the emulator control bandwidth. Therefore, selecting the proper filter element is crucial for optimizing the performance and accuracy of the emulator system.

1.3. Research objective

In the previous section, the motivation behind the research and development of the motor emulation system was explained, and some potential research problems associated with this area were discussed. In this section, the research objectives of this thesis and the problems to be addressed in this research work are as follows:

1. The conjunction of the transformer at the output of the grid emulator can impact both the grid emulator and the transformer characteristics. Hence, it is important to investigate and analyze the effect of the grid emulator transformer interconnection. This research aims to characterize the grid emulator and transformer under various operating conditions.
2. The emulator system test bench in the literature has mostly been developed with conventional switching devices and inverter topology. Such emulator converters provide limited bandwidth, switching ripple, and harmonics in the output voltage. Recently, linear/class D amplifiers have been used for machine emulation to achieve better emulation performance. These amplifiers can provide higher bandwidth for the emulator system with low harmonics and distortion. Thus, this research will also conduct a comparative study between different machine emulator systems to evaluate their performance and limitations.
3. A switched voltage source inverter (VSI) is employed as an emulator converter in the motor emulation system. However, the VSI introduces various harmonics into the motor emulation system. These harmonics are mainly attributed to dead time, switching components, and controlling signals. These harmonics deteriorate motor emulation accuracy. Thus, it is important to investigate and compensate for emulator converter harmonics in motor emulation systems. Therefore, this work aims to investigate and compensate for emulator converter harmonics in the machine emulator system.
4. Low-pass LC filters are introduced to overcome the problem of high dv/dt in the motor terminal due to the VSI. Testing the drive with an LC filter using the conventional emulator system is challenging as the emulator system itself consists of a link filter. So, the emulator system configuration needs to be modified to test such a drive. Therefore, it is important to investigate the effect of this type of motor drive on conventional emulation test benches and modify the emulator system as per requirements.

1.4. Contributions

The contributions of this Ph.D. research work are summarized below.

- Investigation of a grid emulator system connected to a transformer.
- Development of emulator system test benches based on linear amplifiers, class D power amplifiers, and switches.
- Improving the accuracy of motor emulation test benches by reducing emulator converter harmonics.

- Modification of the motor emulator control structure to accommodate testing of an induction motor drive with an LC filter.

Journal Papers:

- **S. N. Afrasiabi**, Mohammad Babaie, C. Lai and P. Pillay "Harmonic Compensation of a Power-Hardware-in-the-Loop Based Emulator for Induction" in IEEE Transactions on Industrial Electronics, doi: 10.1109/TIE.2025.3532726.
- **S. N. Afrasiabi**, R. Thike, C. Lai and P. Pillay, "PHIL based Induction Motor Emulator with LC Filter" under review of IEEE Journal of Emerging and Selected Topics in Power Electronics.
- **S. N. Afrasiabi**, R. Thike, K. S. Amitkumar, C. Lai and P. Pillay, "Investigation of a Transformer Connected Power Amplifier for Versatile Grid Emulation" submitted to IEEE Journal of Emerging and Selected Topics in Industrial Electronics.

Conference papers:

- **S. N. Afrasiabi**, R. Thike, K. S. Amitkumar, C. Lai and P. Pillay, " Investigation of a Transformer Connected Power Amplifier for Grid Emulation," 2023 IEEE 14th International Conference on Power Electronics and Drive Systems (PEDS).
- **S. N. Afrasiabi**, R. Thike, K. S. Amitkumar, C. Lai and P. Pillay, "Comparative Study on Machine Emulation Systems Based on Switching Converters and Linear Power Amplifier Configurations," 2023 IEEE 14th International Conference on Power Electronics and Drive Systems (PEDS).
- **S. N. Afrasiabi**, C. Lai and P. Pillay, "Dead Time Analysis of a Power-Hardware-in-the-Loop Emulator for Induction Machines," IECON 2021 – 47th Annual Conference of the IEEE Industrial Electronics Society.

1.5. Organization of this thesis

The rest of the thesis is divided into the following five chapters.

Chapter 2 provides a brief description of the transformer and grid emulator interconnection, followed by an analysis of their effects. Experimental results are included to validate the impact of this interconnection on the amplifier and transformer grid emulation system.

Chapter 3 introduces and evaluates three different configurations for induction machine (IM) emulation: a conventional IGBT-based inverter, a Class D power amplifier, and a linear amplifier. The chapter begins with discussing the control design for each configuration in detail. It then describes the experimental setup of the emulator systems and presents the results obtained from each configuration. These results are compared with those from a physical machine providing insights into their performance. This comparative analysis aids in selecting the most suitable emulator converter for motor emulation applications.

Chapter 4 explores the nonlinear effects of the emulator converter in the IM emulator system. It begins with presenting the system model, incorporating the emulator converter's nonlinearity, along with a detailed control design for IM emulation. The chapter then introduces a modified control structure aimed at eliminating emulator converter harmonics and dead time. Both classical and intelligent solutions for mitigating these harmonics are discussed. Comprehensive experimental results are provided to validate the proposed control modifications, and these results are compared with those of a physical motor operating under identical conditions. This analysis highlights the effectiveness of the control enhancements in improving the emulator system's performance.

Chapter 5 focuses on the IM emulator system utilizing an LC filter in conjunction with a Class D power amplifier. It provides a detailed explanation of the control design for the emulator control structure to ensure safe and reliable operation of the drive with the LC filter. Control-in-the-loop simulations are first conducted to validate the performance of the IM emulator with the LC filter. A high-performance and high-bandwidth Class D power amplifier is employed to emulate the drive, supported by a single DC power supply to power both the drive inverter and the emulator converter for minimizing the required equipment. Comprehensive experimental results are presented, along with a comparative analysis against a physical IM setup under identical driving inverter operating conditions, to validate the emulation accuracy.

Chapter 6 concludes the thesis and discusses possible future work to extend or improve the research proposed in this thesis.

Chapter 2 The grid emulator

Power grid emulators are used extensively for the testing and validation of grid-tied applications. Currently, power amplifiers are extensively used as grid emulators because of their higher bandwidth, compact size, and ease of control. Usually, amplifiers are designed for specific output voltage ratings. For an application requiring a higher voltage level, the output voltage of the grid emulator system can be increased by adding a step-up transformer at the amplifier output terminals. However, the conjunction of the transformer at the output of the amplifier will affect the amplifier and the transformer characteristics. Thus, it is important to investigate and analyze the effect of the amplifier transformer interconnection. This thesis studies the transformer connected four quadrant power amplifier for grid emulation. The proposed work characterizes the amplifier and transformer in different operating conditions considering the influence of DC offset, THD level, transformer thermal behavior, amplifier control bandwidth, and the system startup performance. The proposed analyses have been tested and validated experimentally through a 5-kW grid emulator, while it is connected to a step-up transformer.

2.1. Overview of the grid emulator system with transformer

Grid-connected devices are extensively used in many industrial domains, such as transportation and power distribution systems [57]-[60]. The safety, reliability, and robustness of grid-connected equipment are highly important during manufacturing. Thus, maintaining a reliable grid is becoming more important during the testing of grid-connected equipment, especially in areas where a reliable grid cannot be maintained. Moreover, different types of grid faults may occur during the testing and development of the device, which may cause permanent damage to the equipment under test [60]. Thus, the power grid emulator is introduced so as to provide an AC voltage supply similar to the actual grid. Moreover, the grid emulator is able to produce the sinusoidal voltage waveform with flexible magnitude and various frequencies, similar to the case of a machine emulator. In addition, some non-ideal grid conditions, such as grid unbalance and grid voltage distortion, can be provided by the grid emulator to test the devices comprehensively.

In the literature, different grid emulator systems have been proposed [46]-[50]. These grid emulators are mainly voltage source inverters (VSIs) with L, LC, and LCL filters. These output filters are used to eliminate the switching harmonics of the VSIs. The voltage across the capacitor

of the LC and LCL filter is controlled to track the emulated grid voltage references [61]. The passive filters reduce the switching frequency components, but they introduce resonance into the system, which leads to controller bandwidth reduction [61], [62]. Recently, power amplifiers have been used in grid emulator systems that offer higher bandwidth, with low total harmonic distortion, high output voltage, and the capability of four-quadrant operation. However, these power amplifiers are typically designed for specific output voltage ratings, which limits their application to higher voltage levels. In most power networks outside of North America, the utility voltage ranges around 400 V line-to-line, So the power amplifiers that are designed for 208V are unsuitable for these regions. Thus, this research work proposes connecting a step-up transformer at the output of a versatile 208V power amplifier to enhance the output voltage capability of the grid emulator system.

The conjunction of the transformer at the output of the power amplifier will affect the amplifier and the transformer behaviors. One of the impacts of this interconnection is the imperfect operation of the power amplifier, which will inject a DC voltage into the transformer's primary winding. This DC bias will cause the unidirectional saturation of the magnetic core of the transformer that potentially leads to the core overheating, asymmetrical hysteresis loop, increased eddy current losses, thermal stresses, and a reduction of the lifetime of transformer and amplifier. Thus, this research work will model, investigate, and analyze the effect of the amplifier transformer interconnection in a PHIL-based emulation system. This investigation reveals insights into the safe operation of the power amplifier, transformer, and other device under test (DUT).

Moreover, the accuracy of a grid emulator system depends on the power amplifier bandwidth. Various switching and linear amplifiers are used in the literature [63], [64]. However, these amplifiers either have a bandwidth limitation or higher power loss. This work uses OPAL-RT's high frequency four-quadrant power amplifier with soft switching technology so as to accurately mimic the grid. The proposed investigations on the influences of DC offset, system THD level, transformer thermal behaviors, amplifier control bandwidth, and the system start up performance. During system startup, the transformer generates a high inrush current with significant amplitude. This characteristic may cause damage to both the grid emulator and the DUT.

The accuracy of a grid emulator system depends on the power amplifier selected. Various switching and linear amplifiers are used in the literature [63], [64]. However, these amplifiers

either have a bandwidth limitation or higher power loss. This Chapter uses a [65] high frequency four quadrant power amplifier with soft switching technology to accurately mimic the grid. To evaluate its performance after connecting with a transformer, investigations are also conducted on the resulting system THD level, amplifier control bandwidth, and the system startup performance in addition to the aforementioned analysis on the transformer.

2.2. Analysis on power amplifier based grid emulator system with transformer interconnection

This section first explains the configuration of the grid emulator system with a transformer. Then it will follow with the analysis on the impact of this interconnection on the transformer and power amplifier, respectively.

2.2.1. System description

Fig 2.1 illustrates a schematic diagram of the proposed grid emulator system with a power amplifier connected to the transformer. This diagram mainly consists of a power amplifier-based grid emulator, a step-up transformer, the device under test, and a real time simulator (RTS).

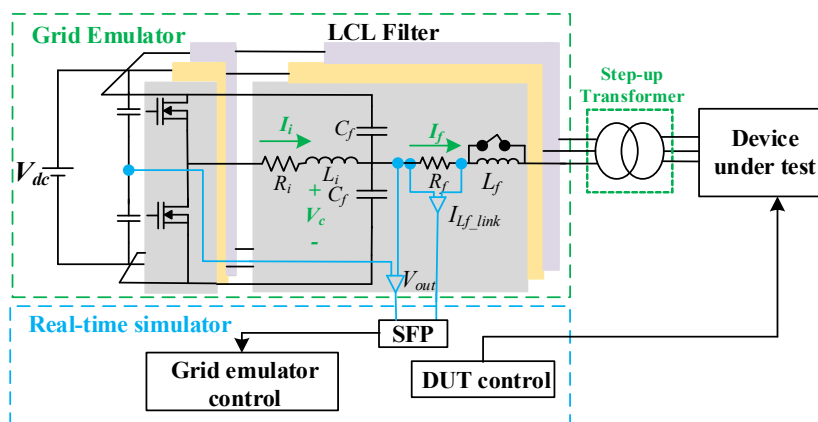


Fig 2. 1 Schematic diagram of the PHIL grid emulator system with a power amplifier connected to the transformer setting

In this study, a three-phase four-quadrant power amplifier is utilized [65]. The amplifier has a bandwidth of 10 kHz. The control for the grid emulator is implemented in an RTS. The control signal is sent from the power amplifier to RTS via a high-speed fiber optic (SFP) link. The amplifier is designed to output a line-line voltage of 208 V_{rms}. Employing the step-up transformer at the output of the power amplifier increases the voltage for operation to 400 V line-line rms. Two

different types of DUTs, namely resistive and nonlinear loads, were used to validate the proposed configuration.

The use of the transformer at the output of the power amplifier enhances the utility of the grid emulator system. However, this interconnection may affect the performance of the transformer and amplifier. For instance, the amplifier has a DC offset at the output voltage due to the sensors, and the transformer performance during startup may influence the grid emulator performance. Therefore, in the following section, these effects are modeled and explained.

2.2.2. Analysis of the impacts on transformer

This subsection investigates and analyzes the effect of this interconnection on the transformer side. A circuit diagram of the amplifier connected to a step-up transformer is shown in Fig 2.2. Voltage and current sensors which are located in the power amplifiers create a DC offset at the output voltage of the amplifier. Thus, one of the impacts on the transformer through this interconnection is the DC offset introduced by the sensors of the power amplifier. In this case, the three-phase transformer equivalent circuit should be modified so as to have a DC bias source in each leg. The electrical circuit model of the transformer is shown in Fig 2.2.

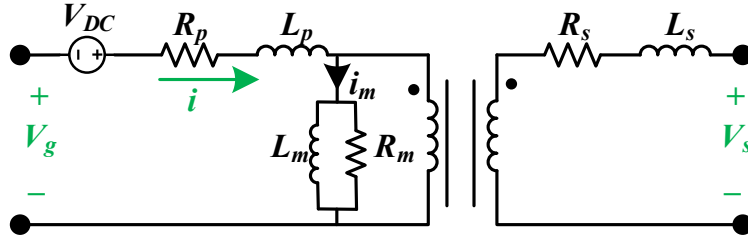


Fig 2. 2 Electrical circuit model of the step-up transformer with DC offset

In Fig 2.2, R_p , and L_p , are the primary side resistances and leakage inductances of the transformer. The R_m is the core loss resistance, and L_m is the magnetizing inductance. R_s , and L_s are secondary side resistances and leakage inductances of the transformer. The voltage equation for the primary winding of the transformer can be written as follows,

$$V_g - V_{DC} = R_p i(t) + L_p \frac{di}{dt} + e \quad (2-1)$$

where V_g is the amplifier output voltages, i is the primary side current with $i = i_{DC} + i_{AC}$. Also, the polarity of the DC bias may change according to the DC offset in the sensor. The voltage

induced by the primary flux is $e = -N \frac{d\varphi}{dt}$, where the flux φ consists of the DC offset component and AC component ($\varphi = \varphi_{DC} + \varphi_{AC}$). The flux component can be calculated as

$$\varphi = -\frac{1}{N} \int e dt \quad (2-2)$$

Considering the DC offset component is negligible (which will be proven through the experimental results section), and $e = E \sin \omega t$, (2-2) can be updated as

$$\varphi_{AC} = \frac{E}{N\omega} \cos \omega t \quad (2-3)$$

Based on (2-1), when the amplifier output voltage magnitude is set to be constant, and the load current magnitude is constant, the magnitude of e will be constant. In this case, the magnitude of the magnetizing flux in the transformer reduces as the operation frequency increases according to (2-3).

One of the capabilities of the grid emulator system is that can operate in different operation frequencies. When the transformer is connected as part of the grid emulator, its operation frequency should also be changing. Therefore, during the operation under a constant voltage magnitude set point and constant load current, the magnitude of the transformer magnetizing flux will reduce as the operation frequency increases according to (2-3). This will lead to a reduction in the flux density B , and hence the core losses in the transformer. This is because the transformer core losses mainly consist of the eddy current loss (P_e) and hysteresis loss (P_h), and these two losses follow the relationship in (2-4),

$$P_e, P_h \propto B^n f \quad (2-4)$$

where $n=2$ for the eddy current loss and $n=1.6$ for hysteresis loss. If the load current is constant the flux density (B^n) is constant, so, the transformer core losses and hysteresis losses will increase as the operation frequency increases. However, in the proposed grid emulator system. There is no control over the load current. Therefore, as the frequency increases the flux density decreases due to the increase of the transformer winding reactance which leads to a reduction in the core losses at a higher frequency

If the DC offset component caused by the amplifier is high, the amplifier produces a bipolar flux (AC component) as well as a relatively large unipolar flux (DC component) in the transformer core. This DC component will create an unwanted current harmonic into the transformer magnetizing current, which could lead to overheating of the transformer [66], [67]. Moreover, the

power amplifier injects some switching and other controlled harmonics into the transformer. These harmonics would again lead to the heating of the transformer, so one of the expected impacts would be additional losses in the transformer due to the grid emulator characteristic. Therefore, it is essential to characterize the DC offset produced by the grid emulator at first, and then the transformer thermal behavior should be determined.

Lastly, grid emulators usually are designed to operate in different frequency ranges, while the selected amplifier for this study can operate up to 10 kHz. However, most of the transformers are designed for 50/60Hz operation. Therefore, running a transformer at high frequency could adversely affect its operation, so it is also essential to analyze the transformer behavior under different operating frequencies.

2.2.3. Performance evaluation of the grid emulator

The power amplifier has performance specifications such as THD, bandwidth, etc. When this amplifier is connected to the transformer, it may potentially affect the amplifier performance specifications. For example, the transformer brings additional inductances to the system, and due to these inductances, the amplifier switching and control harmonics are reduced which leads to a lower THD level at the output of the transformer. Moreover, the transfer function associated with the transformer can be approximated as a second order transfer function [67], resulting in a change of amplifier bandwidth, and more importantly, it may degrade the grid emulator performance. Thus, to have a safe operation for the transformer and the amplifier, the amplifier performance in terms of THD and control bandwidth will be tested.

Moreover, a step-up transformer is added between the grid emulator and the DUT, introducing impedance into the system that can affect the overall performance and the impedance seen by the grid emulator. The transformer contributes to the series and the parallel impedance components, depending on its characteristics, such as winding resistance, leakage reactance, and other parameters. Additionally, the grid emulator typically has its own internal impedance, which includes the controller dynamics and any additional load or filter elements. The total impedance seen by the DUT is therefore the sum of the emulator's internal impedance and the reflected impedance from the transformer. To simulate or account for this impedance, the grid emulator's control system can be adjusted to reflect the total impedance. This adjustment may involve modifying the voltage or current control loops to account for the additional load introduced by the transformer and to ensure that the emulator is maintaining the voltage stability and power quality.

However, in this study, since the grid emulator is a commercial system, we did not have access to modify its control system, and this delay could not be incorporated into our control design.

One of the additional impacts of this interconnection is the inrush current phenomenon. The inrush current occurs during the startup of a transformer [68]-[71]. During the startup, there is no current flowing in the secondary side of the transformer. So, for a very short time, it becomes an open circuit while the primary side of the transformer is energized. By considering the grid emulator voltage as $V_g = \sin(\omega t + \alpha)$ and looking back at the single-phase equivalent, by solving (2-1), the magnetic flux φ_{AC} can be expressed as follows:

$$\varphi_{AC} = \frac{-L_m V_P \cos(\omega t + \alpha)}{\sqrt{R_p^2 + (\omega L_T)^2}} + \left(\phi_r + \frac{L_m V_P \cos(\alpha)}{\sqrt{R_p^2 + (\omega L_T)^2}} \right) e^{-\frac{R_p}{L_p} t} \quad (2-5)$$

where L_p is the inductance of the primary winding, ϕ_r is the residual core flux, V_P is the grid emulator voltage amplitude, ω is the angular frequency and α is the energization angle on the voltage waveform. Alternatively, the equation (2-1) can be solved with respect to the primary side current (i). The differential equation solution can be derived

$$i(t) = (i(t_0) + i_{dc}) e^{-\frac{R_p}{L_p}(t-t_0)} + i_{ac} \quad (2-6)$$

$$i_{dc} = \frac{-V_p \sin(\omega t + \alpha - \beta)}{\sqrt{R_p^2 + (\omega L_T)^2}}$$

$$i_{ac} = \frac{V_p \sin(\omega t + \alpha - \beta)}{\sqrt{R_p^2 + (\omega L_T)^2}}$$

where $\beta = \tan^{-1}(\omega L_p / R_p)$ is introduced to simplify the expression. The magnetic flux and primary current in (2-5) and (2-6) are comprised of two components: a steady periodic component and a transient component that decreases exponentially with a time constant of R_p / L_T . In normal operation conditions when the transient component is zero and the core flux oscillates symmetrically resulting in minimal magnetizing current. When the transient term is non-zero with a high value, then the flux has a DC component that temporarily shifts its center-point in the positive or negative directions, possibly shifting its peak deep into the saturation region and resulting into high magnitudes inrush currents. The inrush current does not damage the transformer. However, this may cause damage to the grid emulator system.

2.2.4. Grid emulator and transformer soft energizing

As mentioned earlier, transformer inrush current may damage the grid emulator system. Therefore, the soft energizing technique is proposed in this work to ensure the safety and utility of the grid emulator with the transformer. According to (2-5) and (2-6), it can be seen that there are five factors influencing the decrease of the flux/current peak value, namely R_p , L_T , V_p , $\cos(\alpha)$, and ϕ_r . However, it is easier to control V_p than other factors. The work presented in this work applies a technique in which the transformer is energized through a controlled voltage. To achieve this, the voltage is slowly ramped up between 0 and the maximum value over a period equal to T_{ramp} . The applied input voltage across ramping and steady-state stages is defined in (2-7):

$$V = \begin{cases} \frac{t}{T_{ramp}} V_p \sin(\omega t + \alpha) & : t \leq T_{ramp} \\ V_p \sin(\omega t + \alpha) & : t > T_{ramp} \end{cases} \quad (2-7)$$

The voltage ramps should be designed to mitigate inrush currents. The transient decay should be faster than the ramp to ensure the resultant peak flux remains below saturation limits. A very fast ramp can cause excessive inrush currents beyond the transformer's rating, while a very slow ramp is unnecessary. Therefore, selecting an appropriate ramp time (T_{ramp}) is a crucial task.

2.2.5. Transformer choice evaluation

The transformer to be selected for the output should meet specific criteria. Since it will be connected to the versatile grid emulator, it must operate within the frequency range of up to 10 kHz. The core material should be silicon steel, as it is suitable for this frequency range. Materials like ferrite, which only operate at high frequencies, are not appropriate for this application.

The transformer current rating (I_{tr}) should be higher than the grid emulator current (I_{grid}). This will ensure that the transformer operates in an unsaturated condition. For this study, the transformer is modeled in JMAG, with the grid emulator voltage set to 170 V peak at 60 Hz. The unsaturated transformer core and the flux density counter and vector plot are shown in Fig 2.3 (a). The same transformer is simulated using a 10% higher current, resulting in saturation, as shown in Fig 2.3 (b).

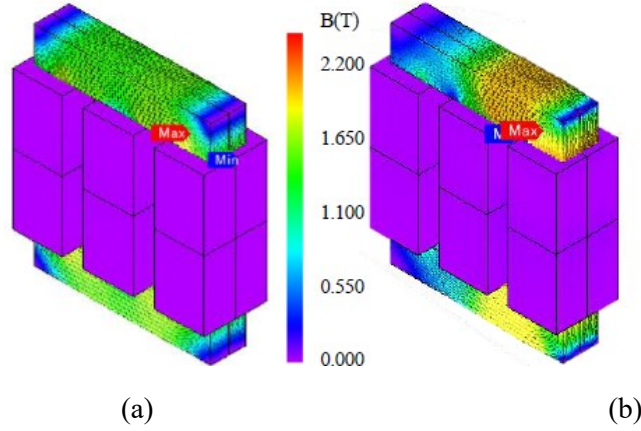


Fig 2. 3 Transformer core and the flux density counter and vector (a) normal condition (b) saturation

To ensure the transformer core remains unsaturated, the selected transformer power (S_{tr}) should be higher than the grid emulator power (S_{grid}). Additionally, the transformer temperature (T_{tr}) should be below the insulation class temperature (T_{ins}). This guarantees the safe operation of both the grid emulator and the transformer.

One of the goals of the grid emulator is to generate different harmonic magnitudes for the DUT at the secondary side. This should be ensured at the transformer's secondary side. Therefore, the transformer connections should not be delta on either the secondary or primary side, as delta connections eliminate triple harmonics.

Table 2. 1 Specification of transformer selection

Parameter	Specification
Core material	Silicon steel
Current	$I_{grid} < I_{tr}$
Power	$S_{grid} < S_{tr}$
Temperature	$T_{tr} < T_{ins}$
Connection	Star

2.2.6. Transformer Model Verification

The transformer model developed using JMAG software was verified through a systematic process to ensure its accuracy and reliability. Initially, the transformer's geometry and electrical parameters such as core dimensions, material properties, and winding characteristics were

precisely measured. These parameters formed the basis for constructing the simulation model in JMAG, where the physical design and operating conditions were accurately replicated.

To validate the model, key static and dynamic performance metrics, including winding resistance, leakage inductance, core losses, and transient response, were compared against experimental data obtained from laboratory tests (will be presented in the next chapter). The transformer core and winding temperatures were also evaluated to confirm the model's accuracy under varying conditions. Iterative refinements were made to address any discrepancies between the simulated and measured results. The final validated model closely matched the experimental data, ensuring its reliability for further analysis and applications.

2.3. Simulation and experimental test results on the grid emulation system with a step-up transformer

This section investigates the effect of the transformer interconnection with the amplifier for grid emulation through simulation and experimental tests. The experimental setup and some preliminary test results will be provided first, to validate the functionality of the grid emulator system when connected to the transformer. Then, the effect of this interconnection on the transformer as well as the power amplifier will be investigated through simulation and experimental tests.

2.3.1. Experimental setup and test results

Fig 2. 4 shows the experimental setup of the grid emulator system with a power amplifier and a transformer. The power amplifier used in this study is described in [65]. This power amplifier has the capability to source and sink 5 kW at 14 A rms. The amplifier can operate in both voltage control mode and current control mode, with a bandwidth of 10 kHz. The three-phase transformer has a rating of 7.5 kVA, 120V/240V, and 60 Hz. The control of the power amplifier is implemented in a real-time simulator system. A three-phase resistive load is connected to the output of the transformer through a contactor. The inverter is used as a nonlinear load connected to the secondary side of the transformer. A bridge diode rectifier is used for this purpose. A DC power supply of 500 V is used for powering the amplifier, and a data acquisition system is used for data recording.

In this subsection, the operation of the proposed power amplifier based grid emulator system with transformer interconnection is tested and validated. Fig 2.5 (a) and (b) show the

simulation and experiment results, respectively, of the amplifier output voltage and current waveforms when the amplifier is operating in the voltage control mode with the reference phase voltage set to 60 Hz and 170 V peak, and the resistive load is connected to the transformer's secondary side. It is clear from the waveforms that there are DC offsets in the three-phase currents and voltages.

Fig 2. 6 (a) and (b) show the simulation and experimental results of the voltage and current waveforms at the transformer's secondary side under the same conditions. These steady-state results demonstrate the viability of the amplifier-transformer interconnection.

Fig 2. 7 shows the measured current and voltage waveforms when the contactor is opened to disconnect the load. The results are for a rated amplifier voltage and current condition while the load is connected to the transformer. It can be seen that the grid emulator is also functional in this transient condition. Further investigations will be conducted in the following two subsections.



- (1) real time simulator
- (2) power amplifier
- (3) DC power
- (4) inverter
- (5) resistive load
- (6) contactor
- (7) data acquisition
- (8) transformer

Fig 2. 4 Experimental setup of grid emulator system with transformer

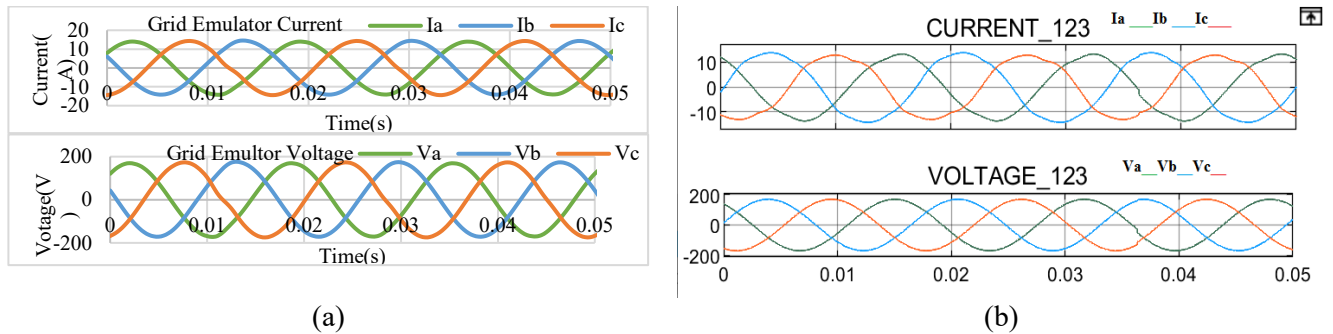
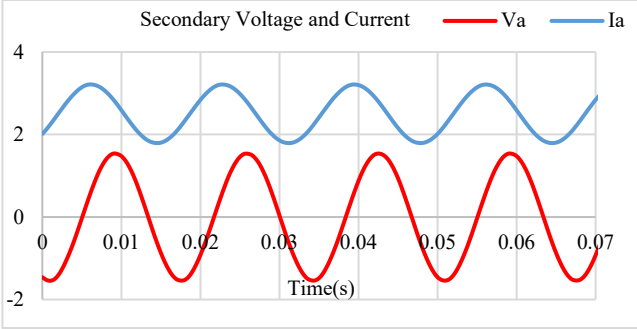
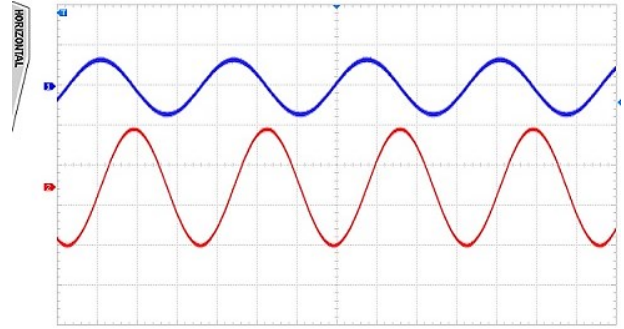


Fig 2. 5 Power amplifier output voltages and currents while it is connected to the transformer. (a) simulation (b) experiment

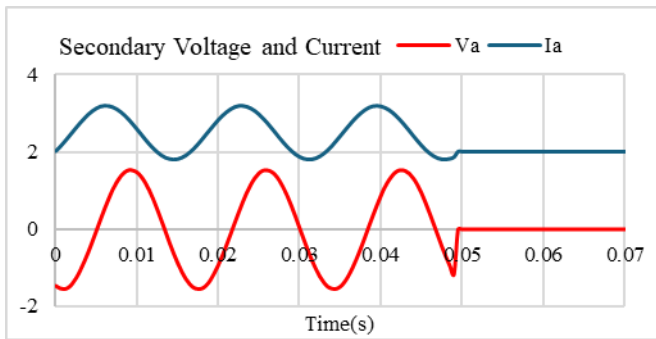


(a)

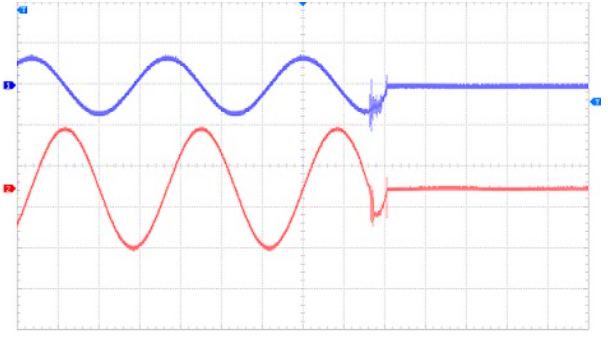


(b)

Fig 2. 6 Transformer secondary side phase current (10A/div, top blue line) and voltage (220V/div, bottom red line) when connected to the amplifier (a) simulation (b) experiment



(a)



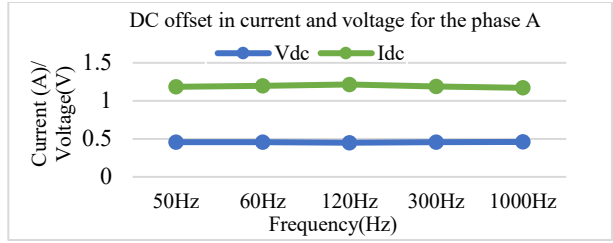
(b)

Fig 2. 7 Transformer secondary side phase current (10A/div, top blue line) and voltage (220V/div, bottom red line) under sudden load disconnection (a) simulation (b) experiment

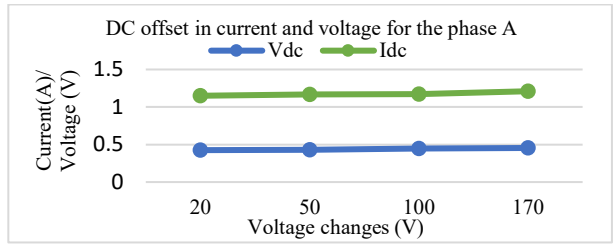
2.3.2. Experimental results on the impacts of transformer

As analyzed in section 2.2 and validated in the previous subsection, the voltage and current sensors in the power amplifiers can cause a DC offset at its output voltage and hence the current. The DC offset components under different operation frequencies, voltage levels, and loading conditions are characterized first, and then their impacts will be studied.

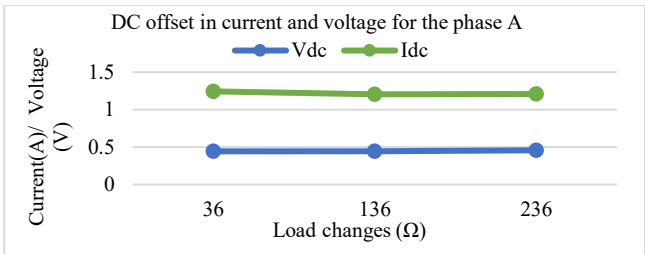
Fig 2.8 (a) presents the measured DC offset on the voltage and current outputs of the amplifier under different operation frequencies, while the phase voltage reference is set to 170 V peak. It can be seen that the DC offset is almost constant when the operation frequency changes from 50 Hz to 3 kHz.



(a)



(b)



(c)

Fig 2. 8 The measured output current and voltage DC offsets of the amplifier (a) The fundamental frequency changes from 50Hz to 3kHz. (b) The reference phase voltage is changing from 20V to 170V (c) The load changes from 2 A_{RMS} to 10A_{RMS}

Fig 2.8 (b) presents the measured DC offset on the voltage and current outputs of the amplifier under different voltage levels. In this case, the amplifier phase voltage reference is changing from 20V to 170V peak while the load current is 10A_{RMS} and the frequency of operation is 60Hz. It is seen that the DC offset is almost constant at different voltage levels.

The measured DC offset on the voltage and current outputs of the amplifier under various loading conditions are shown in Fig 2.8 (c), while the phase voltage reference is set to 60Hz and 170V peak. In this test, the load current changes from 2A_{RMS} to 10A_{RMS}. It can be observed that the DC offset is also constant under different load current conditions.

As can be seen from the test results in Fig 2.8, the DC offset voltages produced by the amplifier are small and negligible. The rest of this subsection will test and analyze the transformer temperatures under different operation frequencies while it is connected to the amplifier.

Fig 2.9 (a) presents the JMAG simulation results, where the input phase voltage is 170V peak and 120 Hz. Under a load condition of 10A RMS, it can be seen that the transformer temperature reaches 70°C. Fig 2.9 (b) shows the experimental setup of the transformer for temperature measurement.

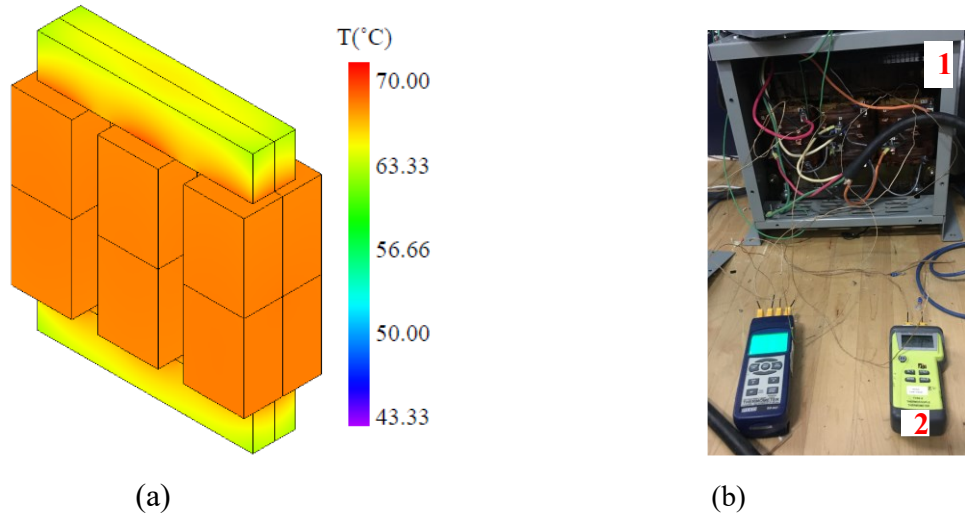


Fig 2. 9 Transformer temperature measurements (a) The transformer temperature map while the input phase voltage is 170V peak and 120 Hz, under load condition of 10A_{RMS}. (b) temperature measurement setup (1) step up transformer (2) thermocouples

In the temperature tests, the maximum voltage of the amplifier is applied, and a constant resistive load is connected at the transformer output to produce a load current of 10Arms, while the operation frequency changes from 60Hz to 1 kHz. For the temperature tests, the operation frequency is limited to 1 kHz because, at higher operation frequencies, some esoteric noise has been observed in the resistive load. Thus, this test is only conducted up to 1 kHz. In addition, the resistance in the load could increase as the operation frequency increases, which will lead to a slight decrease in the load current. Thermocouples are used to measure the temperatures at two different points in the core and the winding of the transformer, respectively, and the average value has been taken as the measured temperature. Figures 10 (a) and (b) present the temperature curves of the transformer winding and core, respectively, taken from simulation and experiment under 120 Hz over 5 hours. The transformer winding and core temperatures from both the simulation and experiment stabilize at 67.5°C and 61.98°C under these test conditions.

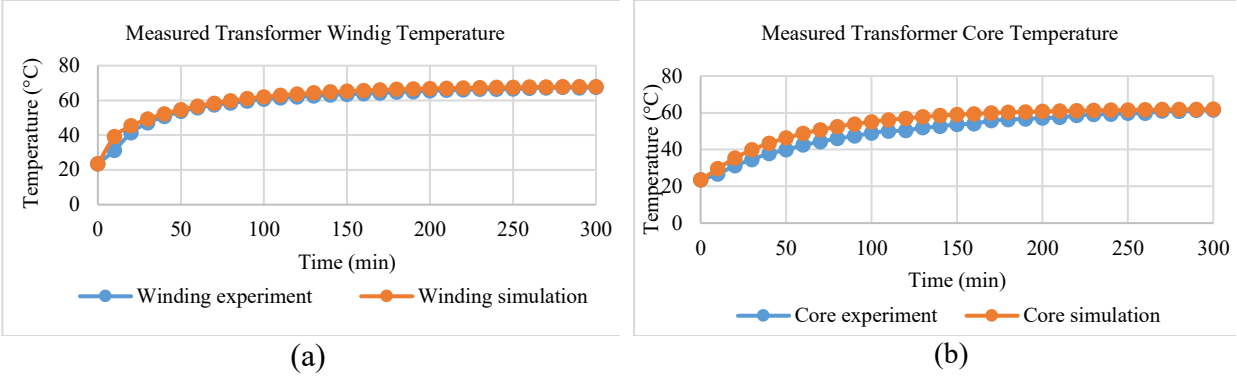


Fig 2. 10 The measured transformer temperature while the input phase voltage is 170V peak and 120 Hz, under load condition of 10A_{RMS} (a) winding (b) core

To evaluate the transformer temperature increase under different operation frequencies, the ambient temperature is deducted from the measured core and winding temperatures. Table 2.2 summarizes the temperature increases in the transformer’s winding and core after the temperatures stabilize under different operating frequencies. It is evident from Table 2.2. , the temperature increases in the winding and core of the transformer reduce slightly as the amplifier’s operation frequency increases. The temperature increase in the transformer core at higher operation frequency is lower as shown in Table 2.2.

Table 2. 2 The measured transformer core and winding temperature increases

Core temperature increase (°C)				
Frequency (Hz)	60	120	300	1000
Simulation	43.27	41.5	39.99	36.97
Experiment	45.4	43.8	39.5	37.9
Winding temperature increase (°C)				
Frequency (Hz)	60	120	300	1000
Simulation	47.03	44.26	42.27	38.27
Experiment	44	42.4	40.1	31.3

The transformer iron loss is measured using the JMAG simulation model, while the operating frequency is varied from 50 Hz to 1 kHz. Fig 2.11 presents the iron loss density at 60Hz and 1 kHz. Fig 2.12. Presents the iron loss results at different operating frequencies. These results also confirm that as the operating frequency increases, the transformer iron loss decreases.

The winding temperature increase is mainly a result of the copper loss in the equivalent winding resistance. As the operation frequency increases, the equivalent resistance increases, if the load current is constant, then the copper loss should be higher. However, the amplifier is under voltage control mode, which means a constant voltage is applied to the resistive load during the test, so the load current will reduce as the resistances increase when the operation frequency increases.

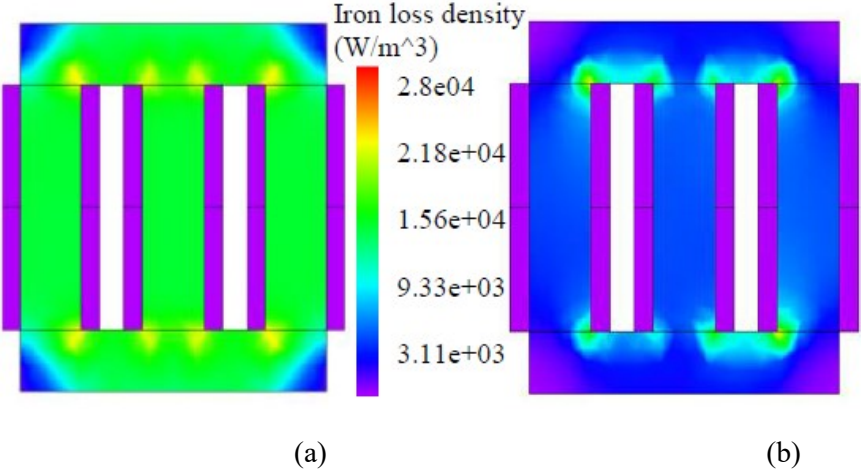


Fig 2. 11 The transformer iron loss density at an operating frequency of (a) 60 Hz and (b) 1 kHz

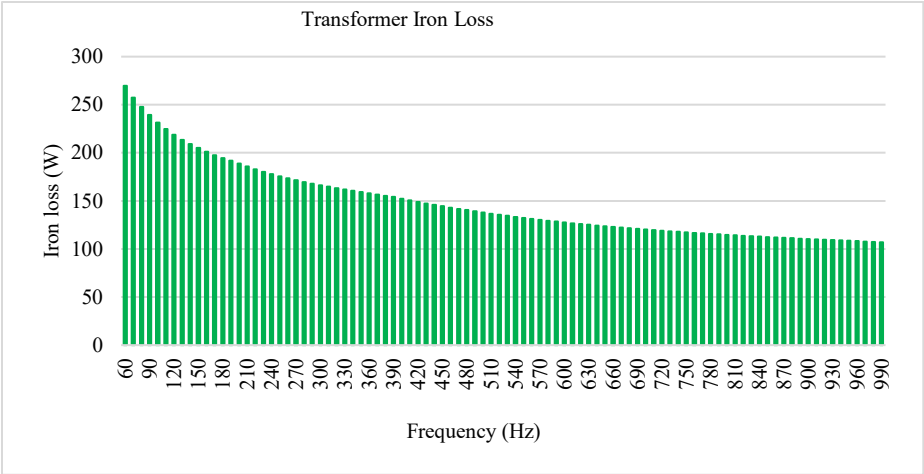


Fig 2. 12 The transformer iron loss simulation results with the input voltage set to 170V and a load of 10 A RMS, as the fundamental frequency changes from 60 Hz to 1 kHz

Fig 2.13 presents the results obtained from the simulation and experiment, showing the reduction in load current at higher frequencies. As a result, the copper loss in the transformer winding reduces as the operation frequency increases, which leads to a reduction in the winding

temperature increase. Fig 2.14 presents the transformer copper loss results obtained from both simulation and experimental data as the operating frequency changes from 50 Hz to 1 kHz. These results show lower copper loss at higher frequencies.

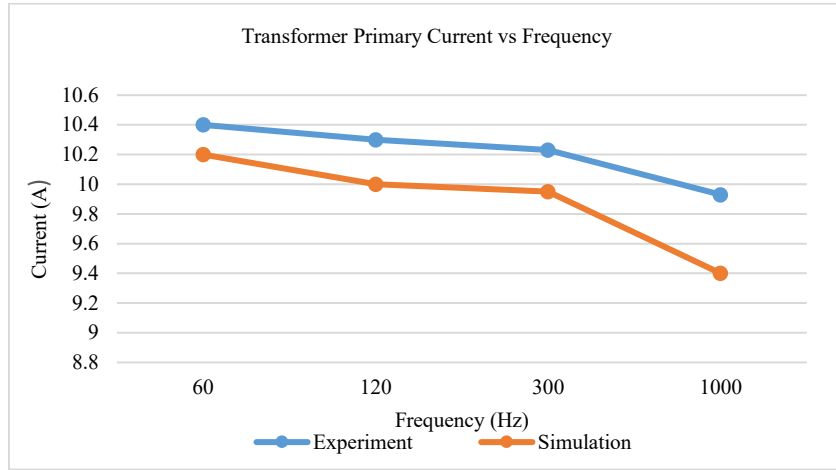


Fig 2. 13 The measured transformer primary current while the input voltage is set to 170V with a constant load and fundamental frequency changes from 60Hz to 1kHz

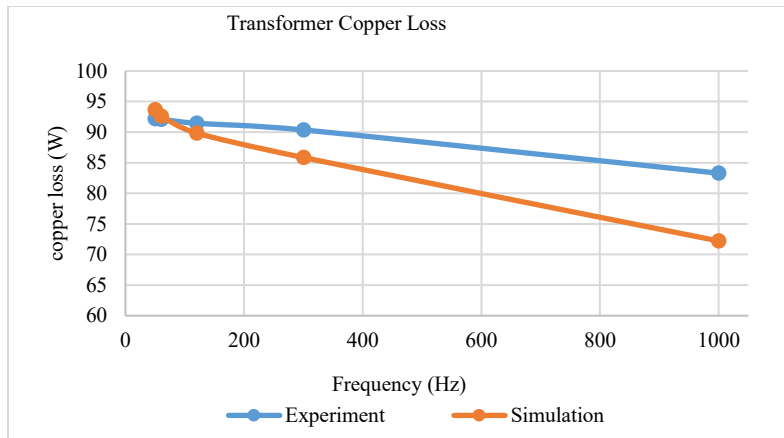


Fig 2. 14 The transformer copper loss simulation and experimental results with the input voltage set to 170V and a load of 10 A RMS, as the fundamental frequency changes from 60 Hz to 1 kHz

Table 2. 3 The simulation results on transformer core and winding temperature increase under grid harmonic injection

	Temperature increase (°C)			
Frequency (Hz)	60	120	300	1000
Simulation core	45.17	42.40	41.93	37.88
Simulation winding	49.41	44.82	44.82	37.96

The transformer winding and core temperatures were obtained during the injection of the 5th harmonic from the grid emulator into the transformer, as the operating frequency varied from 60 Hz to 1 kHz. Table 2.3 presents the simulation results under grid harmonic conditions, showing a slight increase in both core and winding temperatures compared to the resistive load condition.

The transformer temperature is evaluated under nonlinear load conditions. Table 2.4 lists the simulation results obtained from the grid emulator system while the DUT was subjected to a nonlinear load across a frequency range of 60 Hz to 1 kHz. As shown, the temperatures of the transformer core and winding increase compared to the resistive load condition. This increase is primarily due to the harmonics injected from the nonlinear load into the transformer.

Table 2. 4 The simulation results on transformer core and winding temperature increase under nonlinear load condition

Temperature increase (°C)				
Frequency (Hz)	60	120	300	1000
Simulation core	54.5	53.1	50.04	45.76
Simulation winding	56.7	50.15	49.6	43.59

Figure 2.15 presents the simulation results with a constant load current across a frequency range from 60 Hz to 1 kHz. The resistive load value is adjusted to maintain a constant current throughout the frequency range. It can be seen that as the frequency increases, the resistive load value decreases. In this condition, the temperatures of the transformer core and winding were measured and are listed in Table 2.5. The temperature increase in the transformer core and winding is higher at higher operating frequencies, as shown in Table 2.5.

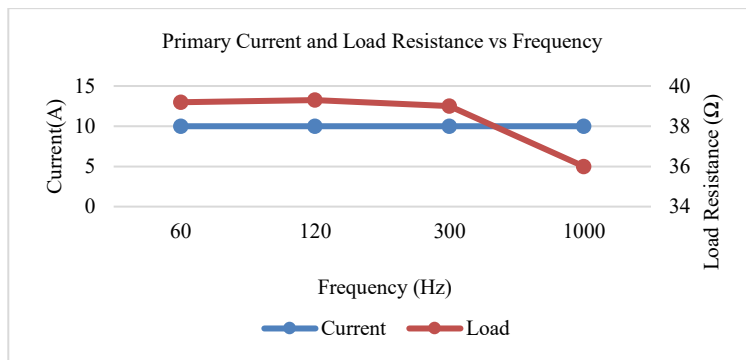


Fig 2. 15 The measured transformer primary current while the input voltage is set to 170V with a constant current and variable resistive load while fundamental frequency changes from 60Hz to 1kHz

Table 2. 5 The simulation results on transformer core and winding temperature increase under constant current condition

Core temperature increase (°C)				
Frequency (Hz)	60	120	300	1000
Simulation	43.27	47.8	66.9	136.9
Winding temperature increase (°C)				
Frequency (Hz)	60	120	300	1000
Simulation	47.03	57.2	71.7	125

2.3.3. Experimental results on performance evaluation of the grid emulator

This subsection evaluates the grid emulator performance in terms of THD and the control bandwidth after connecting to a transformer. The THD associated with the amplifier and transformer are measured using the power analyzer. For this case, the reference phase voltage of the amplifier is set as 170 V peak under the load of 10 A_{RMS} while the operating frequency is changing from 50 Hz to 3 kHz. Fig 2.16 (a) presents the measured THD from the phase A current of the amplifier, and Fig 2.16 (b) presents the measured THD from the phase A current at the transformer secondary side. It can be seen that the THD reduces in the transformer's secondary side compared to the one at the amplifier output.

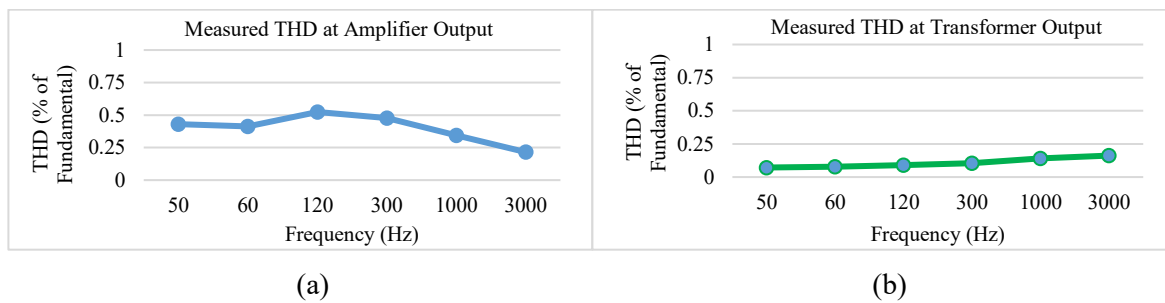
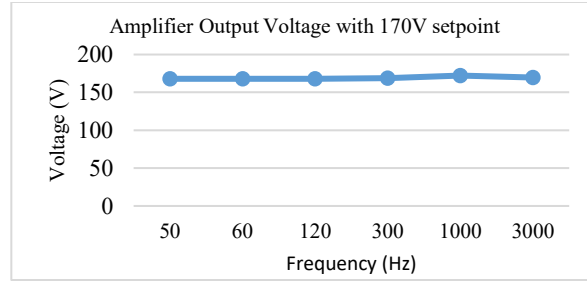
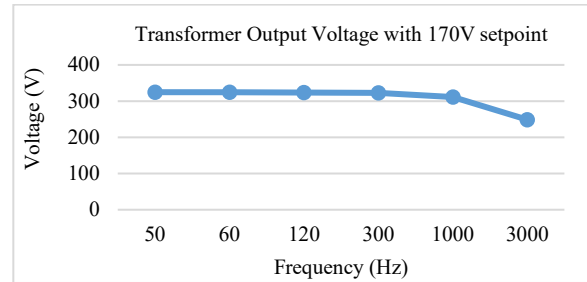


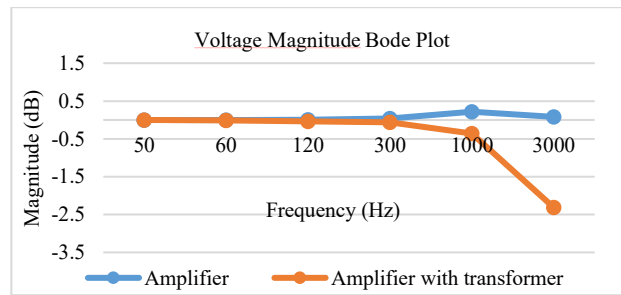
Fig 2. 16 (a) The measured THD when the phase voltage is 170 V peak at load current of 10A_{RMS} and the fundamental frequency changes from 50 Hz to 3 kHz. (a) Measured THD from the output of the amplifier. (b) Measured THD from the output of the transformer



(a)



(b)

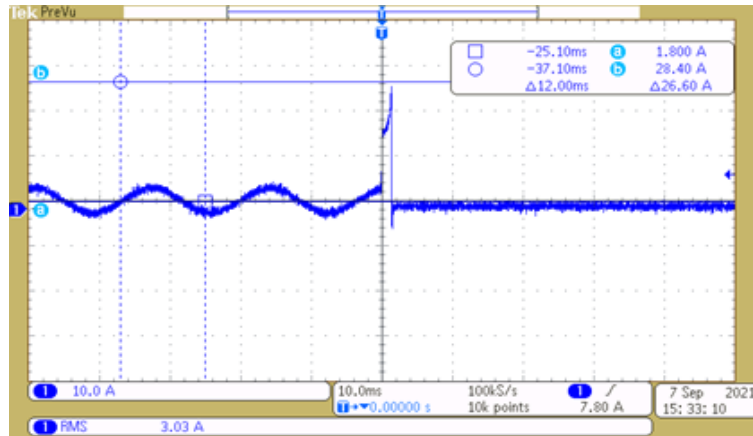


(c)

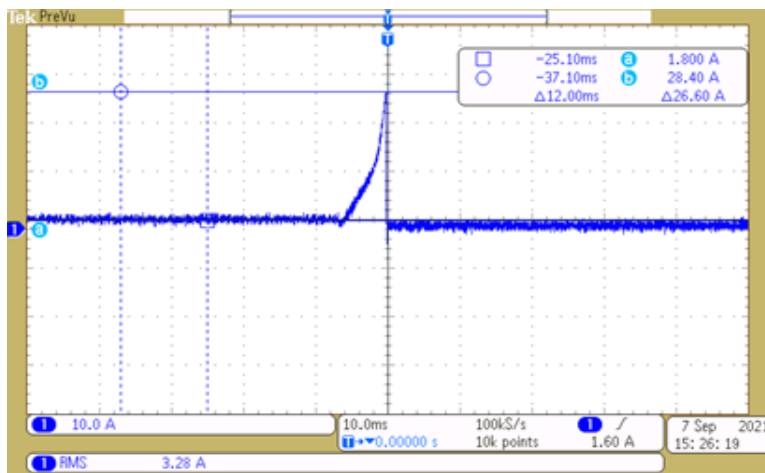
Fig 2. 17 The measured bandwidth when the voltage is 170 V peak at load current of $5A_{RMS}$ and the fundamental frequency changes from 50 Hz to 3 kHz. (a) Measured bandwidth from the output of the amplifier. (b) Measured bandwidth from the output of the transformer (c) The measured bandwidth from the output of the amplifier and the secondary side of the transformer

Another important performance indicator is the control bandwidth. Connecting a transformer to the amplifier output would potentially affect the amplifier bandwidth. For this investigation, the phase voltage reference of the amplifier is set to the maximum value of 170 V peak while the frequency of operation is changing; the voltage magnitudes at both the amplifier output and the secondary side of the transformer are measured and presented in Fig 2. 17 (a) and Fig 2. 17 (b), respectively. The obtained results from Fig 2. 17 (a) and Fig 2. 17 (b), are rescaled to dB and Fig 2. 17 (c) presents the bandwidths associated with the amplifier and transformer outputs. It can be observed that the bandwidth of the grid emulator system has been affected by

the transformer interconnection, and it has been reduced to about 3 kHz according to the results presented.



(a)



(b)

Fig 2. 18 (a) Phase current waveform under a voltage step change of amplifier from 30V to 170V at the fundamental frequency of 60Hz. (b). Phase current waveform under a voltage step change of amplifier from 0V to 60V at the fundamental frequency of 60Hz

Lastly, tests are conducted to investigate the startup performance of the grid emulator system as the transformer could cause an inrush current under this condition. More specifically, during startup, the primary side of the transformer draws a high amount of current from the amplifier. This, in turn, creates an inrush current at the amplifier terminal, which creates a fault in the amplifier. Fig 2.18 (a) and Fig 2.18 (b), show the test results under two different voltage step change conditions. With a high inrush current, the amplifier enters the over current fault condition. For this study, the selected amplifier has a protection circuit that fully protects the amplifier.

However, this effect can cause permanent damage to the other components in the grid emulator system.

2.3.4. Experimental results on inrush current mitigation

The inrush current time is calculated to be 0.4 seconds using Equation (6). This time is used to design the ramp time. Figure 2.19 illustrates the simulation results of transformer currents with two different ramp times: 0.1 seconds in Fig. 2.19 (a) and 0.4 seconds in Fig. 2.19 (b). It can be observed that if the ramp time is set shorter than the inrush current time, the inrush current will still occur in the grid emulator system, potentially damaging the grid emulator or the device under test (DUT).

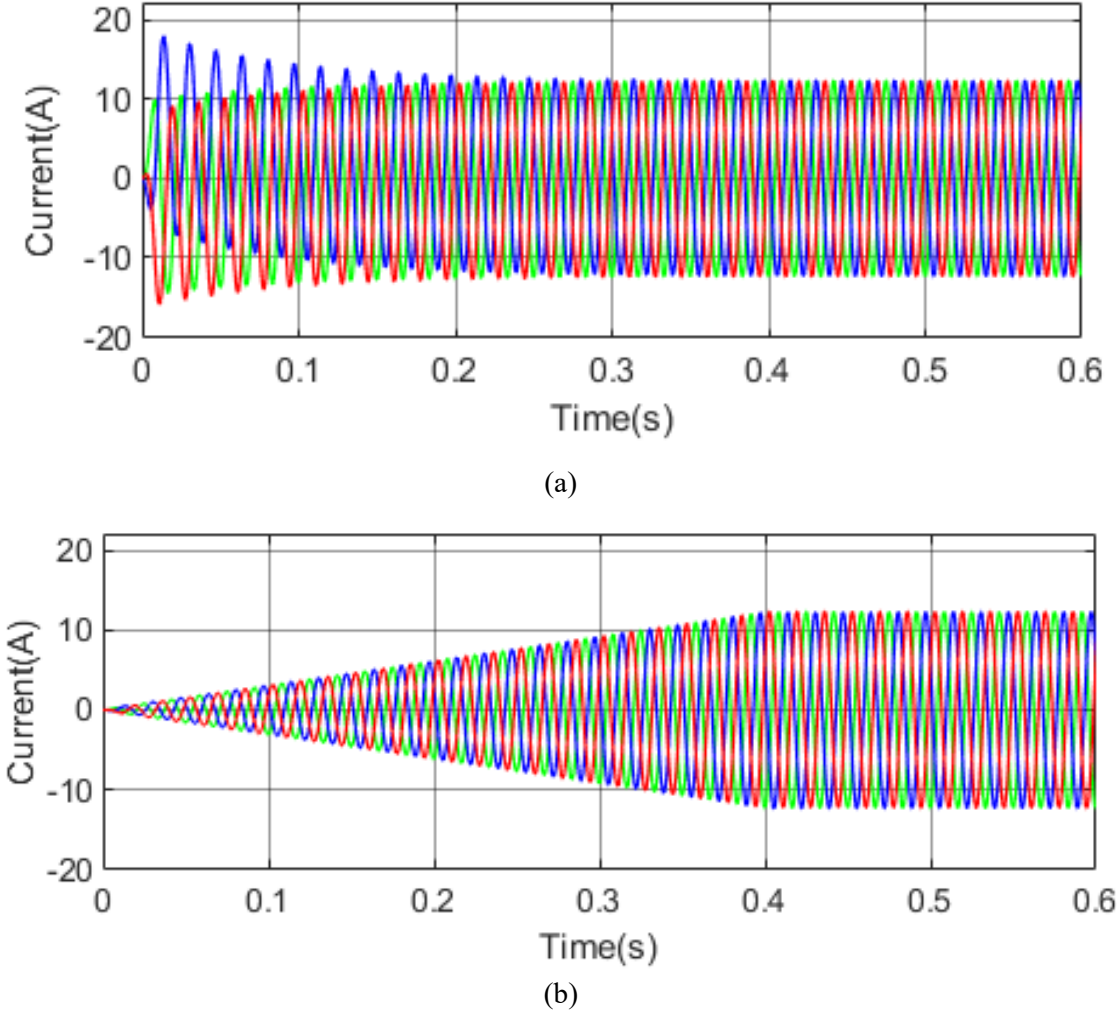
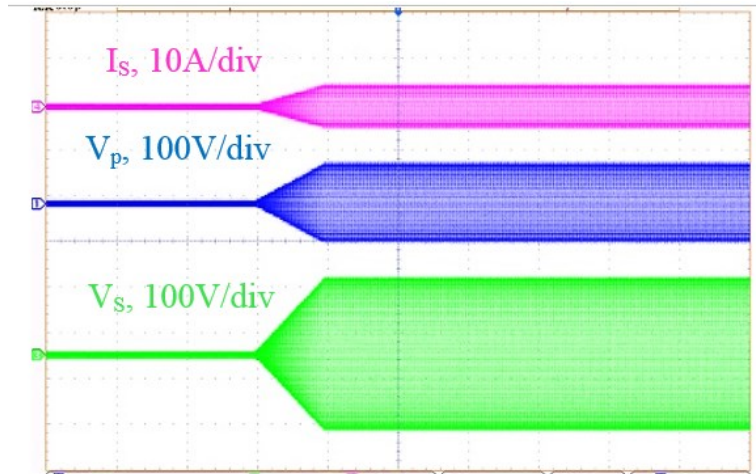
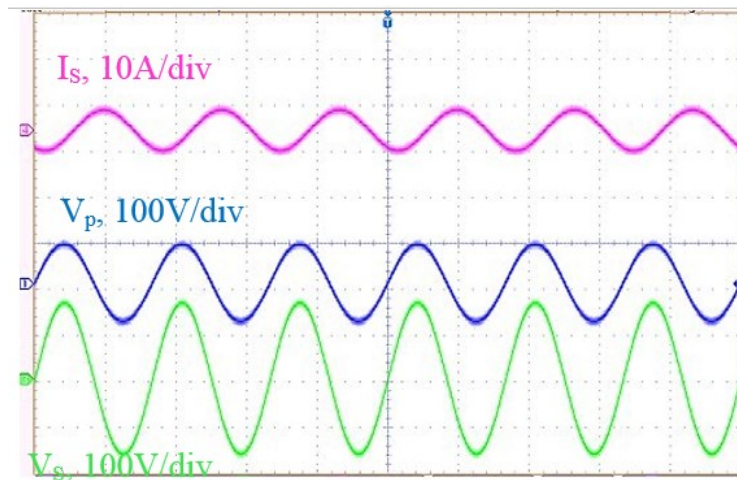


Fig 2. 19 The transformer is energized using the proposed soft magnetizing method with different ramp times. (a) Ramp time: 0.1s. (b) Ramp time: 0.4s

Fig.2.20 (a) presents the transient results when a resistive load is connected as a DUT, with a zoomed-in version of the same result in Figure 2.12(b). It can be observed that the soft magnetizing technique works properly in this condition.



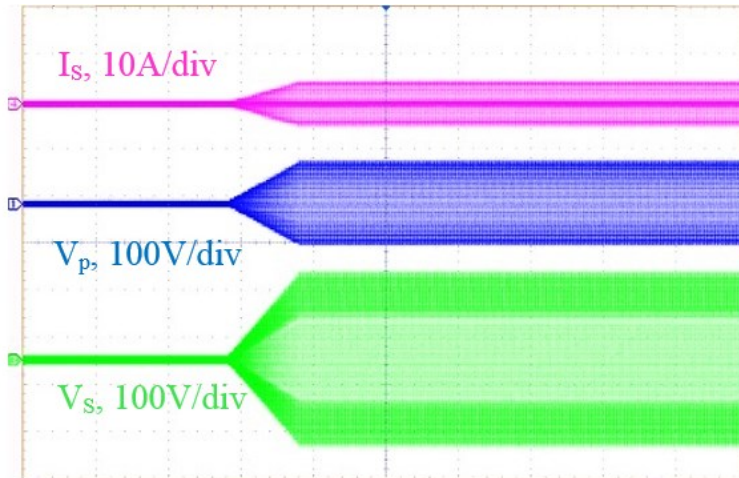
(a)



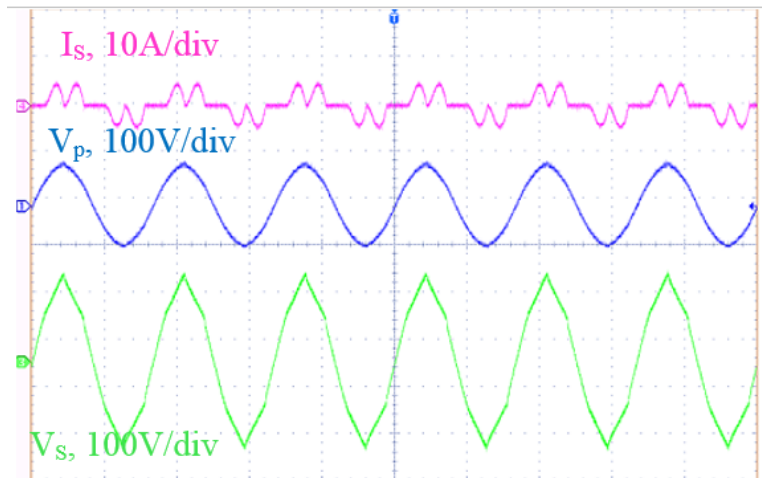
(b)

Fig 2. 20 The transformer is energized using the proposed soft magnetizing method step change from 0 to 60V at the fundamental frequency of 60Hz, Transformer secondary side phase current (I_s , top pink line), Transformer primary side voltage (V_p , middle blue line), and secondary side voltage (bottom green line). (a) resistive load (b) resistive load zoom version

Fig 2.21 (a) shows the results obtained when a diode bridge rectifier (nonlinear load) is connected to the secondary side of the transformer, with the zoomed-in version in Figure 2.20 (b). It can be seen that the proposed configuration operates properly under these conditions as well.



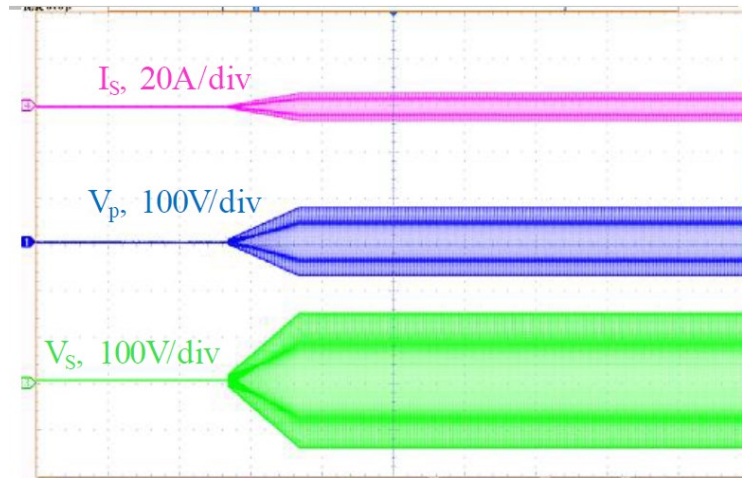
(a)



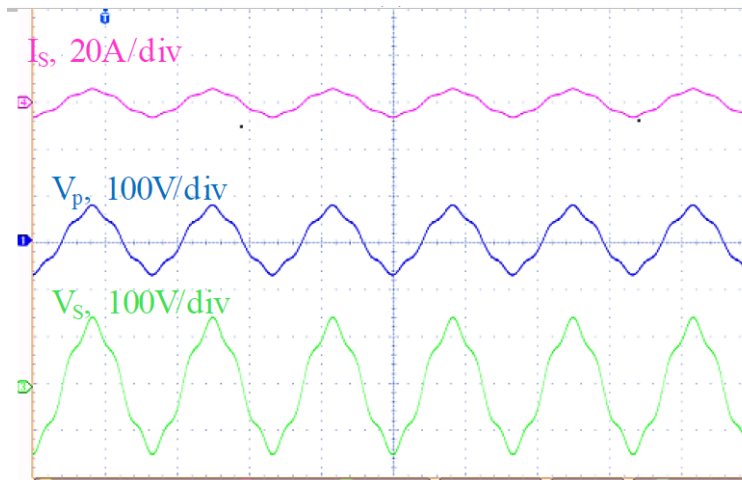
(b)

Fig 2. 21 The transformer is energized using the proposed soft magnetizing method step change from 0 to 60V at the fundamental frequency of 60Hz, Transformer secondary side phase current (I_s , top pink line), Transformer primary side voltage (V_p , middle blue line), and secondary side voltage (bottom green line). (a) nonlinear load (b) nonlinear load zoom version

Figures 2.22 (e) and 2.22 (f) show the measured results when the 5th order harmonic is injected from the grid emulator into the step-up transformer. Both the transient response and steady-state results are measured, indicating that the secondary side voltage is similar to the primary voltage.



(a)



(b)

Fig 2. 22 The transformer is energized using the proposed soft magnetizing method step change from 0 to 60V at the fundamental frequency of 60Hz, Transformer secondary side phase current (I_s , top pink line), Transformer primary side voltage (V_p , middle blue line), and secondary side voltage (bottom green line). (a) grid harmonic (b) grid harmonic zoom version

2.4. Summary

This chapter presents the investigations on a grid emulation system with a transformer connected power amplifier for emulating a grid with a voltage level higher than the amplifier rating. It is found that the interconnection of a transformer at the output of a power amplifier affects the operation of both the amplifier and the transformer. The experimental investigations first verified the functionality of the proposed grid emulation system, demonstrating that the system can operate properly under both steady-state and transient conditions. Subsequently, the DC offset

generated by the power amplifier was characterized before conducting thermal analyses on the transformer winding and core temperatures. It was found that the DC offset component remains nearly constant under different operating conditions, including load changes, voltage changes, and different frequencies. The transformer temperatures decrease slightly when the operating frequency increases from 60 Hz to 1 kHz. Lastly, the performance of the grid emulator was studied in terms of THD, control bandwidth, and startup currents. It was found that with the step-up transformer, the output THD reduces slightly, but the control bandwidth is also reduced, leading to a decreased operating frequency of the grid emulation system. More importantly, the transformer inrush current can cause the amplifier to fault when there is a step change in the reference voltage. Therefore, a soft magnetizing method is proposed to ensure the safe operation of the grid emulator with the step-up transformer under different conditions, including grid harmonics, resistive loads, and nonlinear loads.

Chapter 3 Comparative study on machine emulation systems based on linear power amplifiers and switching converters

Power hardware-in-the-loop based motor emulation system is attracting research attention in recent years as it can enhance electric machine and drive testing. This chapter analyzes machine emulation systems based on three mainstream hardware technologies to compare their performance and limitations. The first emulator system uses a conventional IGBT based hard switching power converter, the second one uses a high bandwidth soft switching power converter and the last one uses a linear amplifier. Detailed configuration and control descriptions for these three machine emulator systems are first presented. Comparative experimental studies are then conducted based on the emulation of a laboratory induction machine (IM) using these three different emulator systems. Moreover, experimental results obtained from the emulators are compared against the experimental results of the physical IM to verify their emulation performance. Finally, obtained results from these configurations.

3.1. Configurations and fundamentals of the emulator systems

This section first presents the general description and common settings for IM emulation, which will be investigated in this chapter. Then, three different motor emulation configurations namely motor emulation system with an IGBT inverter, power amplifier, and linear power amplifier, will be designed and explained in detail. Some theoretical comparative analysis will be provided between these three configurations.

3.1.1. Motor emulation system description

A general schematic diagram of the PHIL based IM emulator system is presented in Fig 3.1. The main objective of this motor emulation system is testing the grid connected induction machine. The IM machine emulator block diagram mainly consists of a machine emulator block and a RTS block. The filter element (L_f) connects the emulator converter to the grid. Different converters or linear power amplifiers can be selected as an emulator converter in order to mimic the machine behavior.

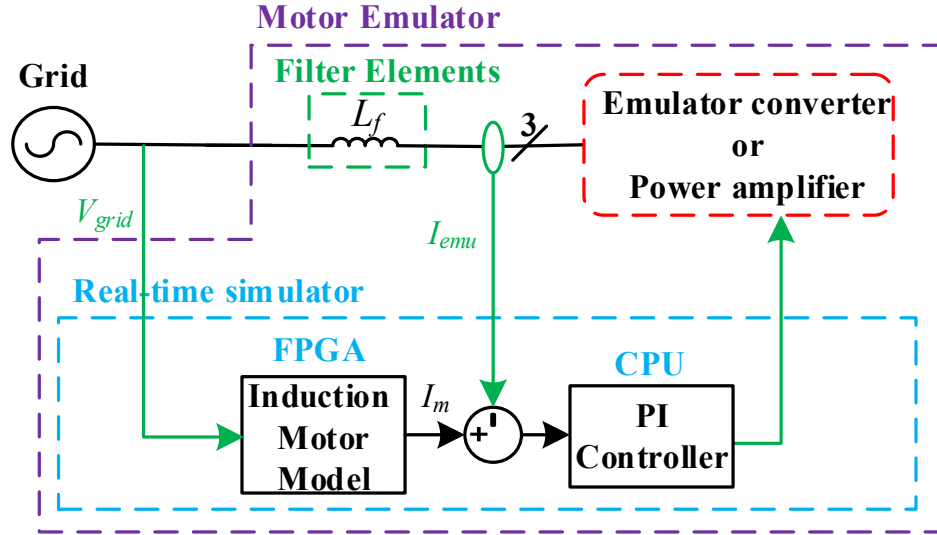


Fig 3. 1 Machine emulator block diagram

The three phase grid voltages (V_{grid}) are measured by the voltage sensors and fed into the mathematical model of the IM. The induction machine model is implemented in the RTS. The OP4510 real time simulator is selected for implementation of the motor model and the current controller. The OP4510 has FPGA and CPU core. Implementing the model on the CPU cores is simpler than FPGA board. The CPU cores have a higher computation time step (15–20 μ s) as compared to the FPGA board (500 ns). The higher computation time step results in a higher delay which leads to a less accurate motor emulator system. Hence, the machine model is implemented in the FPGA board.

To mimic a grid connected IM behavior, the emulator has to deliver the same current as in the real machine. To this end, the motor current (I_m) from the IM model is used as the reference current, and the emulator current (I_{emu}) will be controlled to follow I_m through the current controller by regulating the emulator converter or linear power amplifier. The proportional integral (PI) controller is selected for current control, and it is implemented in the CPU for all three cases.

3.1.2. Motor emulation system with an IGBT inverter

In the inverter based IM emulator system, a standard two level IGBT based voltage source converter (VSC) is used for the realization of the emulator converter. Fig 3. 2 presents the circuit diagram of the IGBT inverter for machine emulation. In this condition, a standard sine triangle PWM technique can be used after the current controller to generate the gating signals for the IGBT inverter for machine emulation.

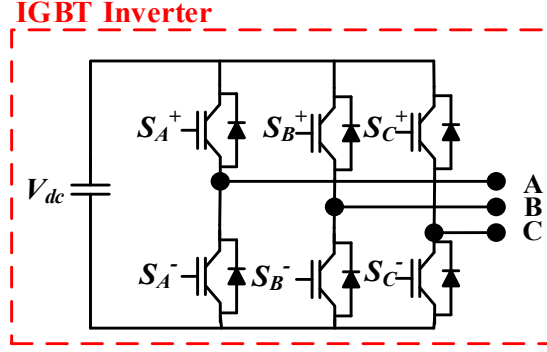


Fig 3. 2 IGBT inverter for machine emulation

The controller is designed in a manner to have a high emulation bandwidth for the IM emulation system. This design exercise has been considered for this configuration. The same can be applied to any inverter based motor emulator configuration. The IGBT inverter is selected to have a 20 kHz switching frequency therefore T_D is considered to be half of the inverter switching frequency (50 μ s) and also a DC link voltage of 300 V, which yields a DC link voltage gain (G) of 150V. A simple first order filter approximation is used for the current sensor with a gain of unity and a time constant T_f of 40 μ s. Furthermore, the sampling time of the digital controller T_s is 20 μ s. R_f and L_f correspond to the resistance and inductance of the link filter, and they are 300 m Ω and 2.5 mH, respectively. The PI controller integral gain is K_i and T_p is K_p/K_i . The PI controller zero is positioned to cancel this L filter pole, as it is the slowest pole. The open loop transfer function of the emulator converter current loop can be derived as (3-1).

$$G(s)_{sw_OP} = \frac{K_i(T_p s + 1)}{s} \frac{G}{1 + s(T_s + T_D)} \frac{1/R_f}{1 + s \frac{L_f}{R_f}} \quad (3-1)$$

The correspondence close loop transfer function of the emulating converter current loop can be derived as (3-2).

$$G(s)_{sw} = \frac{\frac{K_i G (1 + s T_f)}{R_f (T_D + T_s + T_f)}}{s^2 + \frac{s}{T_D + T_s + T_f} + \frac{K_i G}{R_f (T_D + T_s + T_f)}} \quad (3-2)$$

The bandwidth of the system can be calculated as (3-3) by comparing (3-2) with a standard second order transfer function.

$$BW = 2\zeta\omega_n = \frac{1}{T_D + T_s + T_f} \quad (3-3)$$

The critically damped response for the desired bandwidth can be achieved by considering the damping factor (ζ) is 0.707. Therefore, by knowing the values of T_D , T_S and T_f , the emulator bandwidth can be calculated as 1000Hz. The open loop magnitude and phase plots for the emulator current control loop are shown in Fig 3. 3. The designed current controller ensures a positive gain margin and thus, the stability of the emulator system.

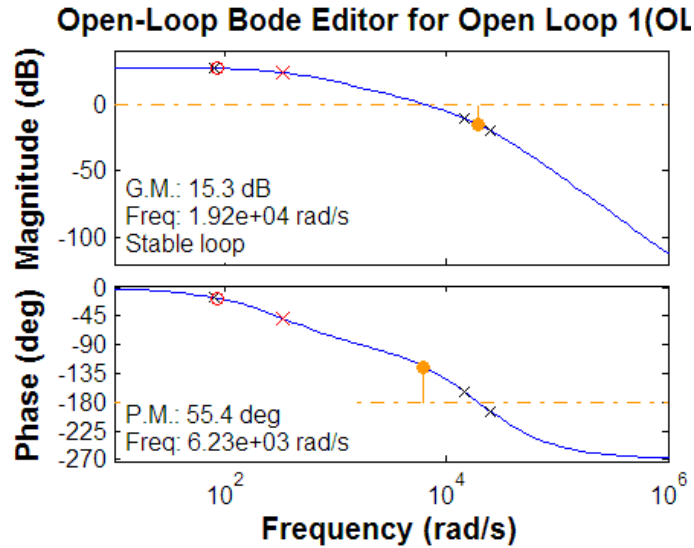


Fig 3. 3 Open loop magnitude and phase plots for the emulator current control

3.1.3. Motor emulation system with power amplifier

The power amplifier is selected for the emulator converter due to its high performance and high bandwidth specification. This motor emulation configuration also ensures the current which is drawn by the emulator system is equal to the IM model current output. Fig 3.4 shows the schematic diagram of the power amplifier used as an emulator converter [65]. Fig 3.1 structure can still be used in this condition by only replacing the emulator converter with this power amplifier. The control of the amplifier is implemented in the RTS system as shown in Fig 3.4. An extra filter (L_f) element is not required for this case as the power amplifier has been designed to have an output filter as shown in Fig 3.4. Moreover, the more specific point about this design is the selected power amplifier can work in the current control mode of operation. Therefore, there is no need to design the custom-made current controller. Therefore, the IM model generates the current reference for the power amplifier directly. The selected power amplifier has a current controller bandwidth of 10 kHz.

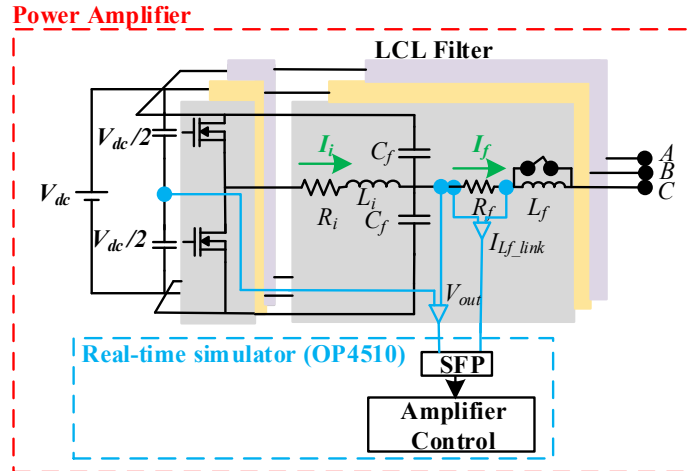


Fig 3. 4 Power amplifier with soft switching for machine emulation

3.1.4. Motor emulation system with linear power amplifier

The schematic diagram of the linear amplifier used for machine emulation is shown in Fig 3. 5 [73]. For this configuration, the linear amplifier is acting as a physical machine and each phase of the machine is emulated by one linear power amplifier. These linear amplifiers are connected in a star configuration. The linear amplifier provides high bandwidth which enables the emulator system to mimic the motor transient behavior. The filter element connects the linear amplifier to the grid as shown in Fig 3.5.

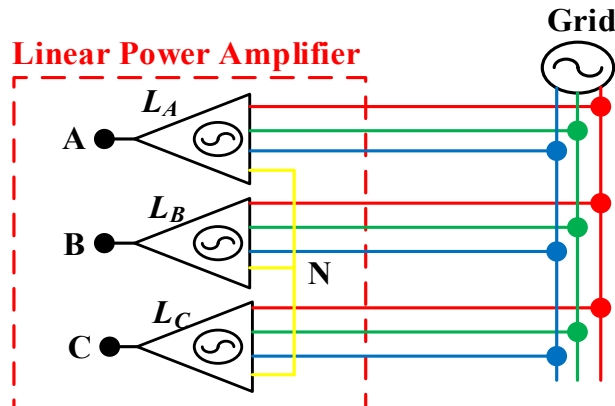


Fig 3. 5 Linear power amplifier for machine emulation

The emulator current controller is designed to have as high a bandwidth as possible, which ensures all the current harmonics can be emulated. The PI current controller is designed for the open loop transfer function in (3-4). The selected linear amplifier has a bandwidth of 40 kHz at the full voltage scale with a delay of 600 ns. The total linear amplifier delay is defined as T_d . The T_d value is 1 μ s. Also, the linear amplifier has a gain (G) of 20. The link filter is represented by the

resistance (R_f) and inductance (L_f) in the transfer function. The current sensor is approximated as a first order transfer function with a time delay of T_s equal to 1.5 μ s. Therefore, the open loop transfer function for the emulation system can be written as

$$G(s)_{EMU} = \left(K_p + \frac{K_I}{s}\right) G e^{-sT_d} \frac{1/R_f}{1 + s L_f/R_f} \frac{1}{1 + sT_s} \quad (3-4)$$

The magnitude and the phase plots of the emulator current control open loop transfer function are presented in Fig 3.6. The designed current controller ensures a positive gain margin and thus, the emulator control loop stability. The current controller is designed to have a bandwidth of 7.5 kHz.

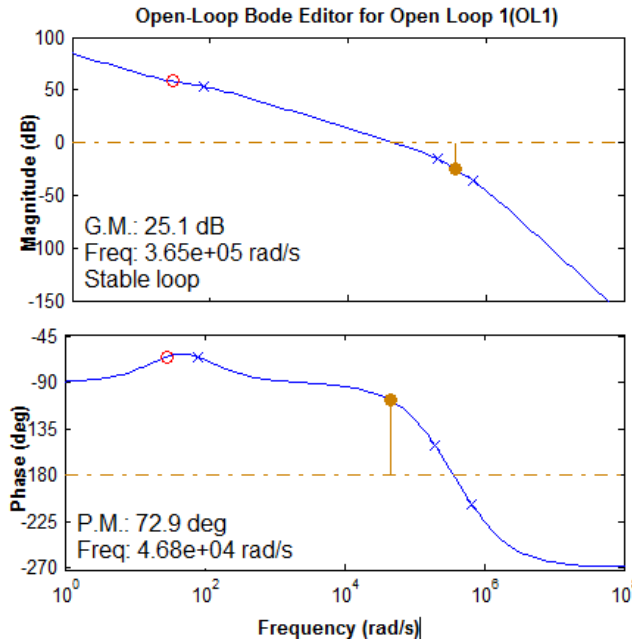


Fig 3. 6 Open loop bode plots design for the current controller of the linear amplifier based emulator system

3.1.5. Comparative analysis between three emulation systems

The previous sections designed and explained the three different hardware technologies and configurations for IM emulation. As discussed, the maximum achievable bandwidth using conventional IGBT inverters for a machine emulator system is limited by the switching frequency of the converters. For performing high-accuracy emulation, the bandwidth of the emulation should also be sufficiently high. In this regard, a high bandwidth linear power amplifier-based emulator configuration has been presented. In the hard switch inverter-based emulator system, the emulator

bandwidth depends on the inverter switching frequency. Although high switching frequency devices, such as silicon carbide (SiC) and gallium nitride (GaN) switches are available for power electronics converters, the IGBT is still the most popular choice for inverters at this stage. Therefore, only the IGBT based inverter with a switching frequency of 10 kHz is implemented in the IM emulation system for comparative studies in this chapter. The power amplifier/linear amplifier in the current market can offer higher bandwidth for motor emulation. For this comparative study, the current controller bandwidths for the IGBT inverter, power amplifier, and linear amplifier based emulators are 1 kHz, 10 kHz, and 7.5 kHz, respectively. Therefore, using the linear/ power amplifiers can offer 7.5/10 kHz bandwidth which is almost 10 times of the IGBT inverter based configuration. Thus, it is expected that the IGBT inverter based emulator system due to the lower bandwidth will lead to a slower response in the emulated current, and its influence will be more severe in high speed/frequency machine emulation conditions. Moreover, the designed controller bandwidth determines the motor frequency range that can be emulated, ie. the 10 kHz bandwidth can be used for emulating a machine up to 10 kHz. Therefore, the IGBT inverter based machine emulator system has limited capability in emulating high speed/frequency machines as compared with the power/linear amplifier based emulation system.

In addition, since the controller bandwidth determines the motor current frequency that can be controlled. The IGBT inverter based machine emulator with limited bandwidth will not be able to emulate/control the harmonic currents at higher order. Therefore, the harmonics due to inverter dead time may not be attenuated in the IGBT inverter based emulator without additional harmonic current controllers. The inverter dead time phenomena introduce the 5th and 7th order harmonics in the emulated current, which will be shown in the test results. For this reason, the IGBT motor emulation configuration may not be able to mimic the machine behavior accurately. However, in the linear/ power amplifier based configurations, the dead time effect do not exist.

When selecting a simulator for Power Hardware-in-the-Loop (PHIL) applications, several factors such as the type of application, integration with hardware, simulation fidelity, and latency must be considered. The PEER Group Lab uses OPAL-RT, widely regarded as one of the best choices for PHIL applications, due to its flexibility, low latency, and the integration of both FPGA and CPU capabilities enabling high-fidelity simulations of complex and multi-domain systems such as power systems, power electronics, and renewable energy applications. Its FPGA-based acceleration ensures minimal delays between the simulation model and the connected hardware,

making it highly suitable for real-time applications where precise and rapid responses are required. Its open architecture also allows seamless integration with external hardware and control systems, making it highly versatile and suitable for a wide range of PHIL scenarios. On the other hand, Typhoon HIL is specifically optimized for power electronics and electrical grid simulations, offering real-time capabilities with high accuracy and extremely low latency, particularly for converter testing and renewable energy systems. It provides fast computation, making it ideal for testing switching devices, controllers, and fast dynamic behaviors with minimal delays. However, it may be less suited for large, complex power system simulations. Meanwhile, dSPACE excels in automotive and aerospace applications, making it an excellent choice for PHIL setups focused on motor control systems or electric vehicles. While it offers low latency in control applications, it may not scale as efficiently for large power system simulations compared to OPAL-RT, which can introduce additional latency for more complex grid or multi-domain simulations. Finally, RTDS is specifically designed for large-scale power system simulations and generally offers very low latency for power grid simulations, providing highly accurate simulations of grid behavior, protection schemes, and other large power systems. However, for very fast switching operations in power electronics, it may not match the speed of Typhoon HIL or OPAL-RT. Overall, OPAL-RT stands out for its versatility, scalability, and low latency across a wide range of PHIL applications, particularly for complex power systems and renewable energy scenarios. Therefore, OPAL-RT has been selected to validate the three proposed IM emulator configurations throughout this thesis.

3.2. Experimental setups and results

This section presents the developed experimental setups and comparative results of the IGBT inverter, power amplifier, and linear amplifier based IM emulator system in start-up test condition. To evaluate the emulation results, a physical IM machine start-up test setup, and results are also presented. Detailed experimental setups and the comparative results are given in the following two subsections.

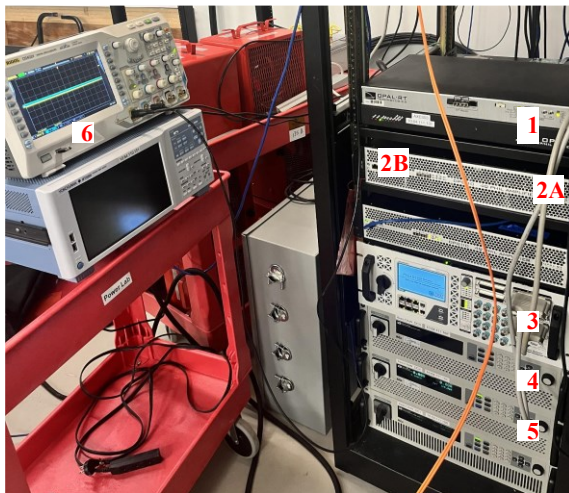
3.2.1. Experimental setups

The developed IGBT inverter based IM emulator system test bench is shown in Fig 3.7. The standard two level IGBT inverter is selected as an emulator converter in this experiment. The DC power supply is used to supply the DC link of this inverter. The emulator converter is

connected to the grid emulator (power amplifier) through a 2.5 mH inductor. The control for the emulator converter is implemented in RTS, also shown in Fig 3.7 in order to maintain safe grid voltages. The bi-directional DC power supply maintains a constant 500 V DC to the power amplifier input. As explained earlier the machine mathematical model is implemented in the FPGA board of the RTS to reduce the sampling time. The data acquisition is selected for recording the data.

The experimental setup of the power amplifier-based IM emulation system is also shown in Fig 3.7. There are two power amplifiers with one working in the voltage mode of operation as a grid emulator, and the other one operating in current control mode to mimic the machine behavior. The power amplifier control is programmed in RTS through the SFP link. The bi-directional DC power supply is used to power these two power amplifiers. The same IM model and the same data acquisition are used in this experiment.

The developed experimental setup of the linear amplifier based IM emulator system is shown in Fig 3.8. The three linear amplifiers [73] are used to emulate each of the machine phases. The linear amplifiers are connected to the link inductor with a value of 2.5mH. The control of amplifiers and machine model are implemented in RTS. The protection circuit board is designed to disconnect the amplifier from the grid in the event of overcurrent. The isolation transformer is used to avoid the circulation of the current from the grid to the linear amplifier. It is important to mention that these experimental tests were conducted using the setup described in [38]-[41].



- (1) Real time simulator (RTS)
- (2A) Power amplifier for grid emulation
- (2B) Power amplifier for machine emulation
- (3) IGBT inverter
- (4) Bi-directional DC power supply for the power amplifier
- (5) DC power supply for inverter
- (6) Data acquisition

Fig 3. 7 Experimental setup of IM emulator system with (1), (2A), (3), (4), and (5) used for IGBT inverter based emulator system, and (1), (2A), (2B), (4) and (6) used for power amplifier based emulator system

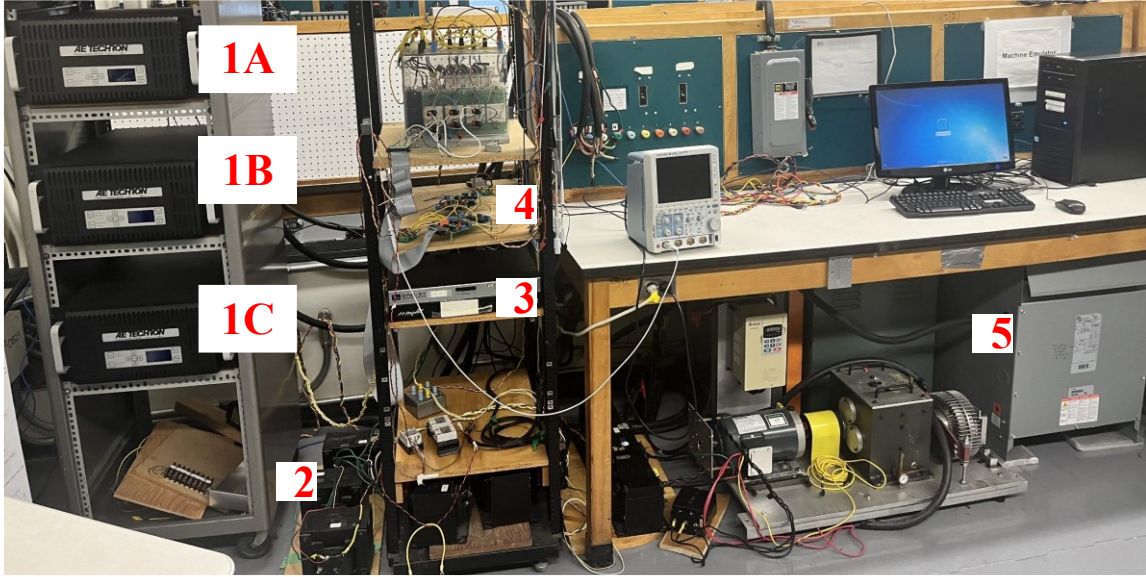
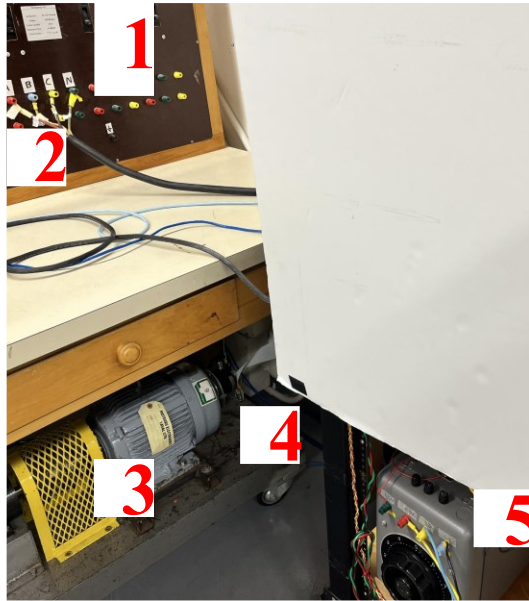


Fig 3. 8 Experimental setup of the linear amplifier-based IM emulator system. (1) Linear amplifiers (2) link inductors (3) real time simulator (4) protection circuitry (5) isolation transformer

Table 3. 1 Squirrel cage induction machine parameters

Parameter	Value
Rated power	5 hp
Rated current	16 A
Rated voltage	220 V
Stator resistance, R_s	0.9649 Ω
Rotor resistance, R_r	1.3046 Ω
Stator reactance, X_{ls}	1.8990 Ω
Rotor reactance, X_{lr}	4.4164 Ω
Mutual reactance, X_M	76.5378 Ω
Moment of inertia, J_M	0.0138 Kg.m ³
Viscous friction coefficient, B	0.0021

The experimental setup of the physical squirrel cage IM is shown in Fig 3. 9. The IM is 5 hp, and it is connected to the grid through the circuit breaker. The encoder is used to measure the IM speed. The machine parameters are listed in Table 3.1, which has been used in the machine model for IM emulation.

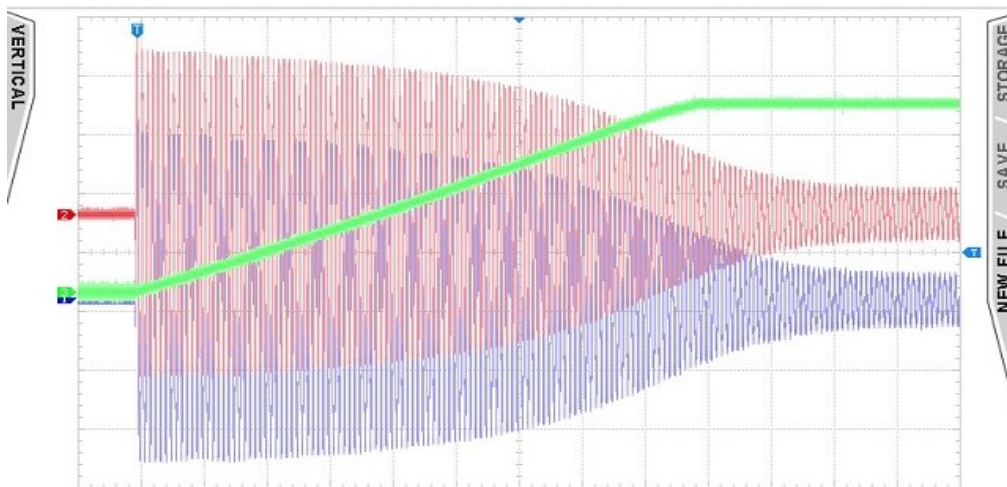


- (1) Circuit breaker
- (2) Three phase grid
- (3) Squirrel-cage IM
- (4) Speed sensor
- (5) Autotransformer

Fig 3. 9 Experimental setup for the physical IM

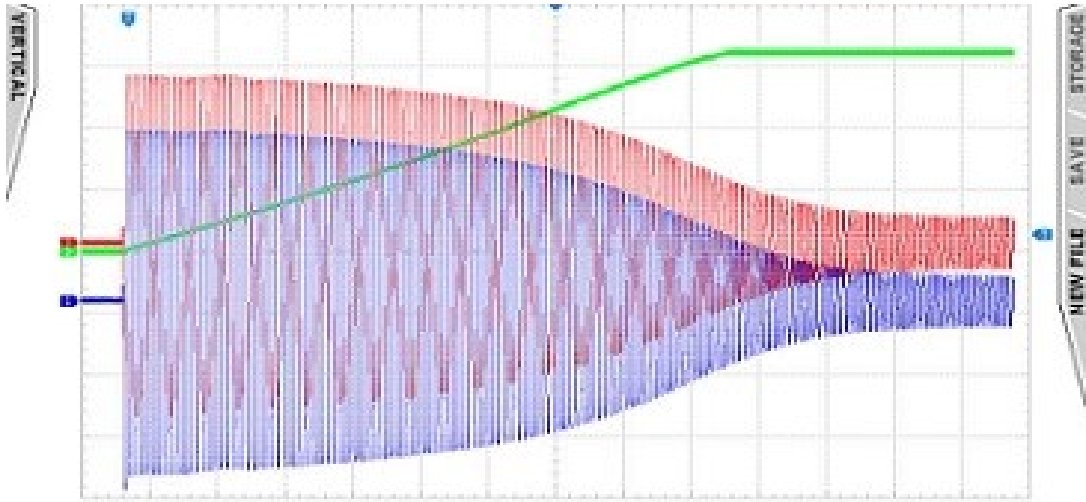
3.2.2. Comparative result

In this section, the results obtained from different IM emulator setups followed by physical IM will be presented. Fig 3. 10(a) presents the results obtained from the IGBT inverter based IM emulator system. Fig 3.10 (b) shows the measured results from the power amplifier based IM emulator system. Fig 3.10 (c) represents the results obtained from the linear amplifier based motor emulator system. The applied voltage to the machine terminal is 35V.

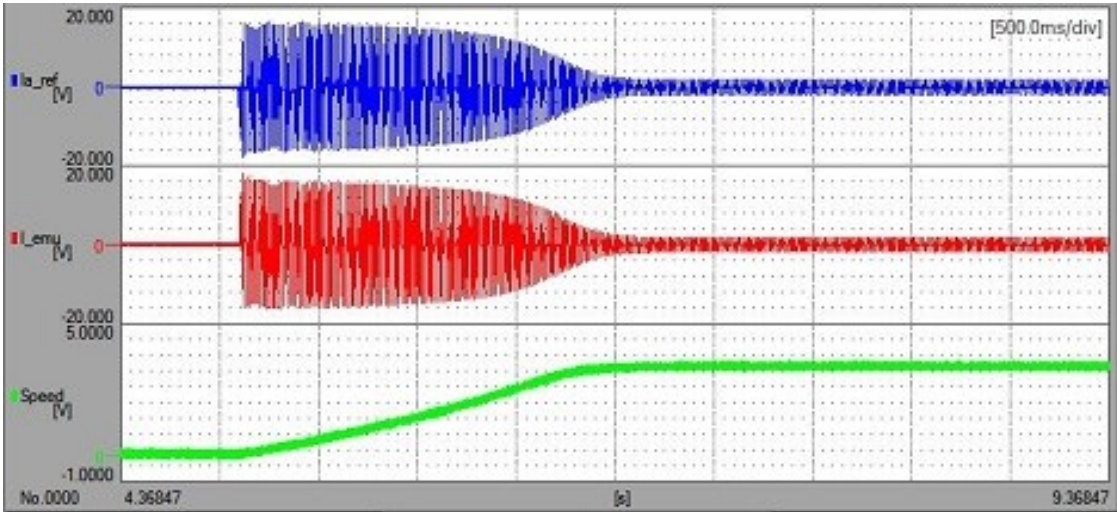


(a)

The virtual machine speed and current within the simulator are measured as well as emulated current for all these configurations. As can be seen from the results, the emulated currents can closely follow the virtual machine current. Fig 3.10 (d) presents the measured current and speed results from the physical IM start-up condition.



(b)



(c)

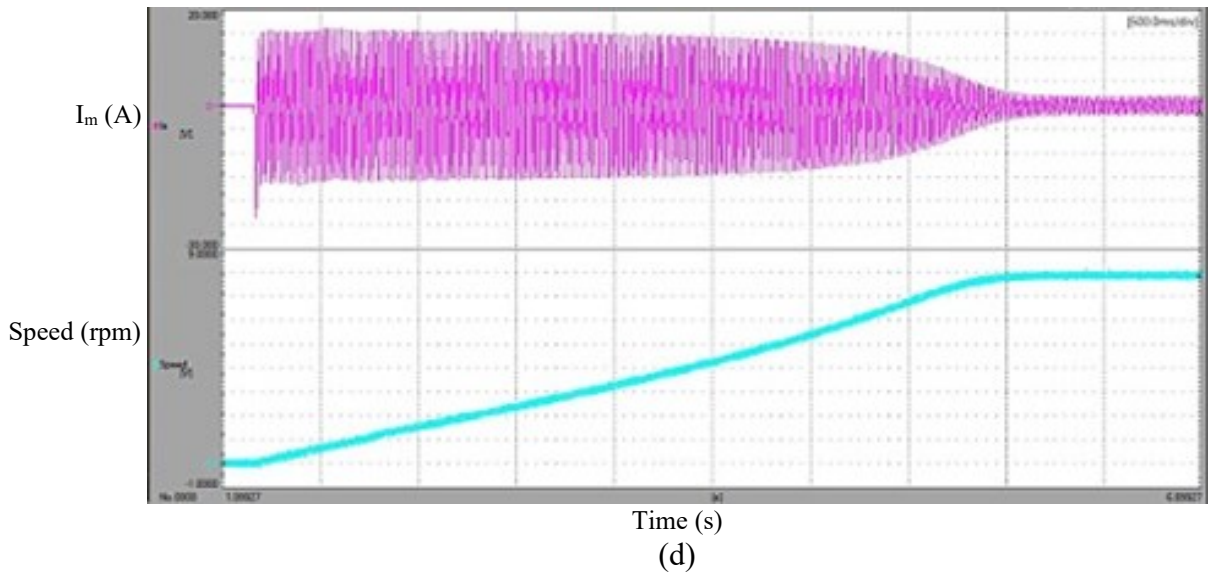


Fig 3. 10 The Experimental results obtained from IM startup condition (a) IGBT based emulator (b) power amplifier based emulator (c) linear amplifier based (d) physical IM (blue emulated machine phase A current, red reference current for emulation generated within the real-time controller, green machine speed)

The steady-state currents and motor speed results from all four test setups are plotted together and presented in Fig 3.11. It can be observed that the emulated currents from all three emulator setups match the one from a physical IM.

To further evaluate the motor emulation accuracy of all three emulator configurations, the peak fundamental components of the emulated currents are compared with the measured current in the physical machine as in Fig 3.12. It is evident that all three emulators can emulate the fundamental current component precisely. The other factor that indicates the emulator performance is the total harmonic distortion (THD) in the emulated phase currents. The objective of motor emulation is to mimic the machine's behavior. However, different control or switching harmonics may be injected into the motor emulation system because of the operation of the emulator converter/amplifier.

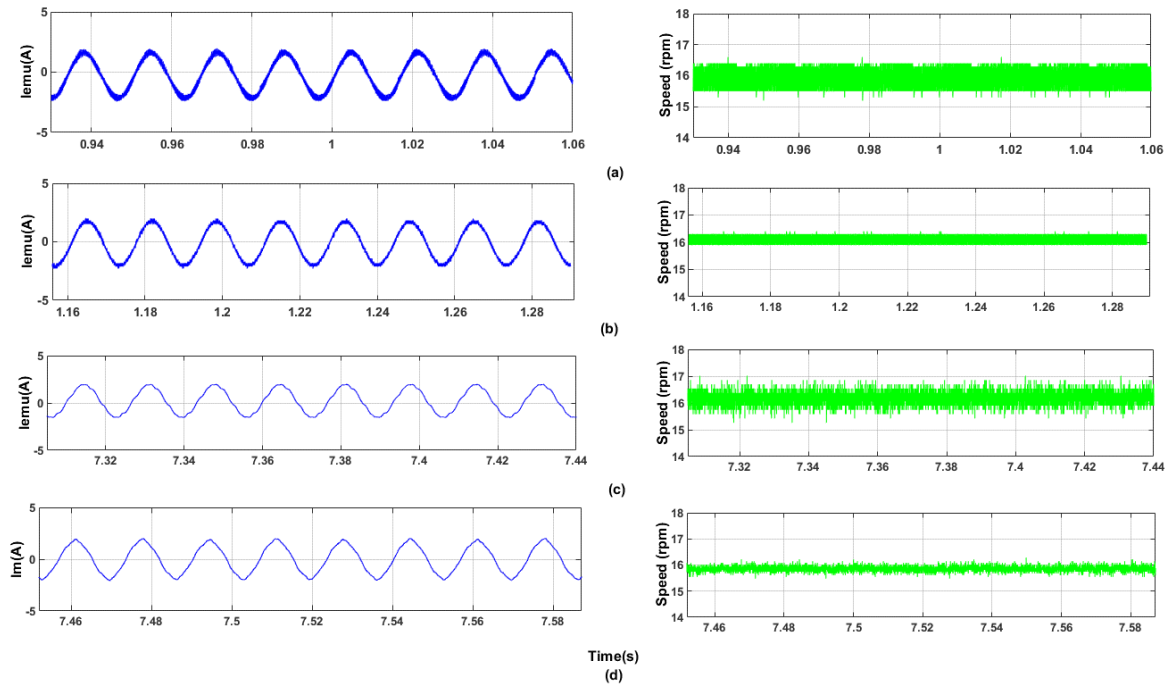


Fig 3. 11 The Experimental results obtained from IM startup condition zoom version (a) IGBT based emulator (b) power amplifier emulator (c) linear amplifier based (d) physical IM (blue emulated machine phase A current, green machine speed Scale:100rpm/div)

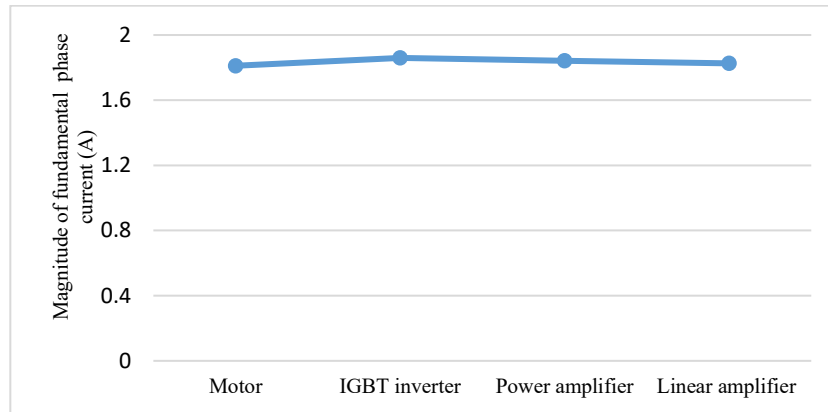


Fig 3. 12 Comparative peak fundamental current results between the physical motor, IGBT inverter, power amplifier, and linear amplifier based emulator systems

Fig 3. 13 shows the comparative analysis on the phase current THD magnitudes. It can be seen that the IGBT inverter based configuration has a higher THD percentage as compared with the linear/ power amplifier based emulator systems. Moreover, the amplifier configurations have THD values close to the one from the physical machine. Therefore, these results demonstrate the

fact that using the linear/ power amplifier based emulator configuration can increase the motor emulation accuracy and utility.

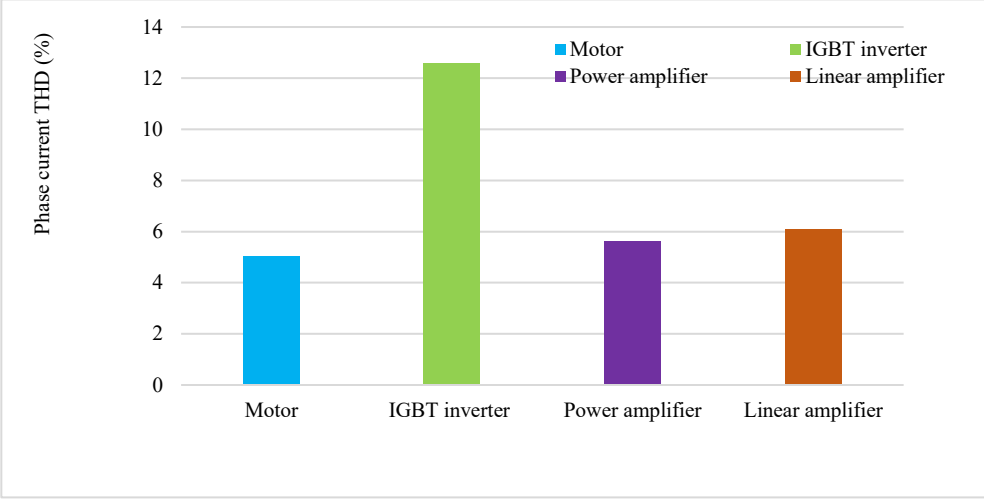


Fig 3. 13 Comparative THD% results between the physical motor, IGBT inverter, power amplifier, and linear amplifier based emulator systems

Fig 3.14 presents the harmonic analysis of the current drawn by the machine and the emulators under all three different configurations. It can be seen that the 5th and 7th harmonics are dominant in the IGBT inverter based configuration as compared to the other two emulator approaches. This is mainly because of the inverter nonlinearity effect. Therefore, using a high bandwidth power amplifier or linear amplifier can reduce this problem to a certain extent.

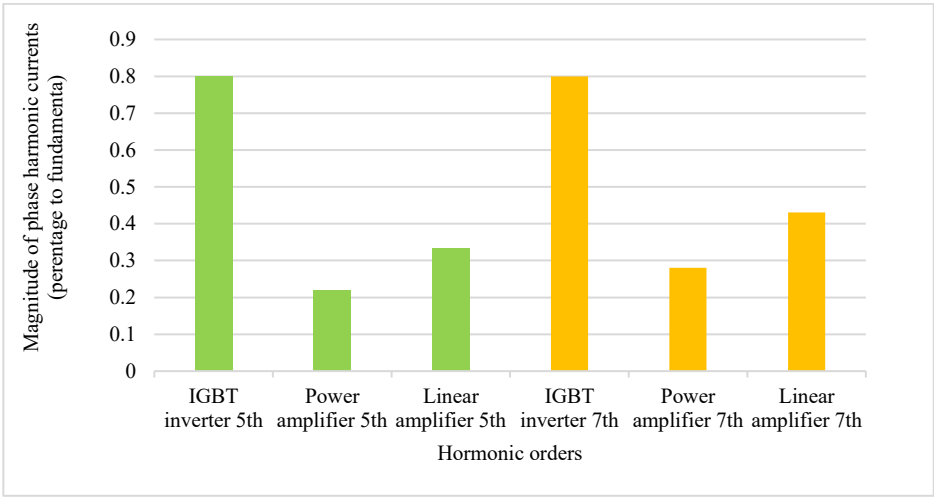


Fig 3. 14 Comparative harmonic current results between the IGBT inverter and power amplifier/linear power amplifier based emulator systems

Table 3. 2 Qualitative analysis between switched based and linear power amplifier based emulator

	IGBT inverter based	Power amplifier based	Linear amplifier based
Emulator bandwidth	Low	Highest	High
THD	High	Lowest	Low
Emulator error	Low	Low	Lowest
Flexibility	High	Low	Low
Design complexity	High	Low	Moderate
Machine speed range emulation capability	low	Highest	High
Machine power level emulation capability	Highest	High	Low
Cost	Low	High	Highest
Emulator size	Large	Small	Largest

Table 3.3 summarizes the comparative results of these three motor emulation configurations in terms of the emulator bandwidth which is designed in section 3-1, emulator THD level, and error which are quantified by the emulated current analysis against the one from the physical motor. The other aspect is configuration flexibility and design complexity which are mostly defined by emulator system design that can be/requires custom made by the end users. The IGBT inverter based configuration is considered as most flexible but more complex in comparison with the power amplifier based ones. The capabilities of the emulator in emulating the motors in terms of the power rating and speed/frequency are also compared. The motor power rating emulation capability can be determined based on the power ratings of the convertor and amplifiers available in the market, and motor speed/frequency capability can be determined based on their bandwidths. Lastly, the cost and experimental setup size of all three motor emulator systems are compared according to the actual device costs and sizes and manufacturer data available.

3.3. Summary

This chapter presented a comparative study and results on power hardware-in-the-loop IM emulator systems. Three different configurations for IM emulator startup test conditions with the IGBT inverter based approach, power amplifier based approach, and linear amplifier approach are designed and investigated. This chapter initially discussed the detailed design of each approach.

Then, the corresponding experimental setups are developed. Test results obtained from these three types of emulator configurations are analyzed and compared against the results obtained from the physical prototype of IM. It is shown that the linear/ power amplifiers can achieve the best emulator bandwidth, accuracy, THD performance, and motor emulation speed range capability, but they could be limited by design flexibility, power ratings and the high cost. The IGBT inverter based approach can be a low-cost laboratory solution towards machine emulation of a wide power range, but it will require a more complex design to tackle issues related to its bandwidth limit, high THD, and dead time harmonics.

Chapter 4 Harmonic compensation of a power-hardware-in-the-loop based emulator for induction machines

In this chapter, a PHIL-based machine emulation system is proposed for grid-tied three-phase induction machines (IM). Typically, a switched voltage source inverter (VSI) is employed as an emulator converter in the motor emulation system. However, the VSI introduces various harmonics into the motor emulation system. These harmonics are mainly attributed to dead time, switching components, and control signals. These harmonics deteriorate motor emulation accuracy. Thus, it is important to investigate and compensate for emulator converter harmonics in motor emulation systems. As an important source of these harmonics is dead time, a detailed analysis of the dead time effect on motor emulation will be presented first. Subsequently, a novel Artificial Neural Network (ANN)-based harmonic compensation technique is developed to ensure the mitigation of harmonics in the emulated motor currents. The proposed ANN-based intelligent harmonic compensator leads to the improvement of motor emulation accuracy. Experimental results are obtained from the emulator system and a squirrel cage induction motor to validate the proposed emulator with harmonic compensation.

4.1. System description of the IM emulator

The structure of the PHIL-based IM emulator system is depicted in Fig 4.1. This figure shows the main component of the emulator system as well as the block diagram of the control system. The IM emulator consists of a power electronic converter that is connected to the grid (grid emulator) through the coupling inductor or filtering inductor (L_f).

The emulator converter (EC) is a two-level three-phase voltage source converter (VSC). The objective of the EC is to draw the current from the grid following the three-phase reference currents generated by the induction motor model. More specifically, the motor model is simulated in the RTS, as the input of the motor is voltage so the grid voltage (V_{grid}) is measured and fed to the IM motor model. The virtual output d -axis and q -axis current references of the motor ($I_{m_d}^*$, $I_{m_q}^*$) are compared with the emulator input currents (I_{emu}), and then the related errors go to the proportional-integral (PI) controller; the PI controller ensures that the current which is drawn by the EC is equal to the virtual motor reference. The PI controller generates the required modulation index for the PWM module to regulate the EC operations. A standard triangle comparison-based

PWM is used for generating the PWM. The motor model, the EC controller, and the gating pulses are implemented in the RTS.

The inductor (L_f) is selected for connecting the EC to the grid. This interface element allows a simple control structure for the emulator system, the value of L_f in the emulator system is selected to be close to the motor inductance.

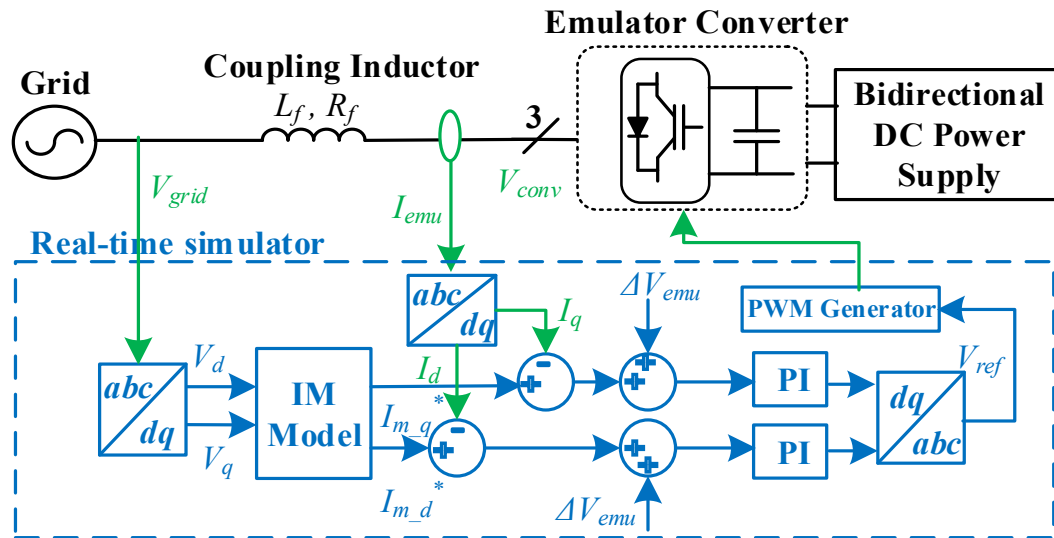


Fig 4. 1 Schematic diagram of the PHIL-based IM emulator system

The developed PHIL-based IM emulator system test bench is shown in Fig 4.2. A standard IGBT-based two-level converter is selected as the EC [74]. A bidirectional DC power supply is used to supply the DC link of this inverter. For protection and easy isolation, the EC is not connected to the grid directly, but to a grid emulator of 5kW at 208 V through a 2.5 mH inductor. This grid emulator is able to sink and source power into the EC. The ITECH bi-directional DC power supply maintains a constant 500 VDC to the grid emulator input. OP4510 real-time simulator is selected for implementation of the motor model and the current controller.

Fig 4.3 shows the experimental setup for testing the physical squirrel cage IM of 5-hp, 4-pole, and 16A. The standard blocked-rotor, direct-current test and no-load tests were employed to obtain the parameters of the machines [75]. The measured stator self-reactance, rotor self-reactance, magnetizing reactance, stator resistance, and rotor resistance are as follows: 1.8990 Ω , 4.4164 Ω , 76.5378 Ω , 0.9649 Ω , and 1.3046 Ω respectively. A DC machine is coupled with the IM for loaded tests. This test bench is used to generate results from the physical machine for validating the ones obtained from the emulator system. In this section, the experimental results are

presented to confirm the presence of Dead time (DT) in the EC under both load and no-load conditions [76]. For the tests that are conducted in these subsystems, the DC bus voltage for the EC is set to 300 V, the applied voltage to the motor is 35 V, and the inverter dead-time is 1 μ s.

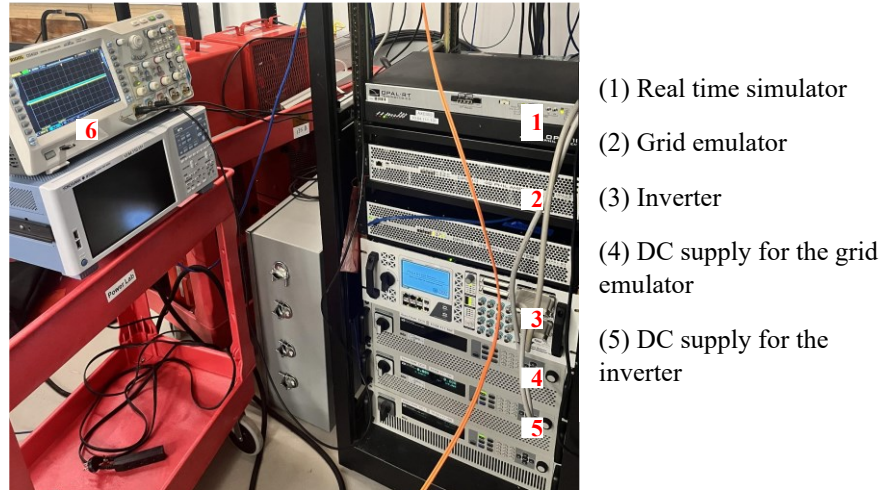


Fig 4. 2 Experimental setup of the proposed IM emulator system



Fig 4. 3 Experimental setup for the physical IM

Fig 4.4 shows the harmonic analysis of the phase A emulated current for the conventional PI controller method compared to the physical motor under no-load and load conditions. This analysis reveals that the emulated current contains 5th and 7th harmonics, which require compensation.

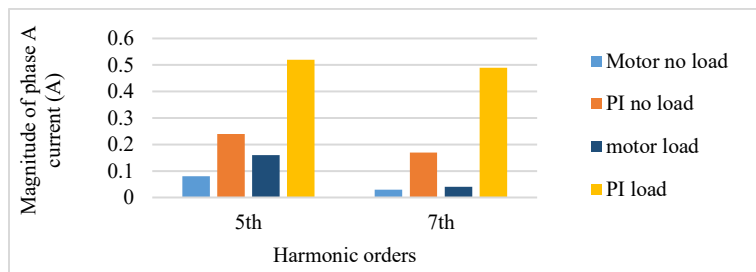


Fig 4. 4 5th and 7th harmonic comparison between the PI method, and physical machine

4.2. Harmonic on motor emulator

4.2.1. The main harmonic component in the motor emulation system

As discussed earlier, the main objective of the motor emulator system is to control the EC and ensure that it mimics the behavior of the motor. In the ideal situation, the dynamic relationship of the EC can be expressed as

$$V_{conv}(t) = R_f i_{abc_emu}(t) + L_f \frac{di_{abc_emu}(t)}{dt} + V_{abc_grid}(t) \quad (4-1)$$

V_{conv} is the output voltage of the EC, and V_{abc_grid} is the grid voltage as the IM is directly connected to the grid. L_f and R_f are the coupling inductance and inner resistance of the interface element, respectively. However, practically (4-1) needs to be modified to consider the inverter nonlinearity. This is mainly because of the use of a two-level PWM-based VSI as the EC. For the safe operation of these switch-based inverters, a blank time or DT must be inserted between the two switching devices in the same leg to prevent short circuits by ensuring that both IGBTs in a phase are not turned on simultaneously. This small delay between the switching of opposite IGBTs is necessary to avoid creating a direct short circuit path, which could lead to significant damage to the inverter and the associated components. However, while dead time is critical for the safe operation of the inverter, it also introduces challenges, particularly in terms of harmonic generation. During the dead time, when neither switch is fully conducting, the voltage or current transition is not ideal, leading to distortions in the output waveforms. These distortions generate higher-frequency components, or harmonics, which are primarily at the switching frequency and its multiples. Furthermore, dead time can cause asymmetry between the three-phase voltages, leading to cross-over distortions and imbalances that contribute to the harmonic content. Moreover, This DT degrades the control performance and accuracy of the motor emulator system by deteriorating the output voltage, causing fundamental voltage drop, and harmonic currents [76]-[78]. Thus, considering the distorted voltage terms, (4-1) can be represented as follows:

$$V_{conv}(t) + \Delta V_{conv} = R_f i_{abc_emu}(t) + L_f \frac{di_{abc_emu}(t)}{dt} + V_{abc_grid}(t) + \Delta V_{abc_grid} \quad (4-2)$$

ΔV_{conv} is the average distorted voltage in the emulation converter and ΔV_{abc_grid} is the grid distorted voltage. In this study, the grid is considered to be ideal, so the term ΔV_{abc_grid} is neglected. The per-phase circuit diagram is shown in Fig 4.5 (a). The motor emulator operates in

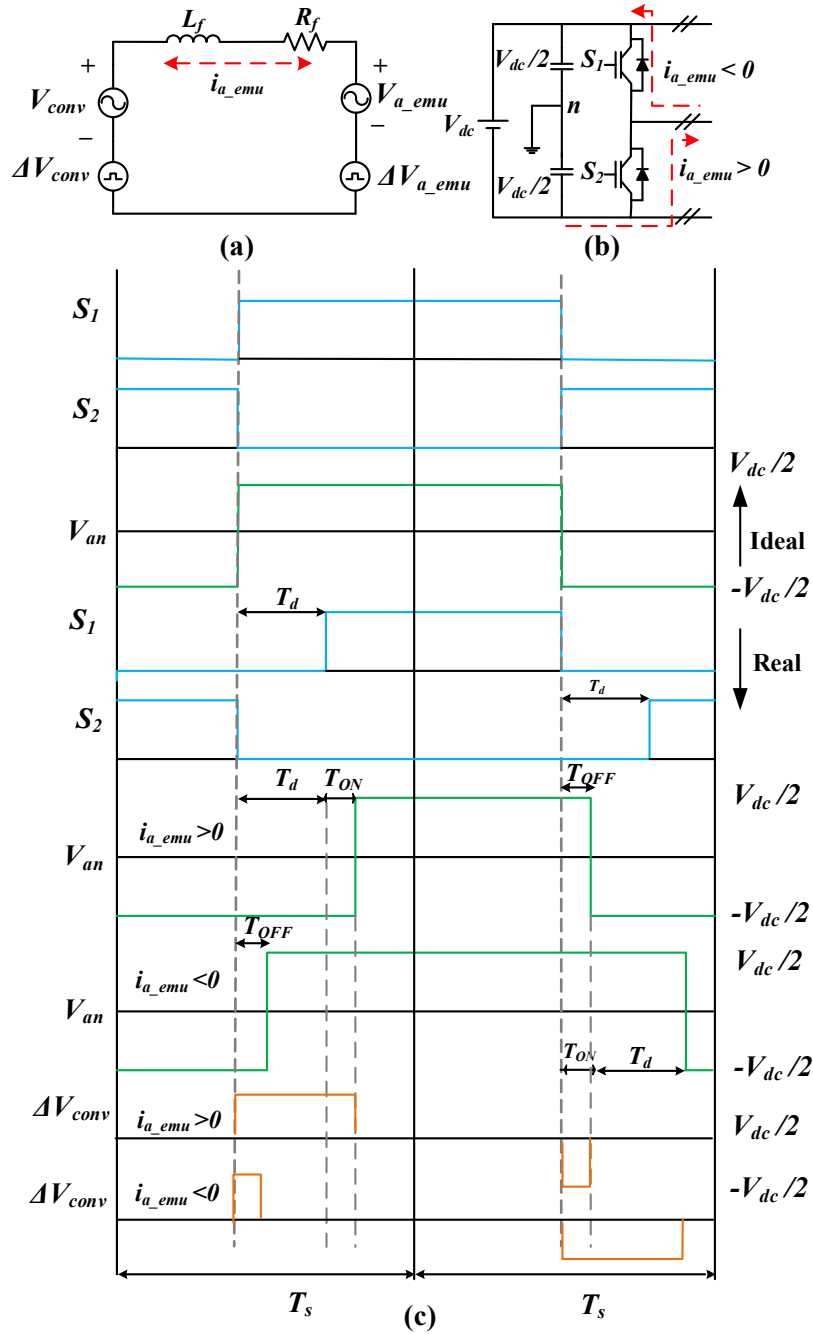


Fig 4. 5 (a) Per-phase equivalent circuit of the emulation system. (b) The basic configuration of one phase leg of the emulator converter. (c) Switching pattern of the switching devices considering the ideal and actual conditions.

the motoring mode, with the current flowing from V_{abc_grid} to V_{conv} . Fig 4.5 (b) shows one phase leg of the three-phase voltage inverter which is commonly used in EC. During the dead time (T_d), both S_1 and S_2 are not conducting. Because of the inductive load, the i_{a_emu} is continuous, this

current flows through the lower freewheeling diodes when the current is positive, and the negative dc voltage is connected to the output. If the current is negative, flowing toward the inverter, the positive voltage is output through the upper diode as a result. Therefore, the output voltage is distorted and the output distorted voltage depends on the direction of the current i_{a_emu} . [80]-[82].

The ideal gating pulses pattern is shown in Fig.4-5(c). Moreover, Fig.4.5(c) presents a dead time (T_d) delay in which both switches in the same leg are not conducting. The time delay associated with turning ON (T_{ON}) and OFF (T_{OFF}) of the device is indicated in the same figure. These time delays present the time taking by the switch to become effectively ON/OFF. The resulting phase to center voltage (V_{an}) considering dead time and ON/OFF delay is illustrated in Fig.4-5(c).

The average EC distorted voltage (ΔV_{conv}), which depends on the current direction, can be represented as

$$\Delta V_{emu} = \frac{-T_d - T_{ON} + T_{OFF}}{2T_s} V_{dc} \text{sign}(i_{a_emu}) \quad (4-3)$$

where T_d , T_{ON} , T_{OFF} , T_s , i_{a_emu} , and V_{dc} represent the DT, turn-on time delay, turn-off time delay, switching period, phase a current, and dc-link voltage, respectively. The harmonic content of the EC output voltage introduces harmonic components to the emulated motor current. The error is analyzed using the Fourier series [83]. The distorted current in the synchronous reference frame contains 6th harmonics ($n=1,2,\dots$) due to the EC dead time. The DT effect can be reduced by applying an appropriate DT compensation method.

4.2.2. Motor emulator controller design

The main design criterion for the current controller of the emulator converter is to have the highest bandwidth possible. The voltage equations for the d and q axis, including the coupling inductance, feedforward terms, and cross-coupling terms, can be written as below:

$$V_{conv_d} = R_f I_{emu_d} + L_f \frac{dI_{emu_d}}{dt} - \omega L_f I_{emu_q} - V_{grid_d} \quad (4-4)$$

$$V_{conv_q} = R_f I_{emu_q} + L_f \frac{dI_{emu_q}}{dt} - \omega L_f I_{emu_d} - V_{grid_q} \quad (4-5)$$

The block diagram of the current controller is shown in Fig.3. The open loop transfer function of the emulator system current loop can be derived as

$$G_{OL}(s) = \frac{1}{L_f s + R_f} e^{-sT_s} e^{-sT_d} G \frac{K_I(1 + s\tau_{PI})}{s} \quad (4-6)$$

where the inverter is modeled as a first-order transfer function in which G is the inverter gain. The value of G is selected equal to half of the inverter dc bus voltage. Also, T_d denotes a time delay corresponding to half of the switching period. The current sensors in the system are treated as first-order transfer functions with a time delay of T_f . The sampling time of the digital controller is T_s . (4-6) includes the coupling filter transfer function with L_f and R_f components. The time constant of the interface filter is comparatively larger than the other poles. Therefore, this is the dominant pole. Adding the PI controller to the system, the zero of the PI controller cancels the pole of the interface filter. The close loop transfer function of the EC current loop considering the pole-zero cancellation is driven in Chapter 3. The bandwidth of the system can be calculated by comparing (3-3) with the standard second-order transfer function. For this study, the G is 150V, T_d is 50 μ s, T_f is 40 μ s, T_s is 20 μ s, R_f is 300 m Ω , L_f is 2.5 mH and ζ is 0.707. The open-loop magnitude and phase plot of the designed current controller are shown in Fig 4.6. The designed current controller, with a bandwidth of 1 kHz, ensures stability by maintaining a positive gain margin.

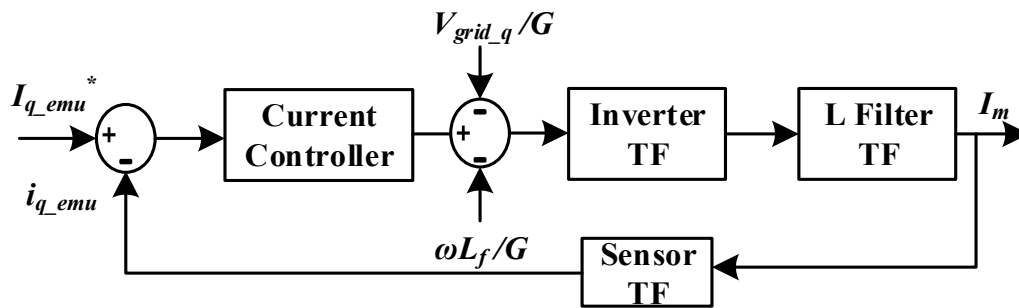


Fig 4. 6 The emulator converter current controller block diagram

4.3. Harmonic compensation for motor emulator

4.3.1. PI and PR -based dead time compensation

As mentioned previously, the DT on EC affects the harmonic content and total harmonic distortion (THD) of the VSI output voltage, thereby impacting system stability and the lifespan of devices [84]. To overcome the harmonics produced by the dead-time effect, different methods have

been proposed in the literature. In [85], [87] each harmonic is accurately computed by analyzing its cause, yet it requires intensive mathematical calculation. In [78], average voltage and losses are computed across the switching cycle and then used to adjust reference voltages according to the current direction. However, this method loses effectiveness, especially at low output current and frequency, due to its reliance on current direction and average voltage estimation. In [86], the DT is compensated by the gate driver signal in the VSI. However, this method requires external hardware. This work proposed a compensation method using a resonant controller. This method doesn't need offline experiments, extra hardware, or complex calculations.

In the presence of DT in the EC, as discussed in the previous section, the dq -axis current contains 6th order harmonic. The designed PI controller for the EC has zero steady-state error for the DC components only. Therefore, the control structure of the emulator system needs to be modified to achieve zero steady-state error at harmonic frequencies other than DC. The proportional resonant (PR) controller is a double integrator that introduces infinite gain at a selected frequency (resonance frequency). Thus, the PR controller eliminates the steady-state error at that frequency with no attenuation outside this frequency and no phase shift at other frequencies [88],[89]. Fig 4.7 presents the proposed DT compensation method using the PR controller. The PI controller works in tandem with the PR controller to achieve zero steady-state error. The proposed controller transfer function (4-7) and the open loop transfer function of the proposed controller for the motor emulator current loop (4-8) can be represented by:

$$G(s)_{PR+PI} = \frac{Ak\omega_6 s}{s^2 + k\omega_6 s + \omega_6^2} + \frac{K_I(1 + s\tau_{PI})}{s} \quad (4-7)$$

$$G_{emu}(s) = G(s)_{PR+PI} \frac{1}{L_f s + R_f} e^{-sT_s} e^{-sT_d} G \quad (4-8)$$

$$\frac{K_{PI}(1 + s\tau_{PI})}{s}$$

where k is the damping factor, A is PR controller gain, and ω_6 is the resonance frequency for the PR controller. The PR controller gain (A). The implementation of the proposed controller is shown in Fig 4.7 (b). The open loop transfer function obtained for the emulator system is shown in (4-8). The open loop phase and magnitude plots for the proposed DT compensation method are compared with the conventional PI controller in Fig 4.8. Fig 4.8 shows that the proposed controller adds around a 20 dB gain at the selected frequency. Thus, the additional resonant peak modifies the

4.3.2. ANN-based harmonics compensation

Considering that the PR controller is developed specifically to alleviate a targeted harmonic component, the design and implementation of multiple PR controllers to address additional frequencies of interest is not feasible because the tuning process of multiple PR controllers necessitates an exhaustive and precise adjustment of parameters for both the proportional and resonant components to achieve the desired response. Thus, an ANN-based control strategy with interpolation capability is introduced in this section for mitigating the harmonics in the motor emulation system. The enhanced harmonic performance and efficiency achieved through the implementation of ANNs have unequivocally demonstrated their effective role in addressing power system challenges, including power converter control, fault detection, modeling, estimation, and forecasting [90]. The Multilayer Perceptron (MLP), recognized as the most commonly employed Artificial ANN in power electronic-based designs, is chosen for its simple structure, flexibility in expanding inputs/outputs, and robustness in handling unforeseen circumstances [91]. Consequently, this research work also uses MLP to design a model-free, robust control loop for the proposed motor emulation system. The designed MLP Controller (MLPC) receives the current tracking errors of the d-axis (I_d) and q-axis (I_q) as inputs and then generates the desired dq reference signals for generating the gating pulses. The MLPC structure, including input, hidden, and output layers, is illustrated in Fig 4.9. In addressing the control problem, the hidden and output layers are configured with 16 and 2 neurons, respectively. Thus, 62 weighting factors and 18 biases are assigned among the neurons to propagate the input signals throughout the neural network.

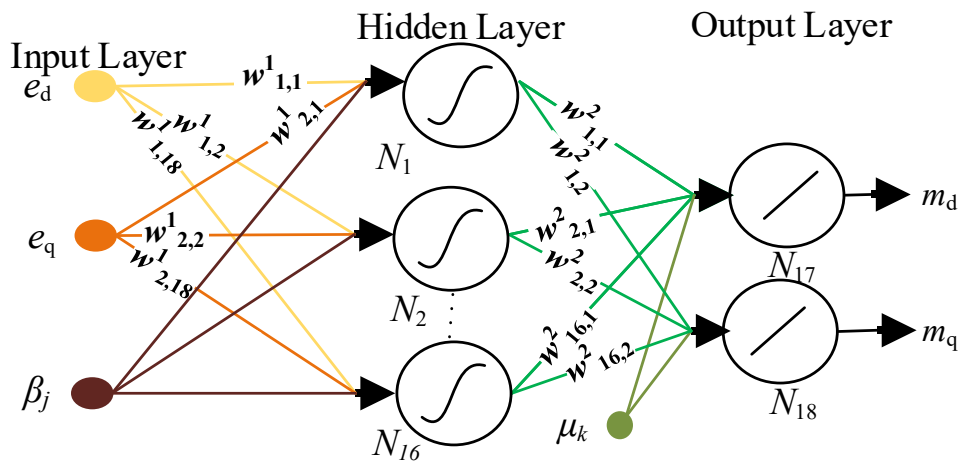


Fig 4. 9 Neural network configuration for the proposed MLPC

The activation functions ($f_j(\psi)$) in the hidden layer use a sigmoidal form, while linear functions are employed for the output neurons to simplify the process.

$$f_j(\psi) = \frac{1}{1 + e^{-\psi}} \quad (4-9)$$

$\psi_i = [e_d \ e_q]$ is the input vector of the neural network. Since the weighting factors and biases placed among the neurons determine the neural network behavior, they must be properly trained to attain the desired performance expected from MLPC. In this regard, the mathematical model of the MLPC is first extracted as below:

$$\left\{ \begin{array}{l} m_d = \mu_k + \sum_i^2 \sum_j^{16} w_{kj} w_{ij} f_j(\psi_i) + \beta_j \Big|_{k=1} \\ m_q = \mu_k + \sum_i^2 \sum_j^{16} w_{kj} w_{ij} f_j(\psi_i) + \beta_j \Big|_{k=2} \end{array} \right. \quad (4-10)$$

$$\left\{ \begin{array}{l} m_d = \mu_k + \sum_i^2 \sum_j^{16} w_{kj} w_{ij} f_j(\psi_i) + \beta_j \Big|_{k=1} \\ m_q = \mu_k + \sum_i^2 \sum_j^{16} w_{kj} w_{ij} f_j(\psi_i) + \beta_j \Big|_{k=2} \end{array} \right. \quad (4-11)$$

m_d , m_q , μ_k , and β_j are respectively the k th output of the MLPC, the bias of the k th output neuron, and the j th hidden neuron. w_{ij} and w_{kj} are the j th weighting factors from the i th input to the j th neuron in the hidden layer and the k th neuron in the output layer, respectively. Secondly, Levenberg–Marquardt (LM) as an effective supervised training strategy is considered to train the MLPC network using training data obtained from the PR-based controller shown in Fig 4.10. LM, a classical optimization algorithm, combines the advantages of Gradient Descent and Newton-Gauss techniques to train ANNs with high accuracy in minimum time [90]. The LM algorithm offers significant advantages over both Gradient Descent and the Newton-Gauss methods, particularly in training ANNs. While Gradient Descent is simple and computationally efficient, it can converge slowly. On the other hand, the Newton-Gauss method provides faster convergence by approximating the second-order derivatives of the error function, but it can be computationally expensive and sensitive to the choice of the initial starting point, potentially leading to instability or slow convergence when the error surface is poorly conditioned. LM combines the strengths of both approaches by dynamically adjusting between Gradient Descent and Newton-Gauss, allowing it to maintain stability (like Gradient Descent) while still benefiting from the faster convergence rate of Newton-Gauss. This combination ensures that LM can train networks with high accuracy in a shorter amount of time, making it an ideal choice for problems requiring efficient and precise optimization.

As the first step of the training process, the Mean Squared Error (MSE) is formalized in (4-12) to measure the training errors between the reference data and MLPC outputs. As the first step of the training process, the Mean Squared Error (MSE), as the objective function of the training algorithm is formalized in (4-12) to measure the training errors between the reference data and MLPC outputs.

$$\xi = \left[\begin{array}{c} \frac{1}{n} \sum_{l=1}^n (m_l^d - m_l^{d*})^2 \\ \frac{1}{n} \sum_{l=1}^n (m_l^q - m_l^{q*})^2 \end{array} \right] \quad (4-12)$$

Where m_l^d , m_l^q , m_l^{d*} , and m_l^{q*} are the l th sample data generated by MLPC and the reference PI-PR controller for the d-axis and q-axis, respectively. n is the total number of data points.

Table I presents the training parameters and the MLPC parameters. λ in Table I is the convergence speed of the LM algorithm.

Table 4. 1 Training parameters

No.of Iteration	No.of weights	No.of Biases	λ	$\omega_{m,q}^n$
1000	64	18	0.001	[-50 50]

The training loop is presented in Fig 4.10. As shown, the control performance of the reference controller (the PI-PR control loop) is compared with the MLPC during each iteration to calculate the training error; then the LM algorithm is used to minimize the training error in a way the MLPC controller learns how to minimize the harmonics besides tracking i_d^* and i_q^* . The training begins with a random initialization of weighting factors and biases within predefined boundaries presented in Table 4.1. These boundaries influence both the training time and accuracy. Overly wide boundaries may result in a local optimum solution or extended training times, while overly tight boundaries could prevent convergence. Despite these challenges, data from the cost function helps to monitor training performance to reduce training efforts.

Regarding, the regression analysis in Fig 4.11 demonstrates the satisfactory training of the MLPC after 768 epochs. According to Fig 4.11, the ANN meets a satisfactory level of regressing for the training, validation, and test data.

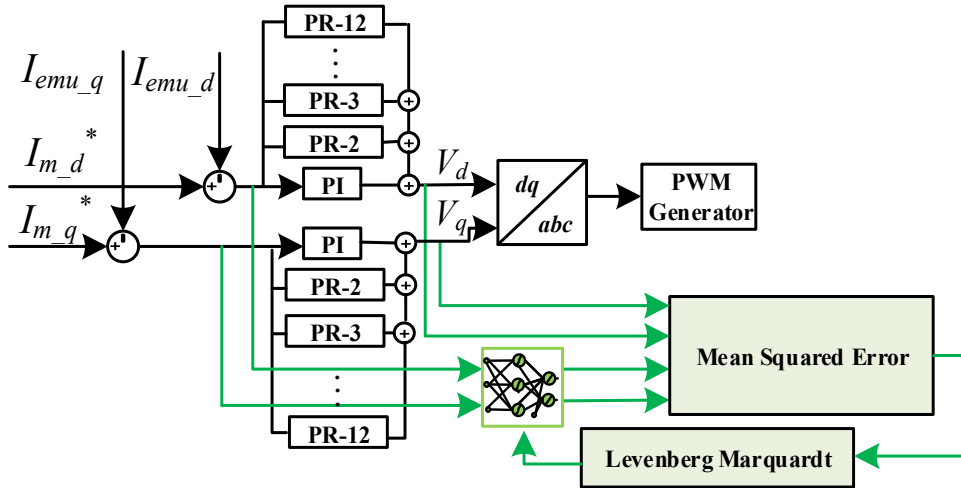


Fig 4. 10 MLPC training loop including the RCD-based controller, the Levenberg-Marquardt optimization algorithm, the mean squared error cost function, and the neural network

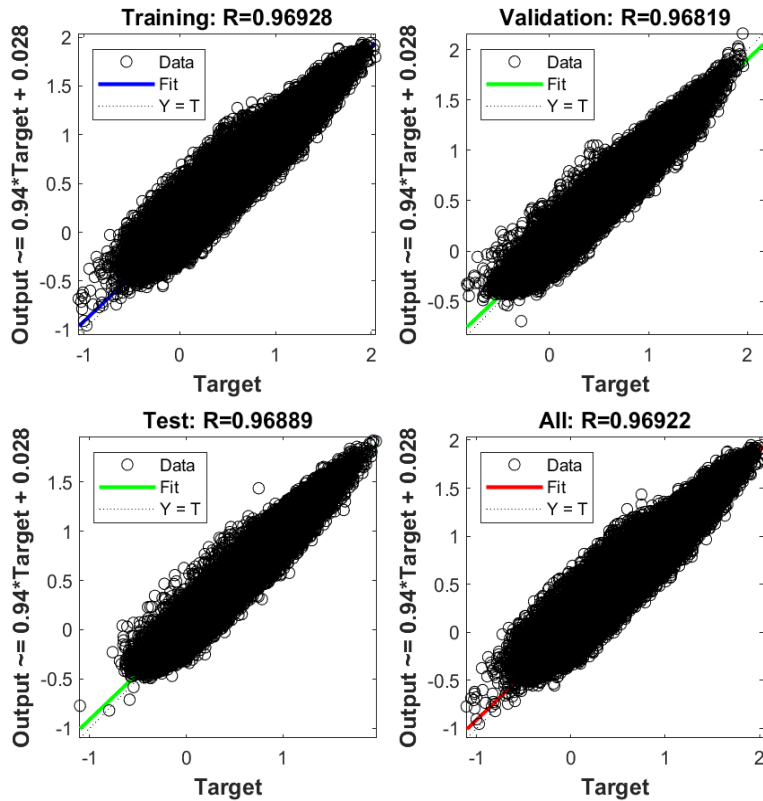


Fig 4. 11 Regression analysis for training, validation, and testing data

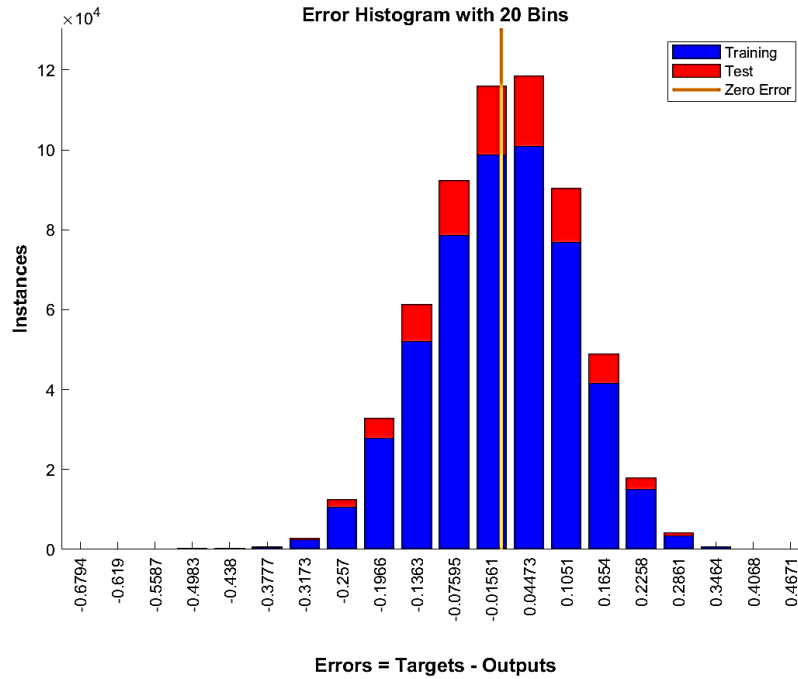
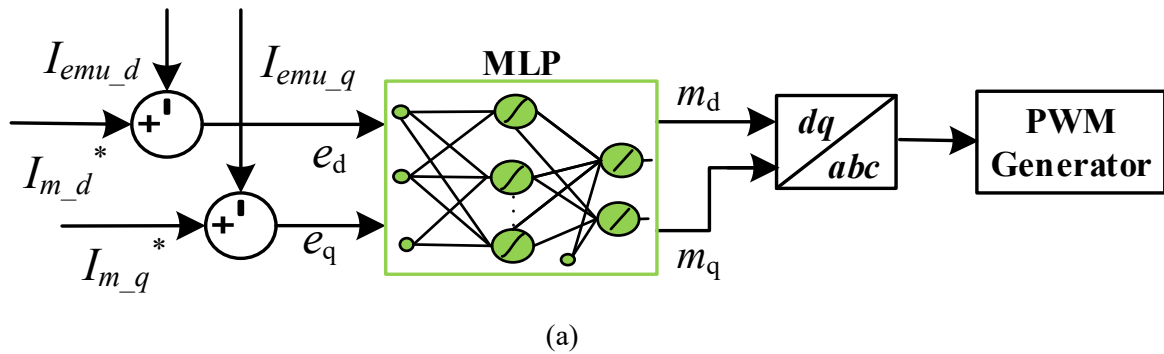


Fig 4. 12 Histogram analysis of the training and testing errors

The histogram analysis of training and testing errors in Fig 4.12 further indicates satisfactory performance, as most errors cluster near the minimal value.

As shown in Fig 4.13, the trained MLPC is independently used in the control loop, as the proposed intelligent harmonic compensation technique. A comparison between Fig 4.7 and Fig 4.13 reveals that the proposed MLPC replaces the whole PI-PR controller with a single ANN unit. The input and output of this unit are presented in the same figure (Fig. 4.13(b)).



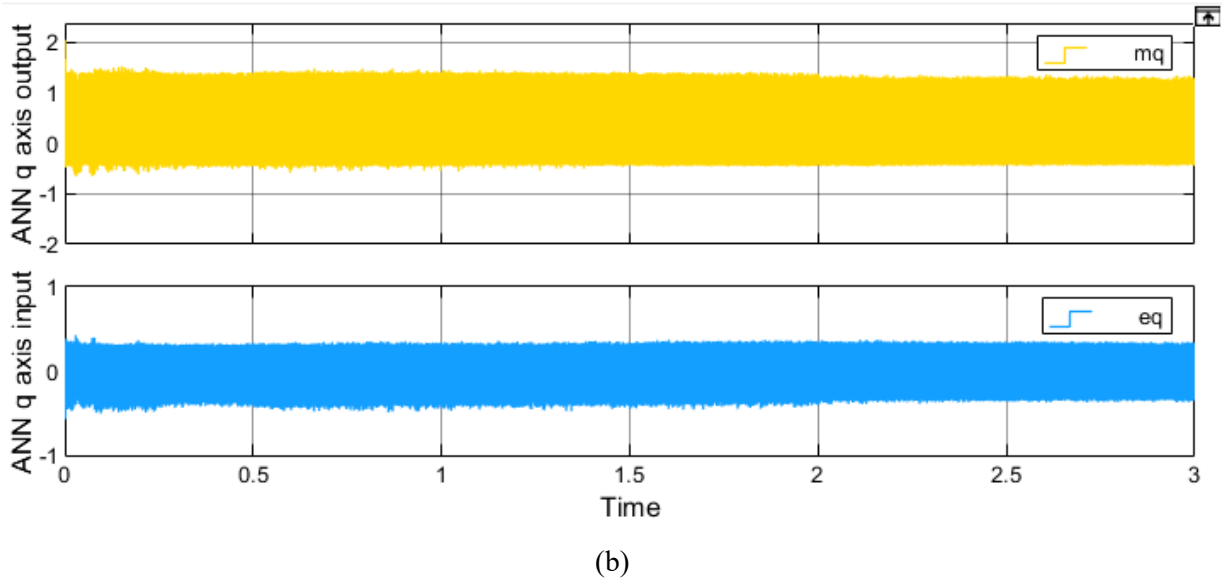


Fig 4. 13 (a) Diagram of the proposed ANN-based controller for IM emulation (b) the measured input and output of ANN

4.4. Experimental results

In this section, the experimental results are presented to confirm the effectiveness of both the emulator controller and the proposed modifications made to the emulator control structure for compensating DT and other harmonic components in the EC under various operating conditions. The same experimental setup and conditions described in section 4.1 are utilized.

4.4.1. Computational time

The computational time for different control methods is given in Table 4.2. Based on the results, the computational time of the ANN control has only increased by 2.6% in comparison to the PI method.

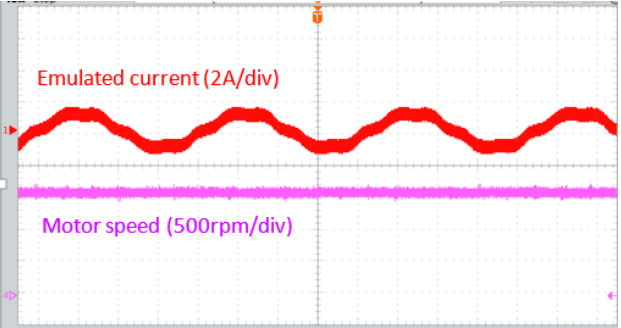
Table 4. 2. Execution time for different control methods

PI control method	PI and PR control method	ANN control
5.65 μ s	5.66 μ s	5.80 μ s

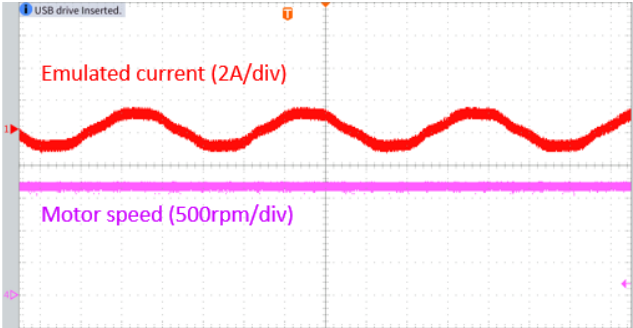
4.4.2. Steady state results on no-load and load condition

The obtained results from the PI-based emulation system are shown in Fig 4.14 (a). It includes the emulated phase-A current and the motor speed generated by the motor model. Fig

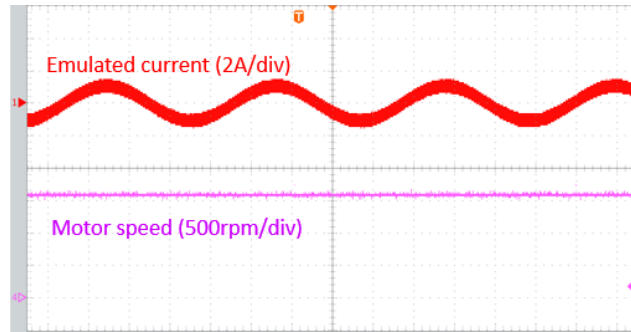
4.14 (b) illustrates the same results obtained from the PI-PR-based IM emulation system. A noticeable reduction in harmonic components can be observed in the PI-PR-based method as compared to the PI-based method. Fig 4.14 (c), shows the same experimental results obtained from the ANN-based IM emulator system in the steady state condition. It can be observed that the results obtained from the MLPC-based method have lower harmonics compared to both the PI-PR-based and PI- based methods. Fig 4.14 (d) presents experimental results for the direct online startup test of the actual IM, depicting the phase A stator current, and speed under steady-state condition. It is evident that results in Fig. 4.14 (a)-(c) through the IM emulation closely match those of the actual motor in steady state condition, especially the fundamental current components.



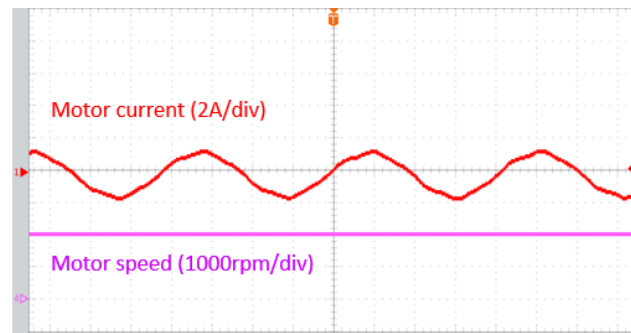
(a)



(b)



(c)



(d)

Fig 4. 14 Experimental results obtained for steady state condition (a) PI based method (b) PI and PR method (c) ANN method (d) prototype IM (Time scale:4 ms/div)

Fig 4.15 presents steady-state results obtained for the dq axis emulated currents using these three control methods. It can be observed that applying the proposed ANN controller yields better performance compared to both PI-based method and the PI-PR-based method in terms of reducing the harmonic current components.

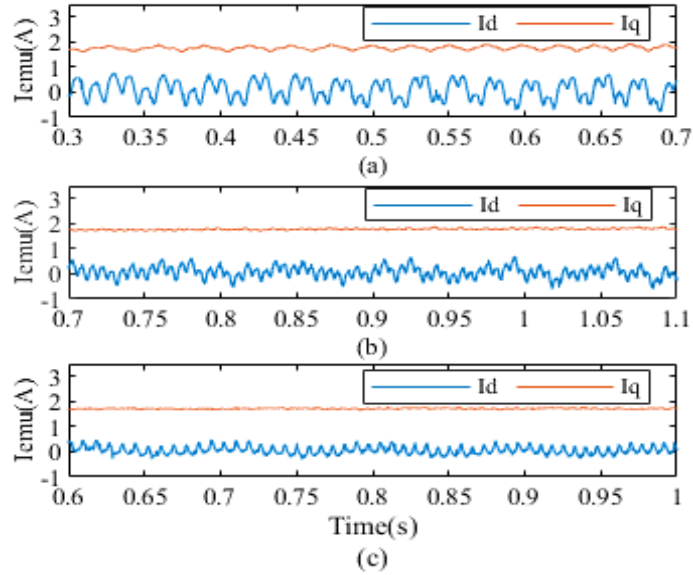
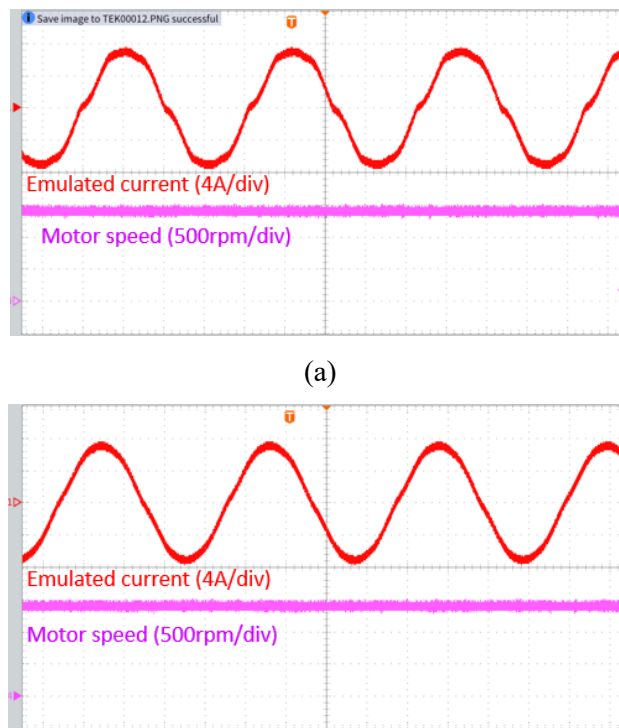


Fig 4. 15 Experimental results measured dq axis emulated current (a) PI-based method (b) PI-PR-based method (c) ANN-based method

Fig 4.16 shows the obtained results when load torque has been applied to the IM machine. Fig 4.16 (d) shows the measured results of the actual machine in the steady state, while Fig 4.16 (a), (b), and (c) show the corresponding emulation results. It can be seen that the emulated currents are nearly the same as the actual current results under this loaded condition.



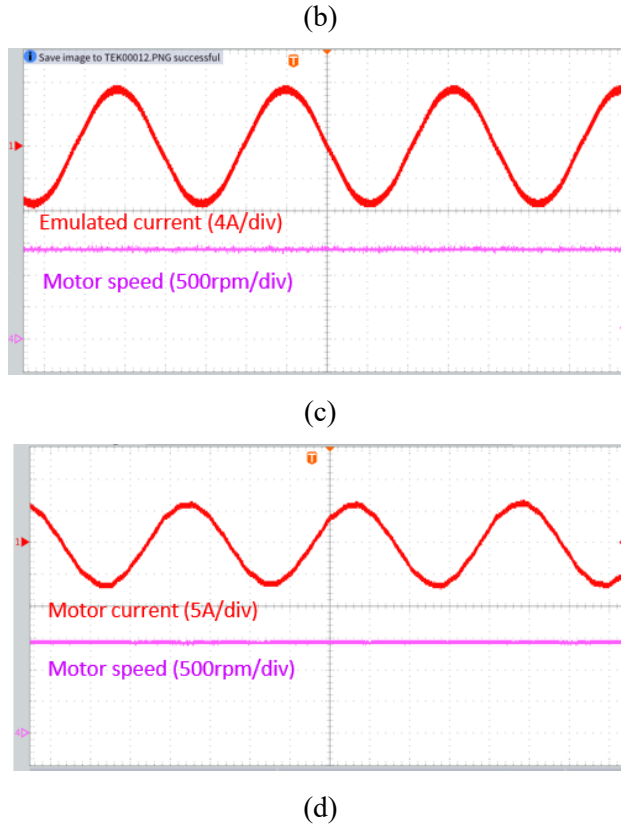
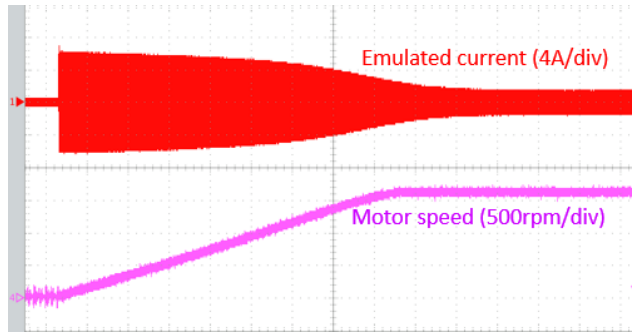


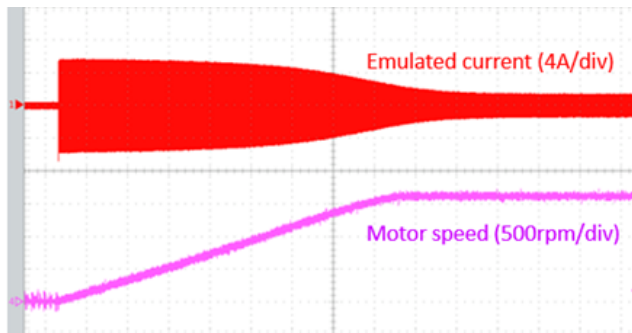
Fig 4. 16 Comparison of the measured phase A current and speed in load condition (a) PI-based (b) PI-PR-based (c) ANN-based (d) Physical machine (Time scale:4 ms/div)

4.4.3. Transient results

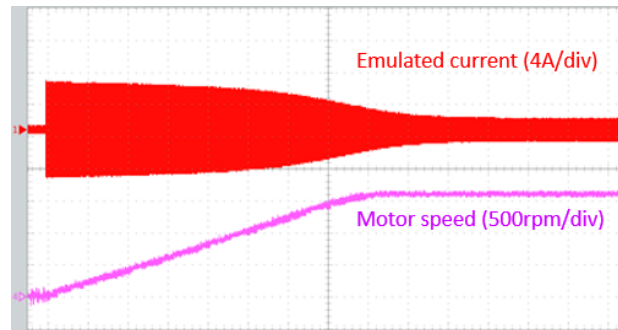
Fig 4.17 presents the results of the online startup of the IM emulation system employing PI-based, PI-PR-based, and ANN-based control, respectively. The emulated phase A current and motor speed generated by the motor model are measured for each of these control methods. Additionally, Fig 4.17 displays the results of the actual motor during direct online startup, measuring the motor phase-A stator current and speed. The IM emulation results are observed to closely align with the physical motor results, achieving similar steady-state conditions within comparable timeframes. These outcomes demonstrate a strong agreement between the test results from the virtual machine and the physical machine.



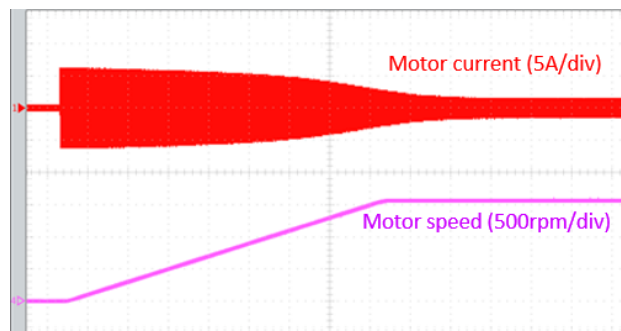
(a)



(b)

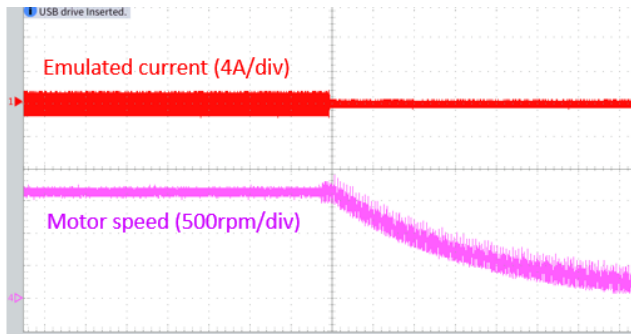


(c)

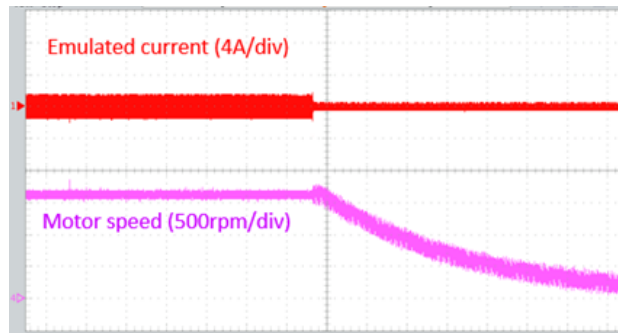


(d)

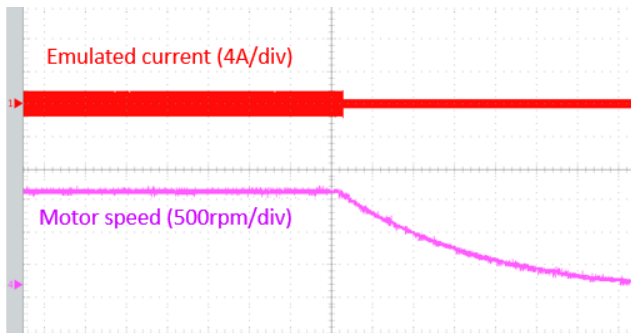
Fig 4. 17 Experiment results during startup, (a) PI-based (b) PI-PR-based (c) ANN-based (d) Physical machine (Time scale:500 ms/div)



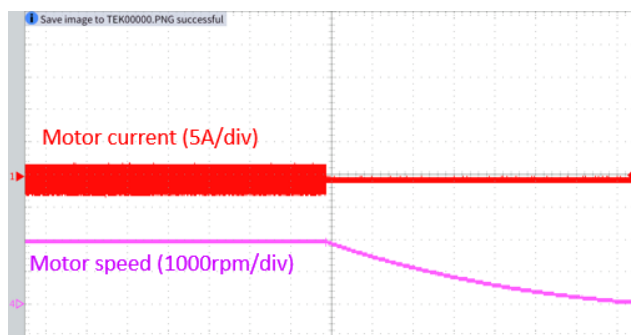
(a)



(b)



(c)



(d)

Fig 4. 18 Experimental results obtained for run down (a) PI based method (b) PI and PR method (c) ANN method (d) prototype IM (Time scale:4 s/div)

The measured rundown results of phase A current and motor speed for (a) PI-based IM emulation, (b) PI-PR-based IM emulation, (c) ANN-based IM emulation, and (d) direct testing with the physical machine are presented in Fig 4.18. These results clearly demonstrate a close match between the prototype machine and the machine emulator system, confirming its accuracy.

Fig 4.19 shows the measured results of phase A current and motor speed during a sudden load increase for (a) PI-based IM emulation, (b) PI-PR-based IM emulation, (c) ANN-based IM emulation, and (d) direct testing with the physical machine. These results demonstrate the effectiveness of the compensation method during transient behavior.

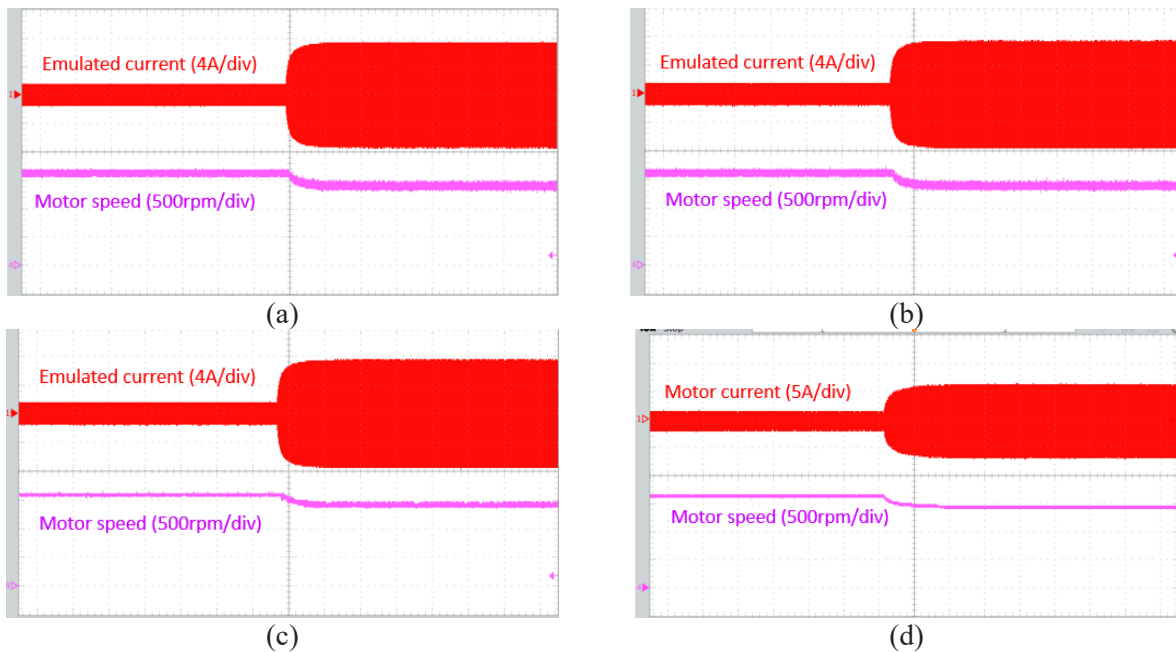


Fig 4. 19 Experimental results obtained for sudden load increase (a) PI based method (b) PI and PR method (c) ANN method (d) prototype IM (Time scale:4 s/div)

Fig 4.20 presents the measured phase A current and motor speed results during a sudden reduction in load for (a) PI-based IM emulation, (b) PI-PR-based IM emulation, (c) ANN-based IM emulation, and (d) direct testing with the physical machine. A close match between the physical motor results and the emulation system results under various transient conditions demonstrates the proposed system's capability to emulate motor transient.

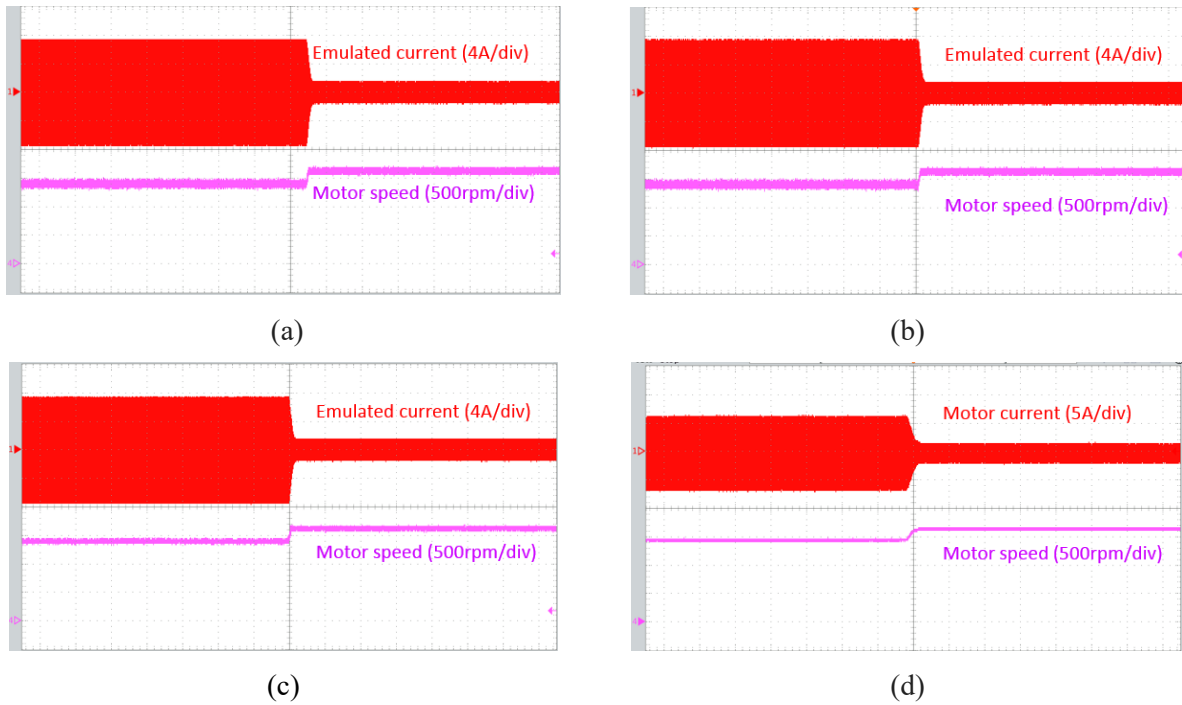


Fig 4. 20 Experimental results obtained for sudden load reduction (a) PI based method (b) PI and PR method (c) ANN method (d) prototype IM (Time scale:4 s/div)

4.4.4. Harmonic analysis results

This section evaluates motor emulation accuracy using these three different control methodologies. The factor indicating emulator performance is the THD in the emulated phase currents. The primary goal of motor emulation is to replicate the behavior of the motor. Nonetheless, various control or switching harmonics may be introduced into the motor emulation system. Table 4.3 compares THD magnitudes in phase currents under no-load and loaded conditions. The THD percentage of the PI-based configuration is higher compared to the PI-PR-based emulator systems. Additionally, the ANN-based compensation method shows a THD value very close to that of the physical motor. These results confirm that using an ANN-based emulator compensation method can enhance motor emulation accuracy and utility.

Table 4. 3 Comparative THD% analysis of phase A emulated current and motor

Control method	Magnitude of THD percentage for phase A current in no load condition	Magnitude of THD percentage for phase A current in load condition
Motor	5.35%	2.77%
PI	13.58%	12.56%
PI and PR	7.62%	6.11%
ANN	5.51%	5.35%

Table 4. 4 compares the harmonic analysis of motor current across three control strategies, both under no-load and loaded conditions. The absolute error between each control method and the physical motor has been calculated. The PI-based method outperforms others in the 5th and 7th harmonics. Thus, employing these compensation methods can mitigate harmonics to some extent.

Table 4. 4 Comparative 5th and 7th harmonic analysis of phase A emulated current and motor

Control method	Harmonic order	Phase A harmonic magnitude (A) no load condition		Phase A harmonic magnitude (A) load condition	
		Magnitude	Error	Magnitude	Error
Physical motor	5 th	0.08	-	0.15	-
	7 th	0.02	-	0.04	-
PI	5 th	0.24	0.16	0.52	0.36
	7 th	0.17	0.14	0.49	0.46
PI and PR	5 th	0.02	0.06	0.05	0.1
	7 th	0.02	0	0.05	0.01
ANN	5 th	0.03	0.05	0.08	0.07
	7 th	0.03	0.01	0.07	0.03

4.5. Summary

PHIL-based motor emulations are gaining popularity in testing electric drive systems due to several advantages. This work investigates and compensates for the harmonics in the emulator converter. Initially, the emulator current control scheme is modified to compensate for the effect of DT in the EC, aiming to increase the accuracy of the motor emulator system. Moreover, an ANN-based intelligent control strategy is introduced to compensate not only for the DT effect but also for the other lower-order harmonics in EC. This ANN-based intelligent control strategy

enhances the THD% of the emulator system. Experimental results are presented to validate the proposed emulator's current controller and the proposed emulator control strategies. The results obtained from the emulator system are compared with those from a physical motor operating under the same conditions. A close match between the results serves as evidence, demonstrating the effectiveness of the proposed control strategy in ensuring the safe operation of the emulator system. Additionally, the proposed PI-PR-based and ANN-based control reduce the harmonics imposed by the inverter nonlinearity.

Chapter 5 PHIL based induction motor emulator with LC filter

Emulating an electric machine allows for testing the drive inverter and controller of an electric drive system prior to prototyping. This chapter focuses on emulating an induction machine (IM). The IM emulator system proposed in this chapter consists of the IM drive with an LC filter. This configuration enables the smooth pulse width modulation (PWM) output voltages of the motor drives. Moreover, employing high-performance, high-bandwidth class D power amplifiers as emulator converters enhances the system's bandwidth, thereby ensuring accurate machine emulation. The work presents a detailed description of the proposed machine emulator system and the design of the drive with LC filter. Experimental results demonstrate the effectiveness of the proposed IM emulator system in replicating various machine transient behaviors. Furthermore, a comparison between the experimental results obtained from the emulator and those from a prototype IM drive is conducted to verify the accuracy of the emulation.

5.1. System description of IM emulator

Fig 5.1 depicts a schematic of the proposed PHIL-based machine emulator. The proposed machine emulator system includes the machine emulator, drive inverter, and RTS, along with a block diagram of the control circuit. The coupling inductor (L_e) connects the machine emulator to the drive inverter with the LC filter. Additionally, both the drive inverter and the machine emulator (power amplifier) are linked to the bidirectional power supply.

The machine emulator utilizes a high-performance four-quadrant power amplifier to act as an induction motor. The primary objective of the power amplifier is to draw current from the drive inverter as an IM. To accomplish this, the output voltages of the LC filter (V_{out_LC}) are measured and converted to the dq reference frame (V_d and V_q). These voltages are then fed into the mathematical model of the induction machine, which generates reference currents (I_{dm} and I_{qm}) for the emulator current controller. These reference currents are compared with the actual measured LC filter output current (I_{emu}). The error between the machine stator currents and the LC filter current is fed into the proportional-integral (PI) controller. The PI controller generates a voltage reference (V_{ref}) for the power amplifier based on this error signal. Consequently, the power amplifier ensures that the induction motor's stator current closely tracks the emulated current (I_{emu}). This process allows the power amplifier to accurately replicate the behavior of an induction motor drive integrated with an LC filter.

To simplify the proposed emulation system, L filter (L_e) is introduced between the drive inverter and the emulator. Selecting the coupling element is crucial as it affects both the emulation bandwidth and accuracy. A large filter element reduces the emulation bandwidth, while a small filter value results in a large ripple in the emulated current. Therefore, the coupling inductance value is chosen to be close to the machine's mean inductance to ensure that the current ripple in the emulated current waveform resembles that of the physical machine.

An IGBT-based two-level voltage source inverter serves as the drive inverter, connected to the LC filter. The control diagram of the drive inverter is depicted in Fig 5.1. The drive controller's reference signals include speed (ω^*), q axis, and d-axis currents (I_q^* and I_d^*). The speed reference signal is compared with the induction motor speed (ω), and the resulting error signal is passed through the PI regulator. The d-axis and q-axis current references are compared with the actual d-axis and q-axis emulated currents. Subsequently, the PI controllers regulate the d-axis (I_d) and q-axis currents (I_d and I_q), generating voltage references that are then transformed from the dq to the abc reference frame for generating the required gating pulses for the drive inverter. A detailed description of the drive inverter controller and emulator will be discussed in the next section. In the present topology for the emulation of an IM with an LC filter, a power amplifier is utilized as an emulating converter (EC).

Fig 5.1 presents the configuration of utilizing one DC power supply for both the EC and the drive inverter. In this configuration, common-mode or zero-sequence currents are generated between the EC (power amplifier) and the drive inverter. The common-mode current is the sum of the circulating currents between the EC and the drive inverter. Therefore, a PI controller is used as a zero-sequence current controller to mitigate the generated common-mode current between the EC and the drive inverter. The DC-DC converter is used to maintain the DC voltage for the drive inverter. The controller for the DC-DC converter is also implemented in the RTS. The control for the drive inverter and machine emulator system, as well as measurements and gating signals, are transferred to the input/output (I/O) of the analog and digital pins of the real-time simulator. The OP4510 real-time simulator is used in this research work. This simulator has a CPU core and an FPGA core. To achieve a low simulation time step and higher accuracy, the machine emulator control and induction motor mathematical model are implemented in the FPGA core. The CPU core, which leads to a higher computational time step, is used for the implementation of drive inverter control.

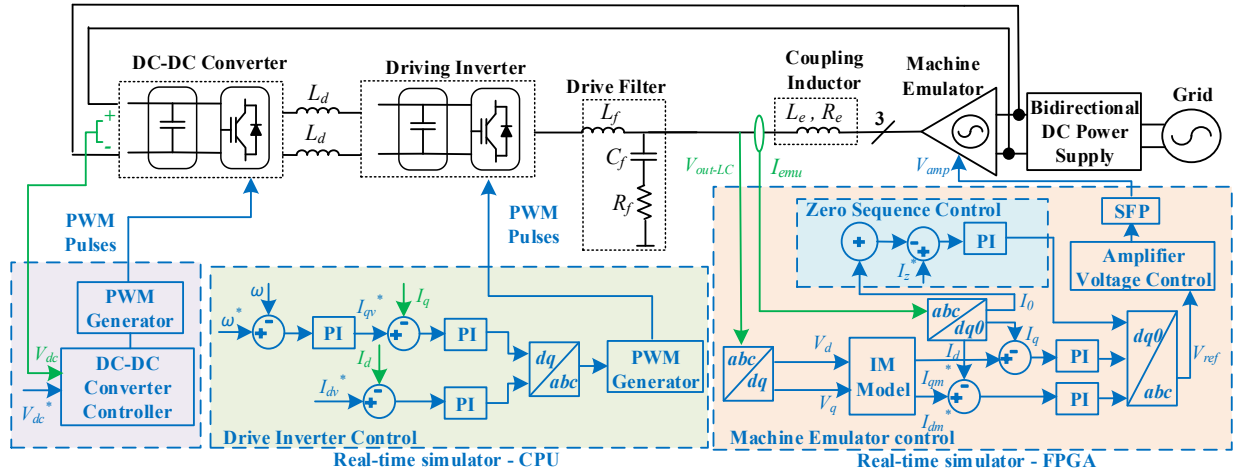


Fig 5. 1 Schematic diagram of the proposed power amplifier-based IM emulator system considering drive with LC filter

5.1.1. Emulator control design

The control proposed methodology for the drive inverter and motor emulation system is shown in Fig 5.1. Both the machine emulator and drive inverter operate in the current control mode. Fig 5.2 illustrates the interaction between the current control loop of the emulator and the drive inverter. The proposed control loop for the emulator system is a cascaded loop configuration, with the emulator loop serving as the inner loop of the drive inverter loop. Therefore, the emulator bandwidth should be high enough to ensure that several machine current harmonics can be precisely emulated. The class D power amplifier utilized in this research work has a bandwidth of 10 kHz. Additionally, the selected Class D power amplifier introduces a time delay, which can be represented as $e^{-sT_{pa}}$, where T_{pa} is 3.3 μ s. To achieve maximum control loop performance, the proposed emulator current control loop is implemented on the FPGA board of the RTS. The associated computational time delay (T_s) for the emulator current control loop is 1 μ s. The transfer function of the coupling inductor represented by the link resistance and link inductance is represented in (5-1) where R_e is 200 m Ω and L_e is 2.5 mH. The PI current controller is designed, where K_i represents the integral gain and K_p represents the proportional gain of the controller. The open-loop transfer function of the emulator current control is given as

$$G_{emu}(s) = \left(\frac{K_I}{s} + K_p\right) \left(\frac{1}{1 + sT_s}\right) \left(\frac{1/R_e}{1 + sL_e/R_e}\right) \left(\frac{1}{1 + sT_{pa}}\right) \quad (5-1)$$

The primary objective of the emulator current control is to achieve the highest possible bandwidth. The Bode plot of the emulator current controller's open-loop transfer function is depicted in Fig 5.3. The designed PI compensators enable the achievement of a bandwidth of 2 kHz while ensuring a positive gain margin and, consequently, stability of the emulator system.

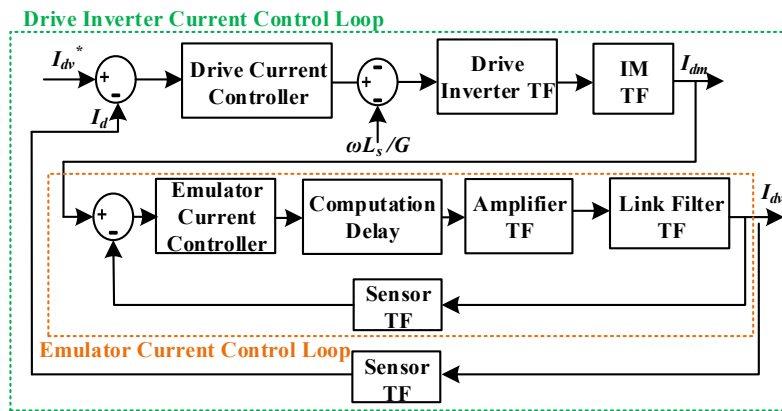


Fig 5. 2 Block diagram of the cascaded power amplifier current control loop within the driving inverter current control loop

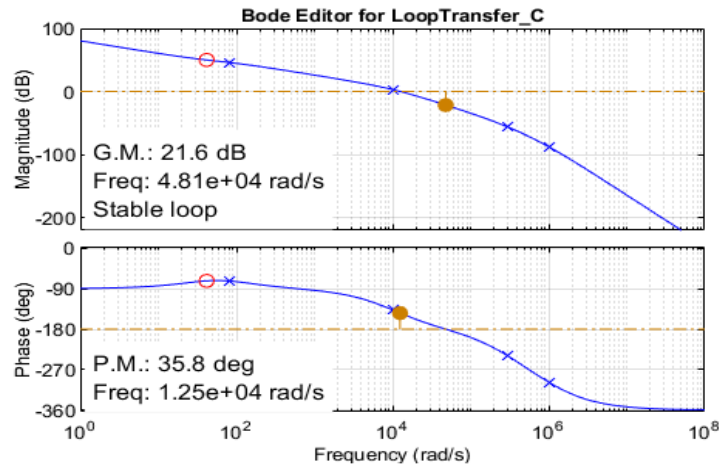


Fig 5. 3 Magnitude and phase plots for the emulator current control open-loop transfer function

5.1.2. Drive inverter control design

The subsequent step involves designing the bandwidth of the drive inverter, as previously mentioned. Given that the drive inverter serves as the outer loop of the emulator system, this current loop needs to be designed accurately to ensure stability for the emulator system. The closed-loop transfer function of the emulator system can be approximated as a first-order transfer function, with the time constant (τ_{emu}) derived from the bandwidth of the emulator current controller. The closed-loop time constant is 79.5 μ s. The drive inverter transfer function can be considered a first-order transfer function, with G representing half of the drive inverter DC link voltage (150 V), and T_{sw} being half of the switching period of the inverter (25 μ s). The drive inverter controller is implemented on the CPU board of the RTS. The CPU sample time, denoted as T_s , is 20 μ s. A PI controller is utilized for the drive inverter control design. Various approaches have been proposed for designing a current loop controller for a motor drive system with an LC filter. Typically, these methods utilize cascaded controllers, necessitating additional sensors [92]. However, this work proposes a cost-effective implementation of the controller for a machine drive with an LC filter, enabling precise control design for the motor emulator system. To achieve this, the transfer function representing the input and output of the induction motor (IM) with the LC filter ($G(s)_{LC\&IM}$) must be extracted. Figure 6 illustrates the equivalent circuit of the single-phase induction motor along with the LC filter. Here, R_s denotes the stator winding resistance, L_s is the stator winding inductance, L_M is the magnetizing reactance, R_r represents the rotor winding resistance, L_r is the rotor winding inductance, L_f signifies the filter inductance, C_f stands for the filter capacitor, and R_f indicates the filter damping resistance. The value of the LC filter can be calculated using:

$$f_c = \frac{1}{2\pi\sqrt{L_f C_f}} \quad (5-2)$$

The cutoff frequency (f_c) of such a filter should be greater than the fundamental frequency of the IM and less than the switching frequency of the drive inverter. This ensures that the filter minimally impacts the control loop of the motor while effectively attenuating the harmonics caused by inverter switching. Additionally, damping resistors are included to limit resonance. The detailed description of the LC filter design for motor drive is well-documented [93]. In this work, f_c is selected as 1 kHz which is placed away from the motor fundamental frequency (57 Hz at the rated

speed) and the switching frequency (20 kHz), the value of L_f is 0.0025H, C_f is 10 μ F, R_f is 1 Ω . Once the LC filter is designed, the transfer function related to the inverter voltage (V_{inv}) and inverter current (i_{inv}) for the induction motor with the LC filter is derived using an equivalent circuit (Fig 5.4).

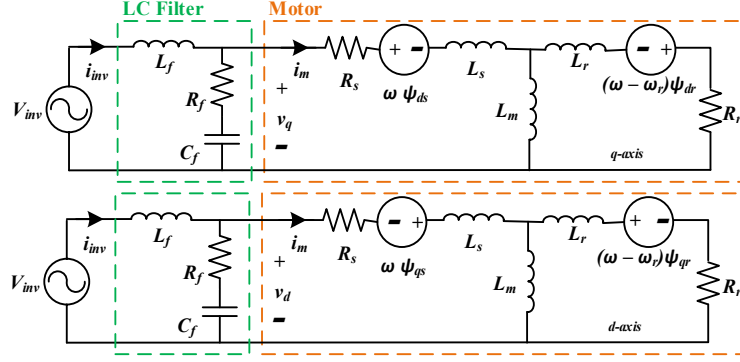


Fig 5. 4 LC filter along with three phase IM dq axis equivalent circuit

Equation (5-3) shows this transfer function:

$$\frac{i_{inv}}{V_{inv}} = \frac{\left(\frac{(R_r+sL_r)sL_m}{(R_r+sL_r)+sL_m}+R_s+sL_s\right)\left(R_f+\frac{1}{sC_f}\right)}{\left(\frac{(R_r+sL_r)sL_m}{(R_r+sL_r)+sL_m}+R_s+sL_s\right)+\left(R_f+\frac{1}{sC_f}\right)} + L_f \quad (5-3)$$

(5-3) is simplified, and then (5-5) is derived from (5-4).

$$\frac{i_{inv}}{V_{inv}} = \frac{((L_f+R_f)((L_r+L_s)L_m+L_rL_s)C_f s^3 + (((L_f+R_f)R_r + (R_f+R_s)L_f + R_sR_f)L_m + ((R_f+R_s)L_f + R_sR_f)L_r + L_sR_r(L_f+R_f))C_f + (L_r+L_s)L_m + L_rL_s)s^2 + ((R_f+R_s)L_f + R_sR_f)R_rC_f + (L_f+R_r+R_s)L_m + (L_f+R_s)L_r + R_rL_s)S + R_r(L_f+R_s)}{(C_f((L_r+L_s)L_m + L_rL_s)S^3 + ((R_f+R_r+R_s)L_m + (R_f+R_s)L_r + R_rL_s)C_f s^2 + ((R_f+R_s)R_rC_f + L_m + L_r)S + R_r)} \quad (5-4)$$

$$G_{LC\&IM}(s) =$$

$$\frac{(C_fL_fL_mL_r + C_fL_fL_mL_s + C_fL_fL_rL_s + C_fL_mL_rR_f + C_fL_mL_sR_f + C_fL_rL_sR_f)s^3 + (C_fL_fL_mR_f + C_fL_fL_mR_r + C_fL_fL_mR_s + C_fL_fL_rR_f + C_fL_fL_rR_s + C_fL_fL_sR_r + C_fL_mR_fR_r + C_fL_mR_fR_s + C_fL_rR_fR_s + L_mL_r + L_mL_s + L_rL_s)s^2 + (C_fL_fR_fR_r + C_fL_fR_rR_s + C_fR_fR_rR_s + L_mL_f + L_rL_f + L_mR_r + L_mR_s + R_sL_r + R_rL_s)S + L_fR_r + R_rR_s}{(L_mL_rC_f + L_mL_sC_f + L_rL_sC_f)s^3 + (C_fL_mR_f + L_mR_rC_f + L_mR_sC_f + C_fL_rR_f + R_sL_rC_f + R_rL_sC_f)s^2 + (R_rC_fR_f + R_rC_fR_s + L_m + L_r)S + R_r} \quad (5-5)$$

The transfer function of the drive inverter current controller can be written as (5-6).

$$G_{drive}(s) = \left(\frac{K_I}{s} + K_p\right) \left(\frac{1}{1 + s\tau_{emu}}\right) \left(\frac{G}{1 + sT_{sw}}\right) \left(\frac{1}{1 + sT_s}\right) (G(s)_{LC\&IM}) \quad (5-6)$$

Using the zero-pole cancellation method, the PI controller is designed. Fig 5.5 shows the Bode plot of the current loop open-loop transfer functions. The test-inverter current controller gains are calculated using the Bode plots of the test-inverter inner current loop depicted in Fig 5.5. This figure illustrates the maximum achievable bandwidth which is limited by the resonant pole. This design exercise has demonstrated the feasibility of the emulating converter current control method proposed.

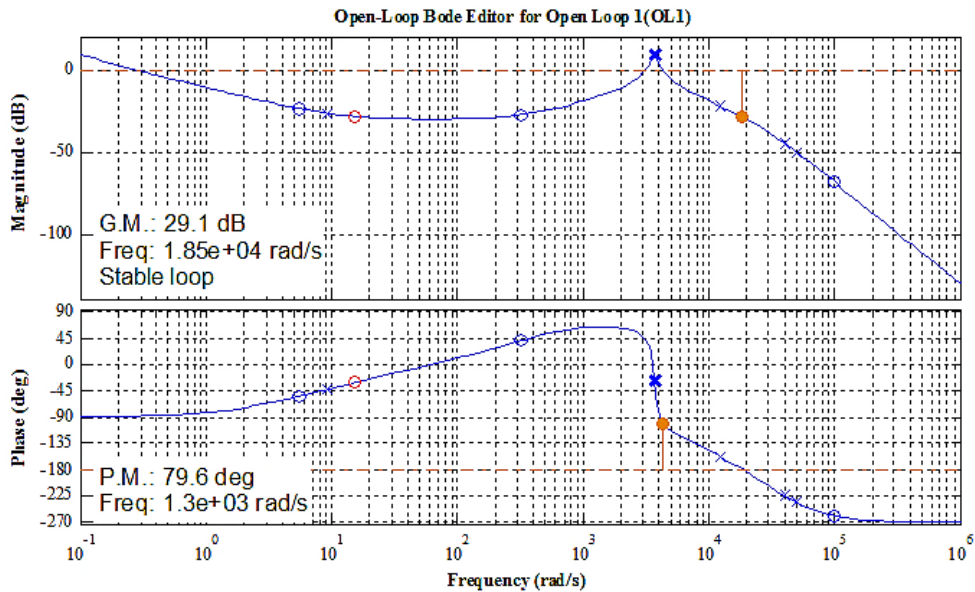


Fig 5. 5 Magnitude and phase plots for the driving inverter current control open-loop transfer function

5.1.3. Zero sequence control design

As mentioned previously, a zero-sequence current path is formed when the DC link of the drive inverter is connected to the EC. Even a small difference between the two common-mode voltages can cause a large zero-sequence circulating current. Thus, it is crucial to suppress this circulating current. Several methods have been proposed in the literature to mitigate the effects of this common-mode current. For example, one method uses a common-mode choke to suppress the common-mode voltage [94], while another modifies the modulation through specific switching combinations. However, these methods require additional hardware or complicated calculations

[95]. Therefore, this research work proposes using a PI controller to mitigate the zero-sequence current. The same design procedure explained in the emulator current controller design has been applied here.

5.2. Control in the loop simulation

Control-in-the-loop simulation results are presented in this section to validate the functionality of the proposed IM with LC filter emulator system. The CHIL setup is shown in Fig 5.6 (a), consisting of a real-time simulator (OP4610) and DSP (OP8666). The RTS is utilized to implement the proposed machine emulation system, while the DSP is utilized for implementing the drive inverter control. The machine model is implemented in the FPGA core of the RTS to achieve a low simulation time step. The stator currents and the rotor position are output from the machine model, which is implemented on the FPGA board of the RTS using the electric hardware solver (eHS). These signals are directed to the analog output (AO) and incremental encoder output ports of RTS. They are then read using the analog input (AI) ports and digital input (DI) ports of the DSP and utilized as the drive control feedback signals. The drive controller generates PWM pulses, which are output on the digital output (DO) port of RTS. These PWM pulses are then read through the digital input port of RTS and fed into the eHS model. This connection is shown in Fig 5.6 (b).

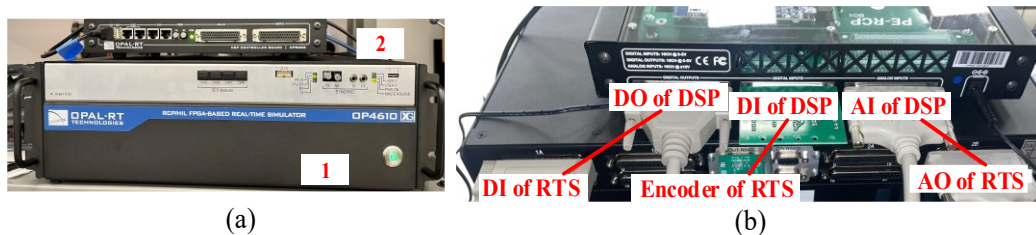


Fig 5. 6 CHIL setup (a)-(1) RTS, (a)-(2) DSP, (b) connection of RTS and DSP

To further investigate the effect of the drive inverter bandwidth on the stability of the emulation system, the bandwidth of the drive inverter is varied while the emulator system bandwidth is fixed. Fig 5.7 and Fig 5.8 present the results obtained from the CHIL IM drive testing with and without LC filter respectively. In the results, phase A emulated current and q-axis current measured for varying drive inverter bandwidths are provided. It can be observed that as the drive inverter bandwidth increases and approaches that of the emulator system, the emulation system loses accuracy and stability.

Fig 5.7 presents the CHIL results for the IM emulator system under steady-state conditions, with the machine speed at 700 rpm and the q-axis reference set to 6A. Fig 5.8 shows the results for the IM emulation with an LC filter drive under the same conditions. The reference phase A IM model current ($I_{emu\ ref}$), phase A emulated current (I_{emu}), and q-axis current are measured. These results demonstrate that the drive inverter current loop bandwidth should be at least five times less than the emulator current control bandwidth. However, when designing the drive with an LC filter, the emulation system's bandwidth should be ten times less than the emulator's bandwidth. This requirement is mainly due to the resonance frequency of the LC filter drive.

These results demonstrate that the drive inverter current loop bandwidth should be at least five times less than the emulator current control bandwidth. However, when designing the drive with an LC filter, the emulation system's bandwidth should be eight times less than the emulator's bandwidth. This requirement is mainly due to the resonance frequency of the LC filter drive. Referring to Figure 5.5, this means that the emulation system with an LC filter drive should have a 20dB gain margin and a 150-degree phase margin.

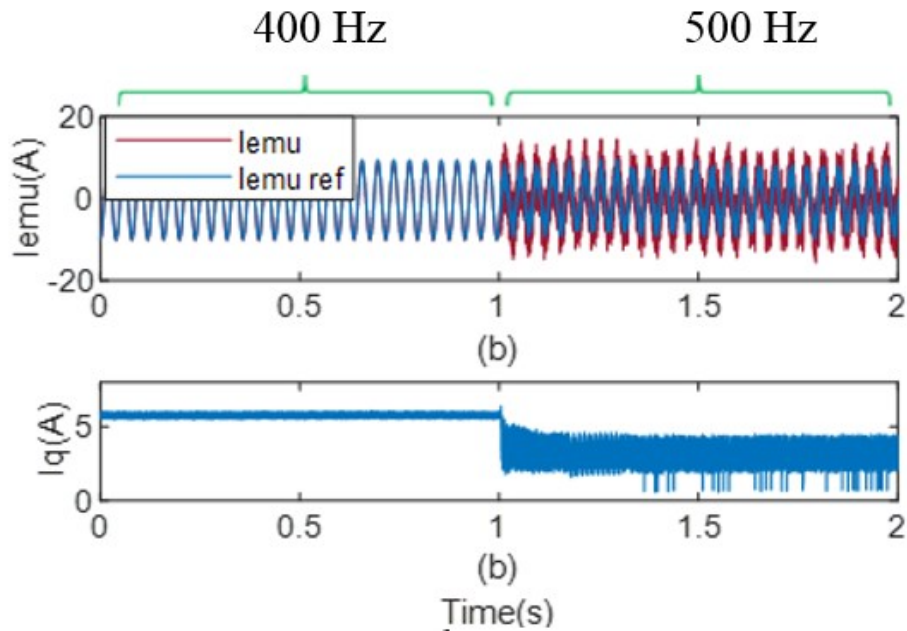


Fig 5. 7 Machine emulator response for a fixed emulator current bandwidth and varying the drive-inverter current-loop bandwidth

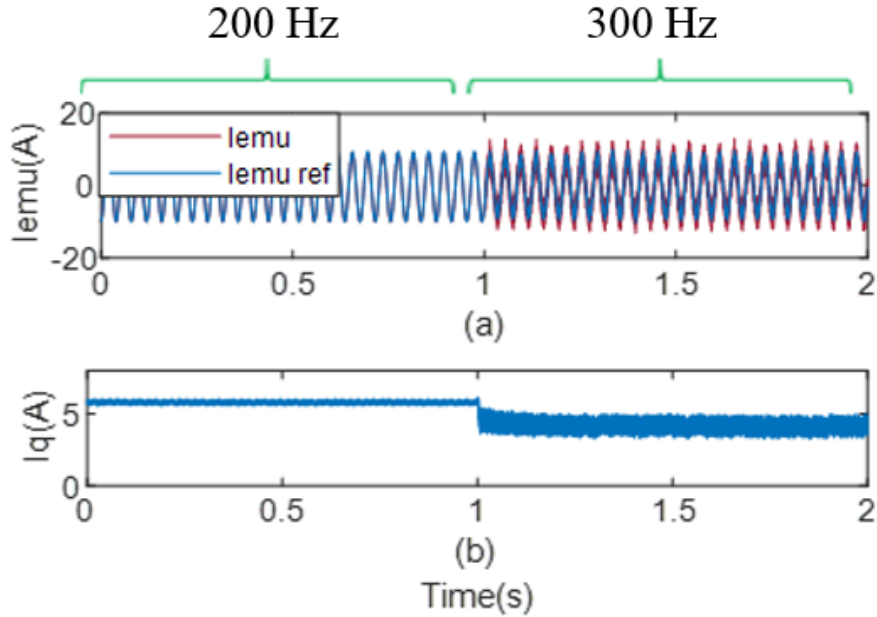


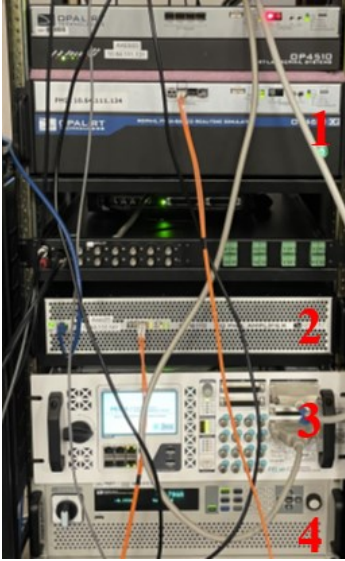
Fig 5. 8 Machine emulator response for a fixed emulator current bandwidth and varying the LC filter drive-inverter current-loop bandwidth

5.3. Experimental setups and results

5.3.1. Experimental setups

The proposed PHIL-based emulator system, as shown in Fig 5.9, consists of a four-quadrant Class D power amplifier. The OP8110 power amplifiers have a power sinking and sourcing capability of 5 kW and a bandwidth of 10 kHz. The control of these Class D power amplifiers is performed through a high-speed fiber optic (SFP) link. The controller for the power amplifiers is implemented in the FPGA board of the RTS (OP4510). A bidirectional DC power supply is used to maintain the 500V DC for this module. The Class D power amplifier is connected to the drive inverter through the coupling inductor of 2.5 mH on each phase. The standard two-level IGBT switch-based inverter is selected for the drive inverter. A DC-DC converter is used to maintain a 300V DC bus voltage for the inverter. The same 500V DC power supply is connected to the input of the DC-DC converter. The drive inverter switching frequency is set to 20 kHz. The controller for the drive inverter is implemented in the CPU of the RTS as the current controller bandwidth is low and it doesn't require a low sample time for the implementation. The sampling time of the drive controller is 20 μ s. The output of the drive inverter is connected to the LC filter,

with the values designed such that the filter inductor is 0.0035H, the filter capacitor is 10 μ F, and the damping resistance is 1 Ω . The IM mathematical model is implemented in the FPGA board of this RTS using electrical hardware synchronization (eHS). The data acquisition is selected for recording the data.



- (1) RTS
- (2) power amplifier (AC mode)
- (3A) DC-DC converter /Drive Inverter
- (4) DC supply for the power amplifier
- (5) Data acquisition

Fig 5. 9 Experimental setup of IM emulator system



- (1) Speed sensor
- (2) Coupled dynamometer
- (3) Prototype machine
- (4) Drive inverter for the machine
- (5) RTS
- (6) LC filter
- (7) Data acquisition

Fig 5. 10 Experimental setup for the prototype squirrel-cage induction IM coupled to induction motor dynamometer

The same drive inverter is utilized to power a prototype squirrel cage induction machine with an LC filter, as depicted in Fig 5.10. The prototype machine is a 4-pole, 120V, 10A induction motor. The measured stator self-inductance, rotor self-inductance, mutual inductance, stator resistance, and rotor resistance are as follows: 1.8 H, 4.4 H, 76.5 H, 0.6 Ω , and 4.3 Ω respectively. This machine is connected to an induction motor dynamometer to apply the required load torque. Experimental results obtained from the physical dynamometer setup are validated against those obtained from the emulator system.

5.3.2. Zero sequence controller results

With the aim of verifying the impacts of the zero-sequence current controller (ZSC) on the IM emulator system, results were obtained from the emulator system before and after applying the ZSC in steady-state conditions with the q-axis reference current set to 6A. Figure 5.11 presents the measured phase A emulated current (a), the q-axis current (b), the machine speed (c), and the inverter line-to-line voltage (d). The same operating conditions were applied to the IM motor emulation with an LC filter, and the results are presented in Figure 5.12. These results verify that before applying the ZSC, there is a zero-sequence current present in the emulated current, which is effectively compensated using the proposed ZSC.

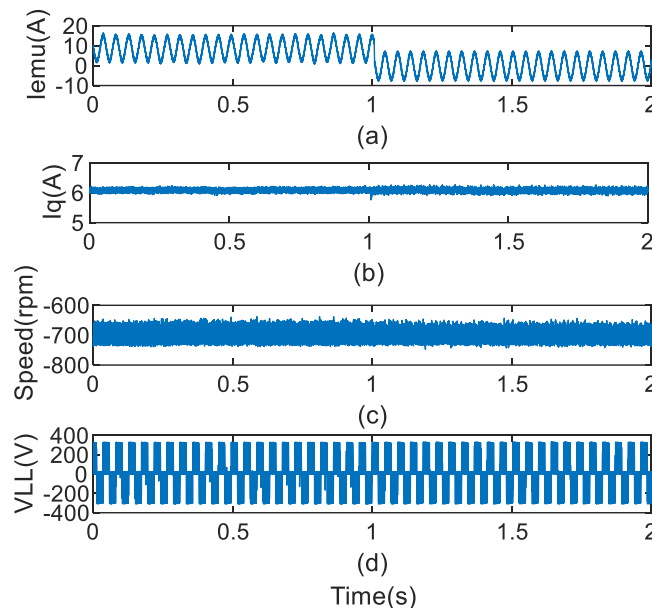


Fig 5. 11 Experimental results obtained for IM emulator before and after applying zero sequence current controller. (a) phase A emulated current (b) emulator q axis current (c) drive inverter terminal line–line voltage (d) machine speed

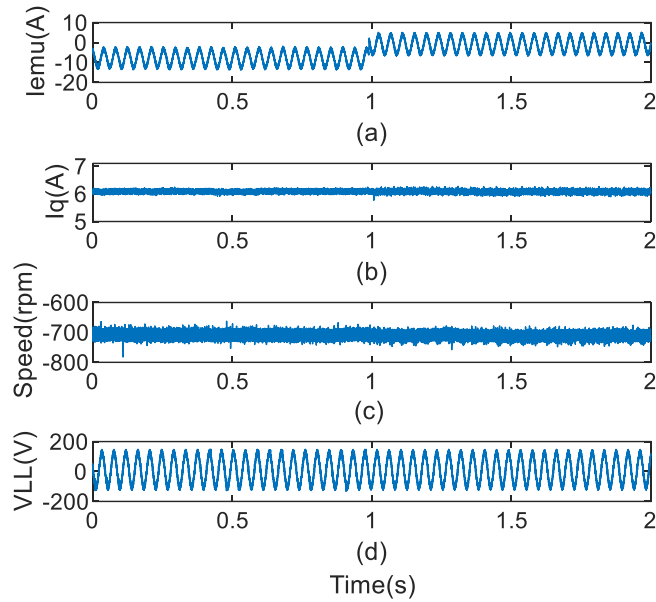


Fig 5. 12 Experimental results obtained for IM emulator with LC filter drive before and after applying zero sequence current controller. (a) phase A emulated current (b) emulator q axis current (c) drive inverter terminal line–line voltage (d) machine speed

5.3.3. Step change results

Figs 5.13, 14, 15, and 16 present results related to the machine start-up from zero to 6 A at a constant speed of -700 rpm, obtained from the emulator system, the emulator system with an LC filter, a physical dynamometer setup, and a physical machine with an LC filter, respectively. As can be seen, there is a close match between these results, demonstrating the effective emulation capabilities of the system.

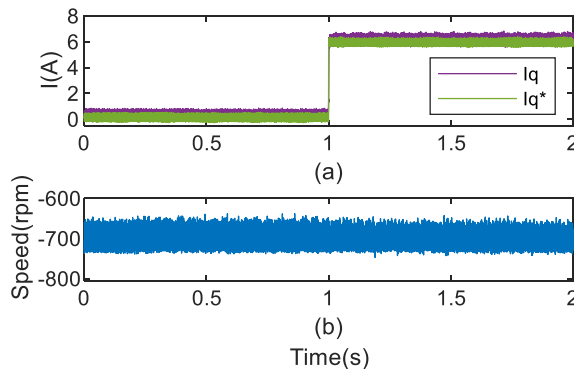


Fig 5. 13 Experimental results of emulator response for a step change in torque (a) emulated machine q axis reference generated within the real time and q axis emulated current (b) emulated machine speed

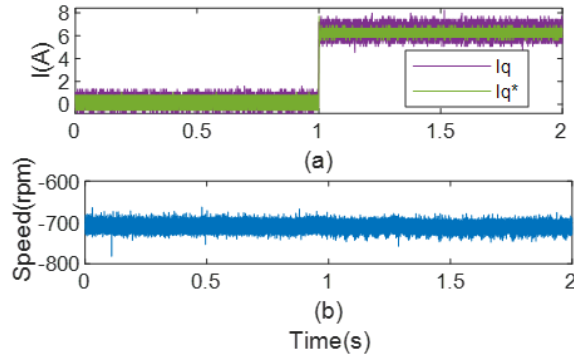


Fig 5. 14 Experimental results of prototype IM response for a step change in torque (a) machine q axis reference generated within the real time and q axis machine current (b) machine speed

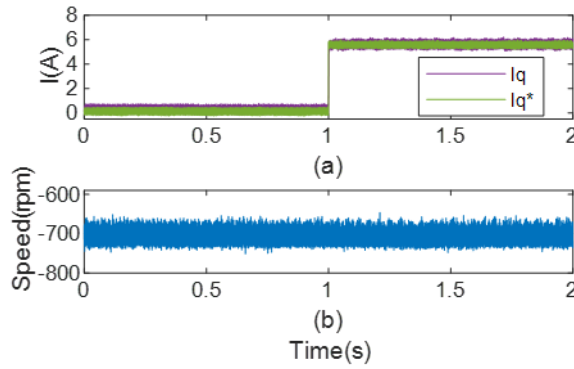


Fig 5. 15 Experimental results of emulator with LC filter response for a step change in torque (a) emulated machine q axis reference generated within the real time and q axis emulated current (b) emulated machine speed

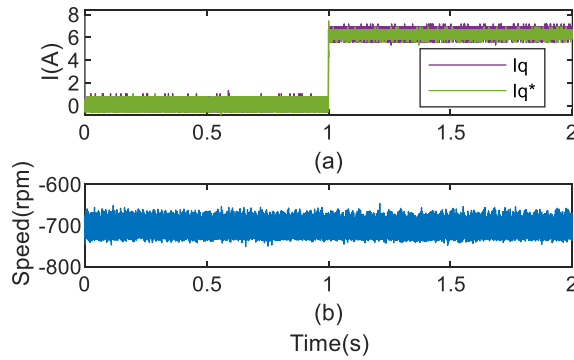


Fig 5. 16 Experimental results of prototype IM with LC filter response for a step change in torque (a) machine q axis reference generated within the real time and q axis machine current (b) machine speed

In Figs 5. 13(a) and 5. 15(a), the q-axis emulated current is shown, closely following the machine's q-axis model current. Similarly, Figs 5.14(a) and 5.16(a) display the q-axis machine

current, which closely follows the q-axis reference current. Figs 5.13(b) and 5.15(b) additionally show the measured speed from the machine model in the RTS. Figures 5.14(b) and 5.16(b) show the measured speed from the physical machine, both without an LC filter drive and with an LC filter drive.

Figs 5.17, 19, 18, and 20 present the results obtained from the torque change from 6 to 0 A at a constant speed of -700 rpm. The results are measured from the emulator system, the emulator system with an LC filter, a physical dynamometer setup, and a physical machine with an LC filter, respectively.

Fig 5.17 (a)-(d) include the emulated phase-A current, the emulated q-axis current, the speed generated by the motor model, and the inverter line-to-line voltage. The same results have been obtained from the proposed drive with an LC filter, as can be seen in Figs 5.19(a)-(d).

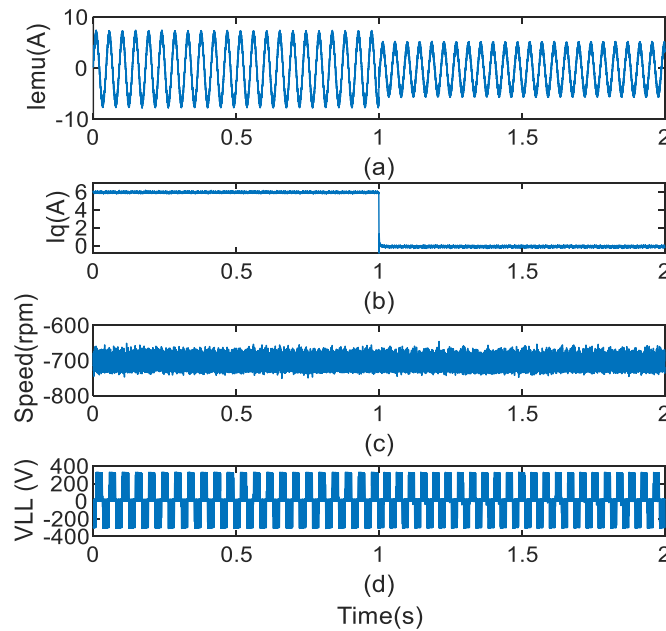


Fig 5. 16 Experimental results of emulator response for a step change in torque (a) phase A emulated machine current (b) q axis emulated current (c) emulated machine speed (d) drive inverter terminal line-line voltage

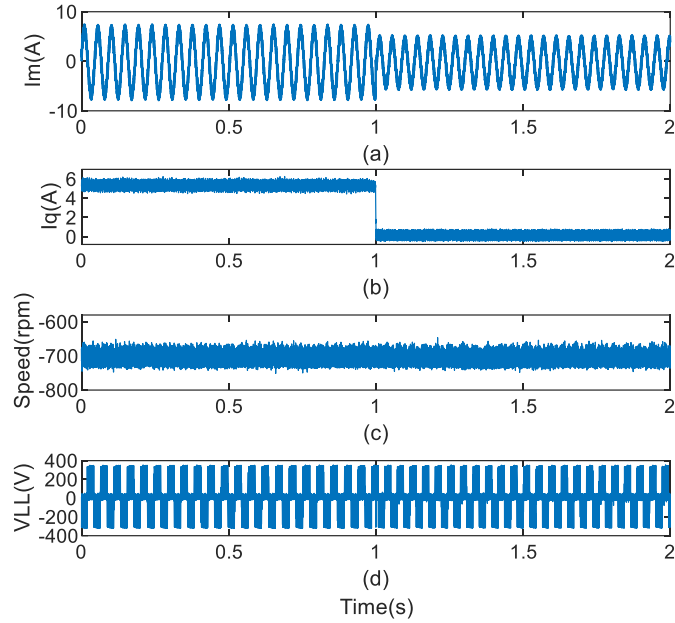


Fig 5. 17 Experimental results of prototype IM with response for a step change in torque (a) phase A machine current (b) q axis machine current (c) machine speed (d) drive inverter terminal line-line voltage

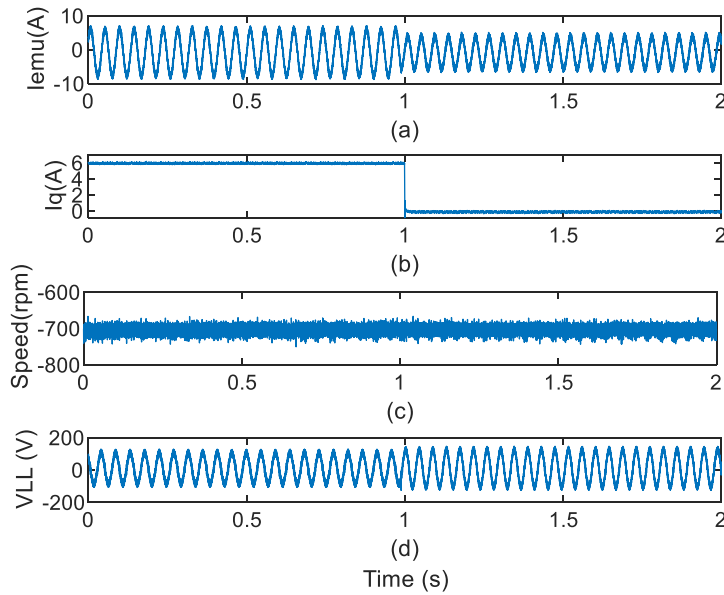


Fig 5. 18 Experimental results of emulator with LC filter response for a step change in torque (a) phase A emulated machine current (b) q axis emulated current (c) emulated machine speed (d) drive inverter terminal line-line voltage

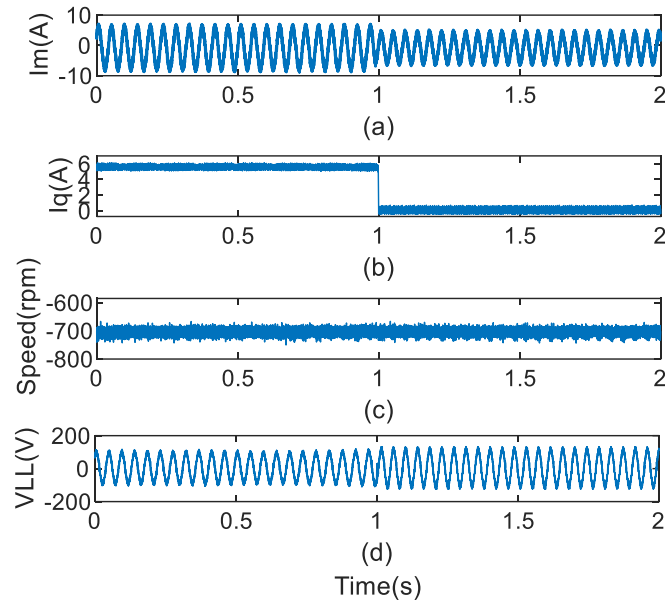


Fig 5. 19 Experimental results of prototype IM with LC filter response for a step change in torque (a) phase A machine current (b) q axis machine current (c) machine speed (d) drive inverter terminal line-line voltage

Figs 5.18 (a)-(d) present the experimental results for the physical IM machine, including measured machine phase A current, machine q-axis current, machine speed, and inverter line-to-line voltage under load torque change condition. Similar results are obtained from the IM drive with an LC filter, as shown in Figures 5.20 (a)-(d).

The close match between the physical motor results and the emulation system results under various transient conditions confirms the proposed system's ability to emulate the IM motor with LC filter.

5.3.4. Harmonic analysis results

This section evaluates motor emulation accuracy by comparing the obtained results from the emulator system drive with an LC filter and without a filter. The factor indicating emulator performance is the total harmonic distortion (THD) in the emulated phase currents. Table 5.1 compares THD magnitudes in phase currents under no-load and loaded conditions. It is evident that using the drive with an LC filter can reduce the harmonic content of the emulation system.

Table 5. 1 Comparative THD% analysis of phase A emulated current and motor

Control method	Magnitude of THD percentage for phase A current in no load condition	Magnitude of THD percentage for phase A current in load condition
Motor	%2.02	%34.52
Motor with LC filter	%1.74	%31.21
IM emulator	%5.58	%27.03
IM emulator with LC filter	%2.98	%23.40

5.4. Summary

The chapter proposes a PHIL-based IM emulator system using a Class D power amplifier for testing the drive with an LC filter. The developed emulator system enables the emulation of an IM under various operating conditions. The research work provides a description of the emulator system along with a detailed control design to ensure the stability of the emulation system. Subsequently, to verify the utility and functionality of the proposed work, control-in-the-loop simulations are presented. Then, experimental results are obtained from the developed machine emulator and physical squirrel cage IM. The emulator results show strong agreement with those obtained from the physical IM drive equipped with an LC filter under various transient conditions. This serves to validate the accuracy and effectiveness of the proposed machine emulator system.

Chapter 6 Conclusion and future works

The focus of this Ph.D. research work was on grid and induction machine emulation. This research is devoted to:

- Developing and investigating a grid emulator system with a transformer: Using this type of configuration increases the safety, reliability, flexibility, and robustness of grid-connected equipment. The platform offers a sinusoidal voltage waveform with adjustable magnitude and various frequencies. In addition, the grid emulator can simulate non-ideal grid conditions, such as grid unbalance and voltage distortion.
- Developing three motor emulation test setups: These setups include power electronic converter-based, Class D power amplifier-based, and linear amplifier-based systems. Each setup accurately mimics the behavior of actual induction machines. These testbeds can replace real induction machines, allowing for the development and testing of machine drive techniques without risking damage to expensive equipment. Using these emulation setups significantly reduces the risk and cost associated with testing and analyzing electrical machines. They offer a safer and more cost-effective approach compared to traditional methods. The setups allow for comprehensive testing under various conditions, leading to better insights and more robust machine drive systems.

6.1. Conclusion

6.1.1. Reviewed grid emulation and induction machine emulation

Chapter 1 reviewed grid emulation and induction machine emulation

- Research indicates that various grid faults can arise during device testing and development, posing a risk of permanent damage to the equipment being tested. Therefore, the necessity of a grid emulator is emphasized. By utilizing a grid emulator, safety in testing procedures is enhanced, and it also facilitates the development of more robust grid-connected equipment. In essence, the grid emulator serves as a crucial tool in mitigating risks and optimizing the reliability and effectiveness of grid-connected devices.
- Machine emulation refers to power-hardware-in-the-loop simulation, which serves as a testing method for electric drives. A PHIL-based motor emulation is constructed using a set of power electronic converters or power amplifiers and controlled by real-time systems

to replicate the behavior of an electrical machine. This test methodology requires an accurate test bench. To be able to test different types of motors with different ratings in various operating conditions.

6.1.2. The grid emulator

Chapter 2 explores the impact of connecting a transformer to the grid emulator. It highlights that the interconnection of the transformer at the output of a power amplifier influences both the performance of the amplifier and the transformer. This interaction has been mathematically modeled to provide insight into the underlying dynamics. An experimental setup was developed to test the proposed system, and the experiments verified its functionality. The results demonstrate that the grid emulation system operates effectively under both steady-state and transient load conditions. Additionally, the chapter characterizes the amplifier and transformer across various operating scenarios, taking into account factors such as DC offset, total harmonic distortion (THD) levels, transformer thermal behavior, amplifier control bandwidth, and the system's startup performance. This comprehensive investigation ensures the reliability of the grid emulator with the transformer under different operating conditions.

6.1.3. Comparative study on machine emulation systems based on linear power amplifiers and switching converters

Chapter 3 presents a comparative study of machine emulation systems utilizing linear power amplifier and switching converters. It begins with a general description of induction machine emulation, particularly focusing on the startup condition, detailing common settings used during this phase. The chapter then delves into the control design of three distinct motor emulation configurations: one based on an IGBT inverter, another using a Class D power amplifier, and a third employing a linear power amplifier. A theoretical comparative analysis between these configurations is provided, followed by the development of experimental setups for each system. The test results obtained from these three emulator configurations are analyzed and compared against those from a physical prototype of an induction motor (IM). The comparison considers key factors such as emulator bandwidth, total harmonic distortion (THD), emulator error, design complexity, machine speed range and power level emulation capabilities, cost, and emulator size. This comprehensive analysis highlights the strengths and limitations of each approach for accurate machine emulation.

6.1.4. Harmonic compensation of a power-hardware-in-the-loop based emulator for induction machines

Chapter 4 addresses harmonic compensation in the emulator converter for induction machine emulation. The effect of inverter harmonics on the induction motor emulation system is thoroughly investigated. Since dead time is identified as the primary source of emulator converter harmonics, this effect is first mathematically modeled. The conventional emulator current controller loop is then modified to compensate for the dead time effect in the converter. Additionally, a novel Artificial Neural Network (ANN)-based harmonic compensation technique is developed to mitigate harmonics in the emulated motor currents. The effectiveness of the dead time and harmonic compensation methods is validated through experimental tests conducted under various operating conditions. The results obtained from the emulation system are compared to those of an actual machine, showcasing the improvements achieved through harmonic compensation.

6.1.5. PHIL based induction motor emulator with LC filter

Chapter 5 investigates the emulation of an induction motor (IM) with a drive incorporating an LC filter. The chapter outlines the control design procedure for emulating the IM drive and LC filter. It further explores the bandwidth design requirements for the drive with the LC filter. A control-in-the-loop simulation is conducted to evaluate the effect of the selected bandwidth on the performance and stability of the emulation system. An experimental setup is developed using a high-bandwidth Class D power amplifier to accurately emulate the IM drive with an LC filter. The results obtained from the IM drive emulation system are compared to those of the actual machine. Additionally, the results from the IM drive with an LC filter emulation system are compared to those of a physical machine with an LC filter under various transient conditions.

6.2. Future work

This research work can be further extended to:

- In Chapter 2, the grid emulator with a transformer can be further studied by considering grid harmonics in this configuration. Future research could focus on enhancing the grid emulator's capability to generate various harmonic orders.

Investigating the effect of these harmonics on transformer performance would provide valuable insights into optimizing grid emulation systems under realistic harmonic conditions.

- Chapter 3 focused on comparing the design procedures and configurations of three different types of emulator converters: IGBT-based inverter, Class D power amplifier, and linear power amplifier. However, future work could explore the control design and investigate the effects of various types of inverters, such as GaN inverters and multilevel inverters, on the emulation performance. This would provide deeper insights into optimizing emulator systems for different applications.
- In Chapter 4, a simplified mathematical model is used in the emulator system. Future work could focus on developing a detailed mathematical model that incorporates all machine harmonics, along with implementing a proper harmonic compensation method for this configuration. Addressing harmonic distortions effectively will enable the emulator system to replicate physical machines more accurately.
- In Chapter 5, the effect of the LC filter drive on the emulation system is investigated. However, future research could explore the impact of various novel drive inverter control structures on motor emulation systems.

References

- [1] Z. Yang, F. Shang, I. P. Brown and M. Krishnamurthy, "Comparative Study of Interior Permanent Magnet, Induction, and Switched Reluctance Motor Drives for EV and HEV Applications," in *IEEE Transactions on Transportation Electrification*, vol. 1, no. 3, pp. 245- 254, Oct. 2015.
- [2] A. M. El-Refaie, "Motors/generators for traction/propulsion applications: A review," in *IEEE Vehicular Technology Magazine*, vol. 8, no. 1, pp. 90-99, March 2013.
- [3] B. S. S. G. Yelamarthi and S. R. Sandepudi, "Predictive Torque Control of Three-Phase Induction Motor Drive With Inverter Switch Fault-Tolerance Capabilities," in *IEEE Journal of Emerging and Selected Topics in Power Electronics*, vol. 9, no. 3, pp. 2774-2788, June 2021.
- [4] P. Surana, K. Gopakumar, L. Umanand, K. Rajashekara and L. G. Franquelo, "A Variable Speed Induction Motor Drive With 24-Stepped Voltage Waveform Throughout Modulation Range," in *IEEE Transactions on Industrial Electronics*, vol. 71, no. 2, pp. 1268-1276, Feb. 2024.
- [5] L. Wu et al., "Design of Complex Vector Controller for High-Power Induction Machine Drive," in *IEEE Transactions on Transportation Electrification*, vol. 10, no. 1, pp. 1816-1826, March 2024.
- [6] M. V. Gururaj and N. P. Padhy, "PHIL Experimentation on Fault Ride Through Behavior of Doubly Fed Induction Generator-Based Wind System in the Presence of Fault Current Limiter," in *IEEE Transactions on Industry Applications*, vol. 56, no. 3, pp. 2988-3005, May-June 2020.
- [7] C. Calleja, A. López-de-Heredia, H. Gaztañaga, L. Aldasoro and T. Nieva, "Validation of a Modified Direct-Self-Control Strategy for PMSM in Railway-Traction Applications," in *IEEE Transactions on Industrial Electronics*, vol. 63, no. 8, pp. 5143-5155, Aug. 2016.
- [8] D. Ronanki, S. A. Singh and S. S. Williamson, "Comprehensive Topological Overview of Rolling Stock Architectures and Recent Trends in Electric Railway Traction Systems," in *IEEE Transactions on Transportation Electrification*, vol. 3, no. 3, pp. 724-738, Sept. 2017.

- [9] R. Solomon, M. A. Khan, P. S. Barendse, P. Pillay, K. A. Folly, "Review and application of micromachines for wind energy integration", Proc. Int. Conf. Elect. Mach. (ICEM), pp. 2151-2157, Sep. 2012.
- [10] K. Ma, J. Wang, X. Cai and F. Blaabjerg, "AC Grid Emulations for Advanced Testing of Grid-Connected Converters—An Overview," in IEEE Transactions on Power Electronics, vol. 36, no. 2, pp. 1626-1645, Feb. 2021.
- [11] G. Si and R. Kennel, "Switch mode converter based high performance power hardware-in-the-loop grid emulator," 2016 IEEE 2nd Annual Southern Power Electronics Conference (SPEC), Auckland, New Zealand, 2016, pp. 1-6.
- [12] K. Upamanyu and G. Narayanan, "Simplified Grid Emulator for Testing Grid-Connected Power Electronic Converters," 2020 IEEE International Conference on Power Electronics, Smart Grid and Renewable Energy (PESGRE2020), Cochin, India, 2020, pp. 1-6.
- [13] Z. Li et al., "Medium-Voltage Megawatt Power-Electronic-Based Grid Emulators: Testing Capability Requirements and Dynamics Challenges—A Review," in IEEE Journal of Emerging and Selected Topics in Power Electronics, vol. 12, no. 2, pp. 1545-1559, April 2024.
- [14] S. N. Afrasiabi, R. Thike, K. S. Amitkumar, C. Lai and P. Pillay, "Investigation of a Transformer Connected Power Amplifier for Grid Emulation," 2023 IEEE 14th International Conference on Power Electronics and Drive Systems (PEDS), Montreal, QC, Canada, 2023.
- [15] T. -F. Wu, Y. -H. Chang, C. -C. Hung and J. -Y. Chiu, "Three-Phase Four-Wire Inverter for Grid Emulator Under Wide Inductance Variation to Evaluate the Performance of Distributed Generator," in IEEE Open Journal of Industry Applications, vol. 4, pp. 260-268, 2023.
- [16] H. J. Slater, D. J. Atkinson, and A. G. Jack, "Real-time emulation for power equipment development. II. The virtual machine," IEE Proc.-Electr. Power Appl., vol. 145, no. 3, pp. 153–158, May 1998.
- [17] F. Alvarez-Gonzalez, A. Griffio, B. Sen and J. Wang, "Real-Time Hardware-in-the-Loop Simulation of Permanent-Magnet Synchronous Motor Drives Under Stator

- Faults," in IEEE Transactions on Industrial Electronics, vol. 64, no. 9, pp. 6960-6969, Sept. 2017.
- [18] S. Mojlish, N. Erdogan, D. Levine and A. Davoudi, "Review of Hardware Platforms for Real-Time Simulation of Electric Machines," in IEEE Transactions on Transportation Electrification, vol. 3, no. 1, pp. 130-146, March 2017.
- [19] W. Yu and I. Husain, "FPGA-Based High-Bandwidth Motor Emulator for Interior Permanent Magnet Machine Utilizing SiC Power Converter," in IEEE Journal of Emerging and Selected Topics in Power Electronics, vol. 9, no. 4, pp. 4340-4353, Aug. 2021.
- [20] R. S. Kaarthik and P. Pillay, "Emulation of a permanent magnet synchronous generator in real-time using power hardware-in-the-loop," 2016 IEEE International Conference on Power Electronics, Drives and Energy Systems (PEDES), Trivandrum, India, 2016, pp. 1-6.
- [21] H. Mohajerani, A. Hassan, M. S. Toulabi, U. Deshpande and N. C. Kar, "Artificial Neural Network-Based PMSM Modeling for the Electric Motor Emulation," 2022 International Conference on Electrical Machines (ICEM), Valencia, Spain, 2022, pp. 2365-2371.
- [22] C. -A. Cheng, C. -C. Chang, T. -S. Li, Z. -J. Chen and Y. -M. Chen, "Initial Rotor Position Startup Process Emulation Based on Electric Motor Emulator," 2020 IEEE 9th International Power Electronics and Motion Control Conference (IPEMC2020-ECCE Asia), Nanjing, China, 2020, pp. 605-610.
- [23] D. Wang, S. Ge, Q. Li, H. Sun and P. Xu, "A Novel Control Scheme for the Electric Motor Emulator to Improve the Voltage Emulation Accuracy," in IEEE Transactions on Power Electronics, vol. 39, no. 1, pp. 374-383, Jan. 2024.
- [24] M. V. Gururaj and N. P. Padhy, "PHIL experimentation on fault ride through behavior of doubly fed induction generator based wind system in the presence of fault current limiter," 2018 IEEMA Engineer Infinite Conference (eTechNxT), New Delhi, India, 2018, pp. 1-6.
- [25] H. Song et al., "Development and Evaluation of a Power Hardware-in-the-Loop (PHIL) Emulator Testbench for Aerospace Applications," 2021 IEEE Energy Conversion Congress and Exposition (ECCE), Vancouver, BC, Canada, 2021, pp. 4505-4512.

- [26] K. S. Amitkumar, R. Thike and P. Pillay, "Linear Amplifier-Based Power-Hardware-in-the-Loop Emulation of a Variable Flux Machine," in *IEEE Transactions on Industry Applications*, vol. 55, no. 5, pp. 4624-4632, Sept.-Oct. 2019.
- [27] K. S. Amitkumar and P. Pillay, "Power Hardware-in-the-Loop based Emulation of an Open-Winding Permanent Magnet Machine," 2020 IEEE Energy Conversion Congress and Exposition (ECCE), 2020.
- [28] T. K. Gaël, M. Boby and P. Pillay, "Power Hardware-In-The-Loop Emulation of a Brushless Dc Motor," 2023 IEEE Energy Conversion Congress and Exposition (ECCE), Nashville, TN, USA, 2023, pp. 6253-6258.
- [29] F. E. Fleming and C. S. Edrington, "Real-time emulation of switched reluctance machines via magnetic equivalent circuits," *IEEE Transactions on Industrial Electronics*, vol. 63, no. 6, pp. 3366–3376, June 2016.
- [30] K. S. Amitkumar, R. S. Kaarthik and P. Pillay, "A Versatile Power-Hardware-in-the-Loop-Based Emulator for Rapid Testing of Transportation Electric Drives," in *IEEE Transactions on Transportation Electrification*, vol. 4, no. 4, pp. 901-911, Dec. 2018.
- [31] M. A. Masadeh, K. S. Amitkumar and P. Pillay, "Power Electronic Converter-Based Induction Motor Emulator Including Main and Leakage Flux Saturation," in *IEEE Transactions on Transportation Electrification*, vol. 4, no. 2, pp. 483-493, June 2018.
- [32] Y. Liu, M. A. Masadeh and P. Pillay, "Power-Hardware-In-The-Loop-Based Emulation of a Self-Excited Induction Generator Under Unbalanced Conditions," in *IEEE Transactions on Industry Applications*, vol. 58, no. 1, pp. 588-598, Jan.-Feb. 2022.
- [33] Y. Liu, C. Boniface, P. Barendse and P. Pillay, "Power-Hardware-in-the-Loop Based Induction Motor Emulator with Rotor Cage Fault," 2022 IEEE Energy Conversion Congress and Exposition (ECCE), Detroit, MI, USA, 2022, pp. 1-6.
- [34] Y. Liu, L. Ralikalakala, P. Barendse and P. Pillay, "Power Hardware-in-the-Loop based Emulation of An Induction Machine with Stator Winding Faults," *IECON 2021 – 47th Annual Conference of the IEEE Industrial Electronics Society*, Toronto, ON, Canada, 2021, pp. 1-6.
- [35] J. -M. Zhong, C. -C. Chang and Y. -M. Chen, "Power Hardware-in-the-Loop Emulation for SPMSM Under Fault Scenarios," in *IEEE Transactions on Transportation Electrification*, vol. 10, no. 3, pp. 5880-5893, Sept. 2024.

- [36] K. S. Amitkumar, P. Pillay and J. Bélanger, "An Investigation of Power-Hardware-in-the-Loop- Based Electric Machine Emulation for Driving Inverter Open-Circuit Faults," in IEEE Transactions on Transportation Electrification, vol. 7, no. 1, pp. 170-182, March 2021.
- [37] K. S. Amitkumar, P. Pillay and J. Bélanger, "Hardware-in-the-loop Simulations of Inverter Faults in an Electric Drive System," 2019 IEEE Energy Conversion Congress and Exposition (ECCE), 2019, pp. 353-358.
- [38] G. Tanuku and P. Pillay, "Induction Machine Emulation for Variable Frequency Drive Converter Faults," in IEEE Journal of Emerging and Selected Topics in Industrial Electronics, 2022.
- [39] G. Tanuku and P. Pillay, "Induction Machine Emulation for Open Circuit and Short Circuit Grid Faults," in IEEE Transactions on Energy Conversion, 2022.
- [40] G. Tanuku and P. Pillay, "Emulation of an Induction Machine for Unbalanced Grid Faults," in IEEE Transactions on Industry Applications, vol. 57, no. 5, pp. 4625-4635, Sept.-Oct. 2021.
- [41] G. Tanuku and P. Pillay, "Emulation of induction machines subject to industrial grid harmonics," 2022 IEEE International Conference on Power Electronics, Smart Grid, and Renewable Energy (PESGRE), Trivandrum, India, 2022, pp. 1-6.
- [42] O. Vodyakho, M. Steurer, C. S. Edrington and F. Fleming, "An Induction Machine Emulator for High-Power Applications Utilizing Advanced Simulation Tools With Graphical User Interfaces," in IEEE Transactions on Energy Conversion, vol. 27, no. 1, pp. 160-172, March 2012.
- [43] T. Boller and R. M. Kennel, "Virtual Machine - A hardware in the loop test for drive inverters," in 13th European Conference on Power Electronics and Applications, Barcelona, 2009.
- [44] J. Noon et al., "Design and Evaluation of a Power Hardware-in-the-Loop Machine Emulator," 2020 IEEE Energy Conversion Congress and Exposition (ECCE), Detroit, MI, USA, 2020, pp. 2013-2019.
- [45] L. Bigarelli, M. di Benedetto, A. Lidozzi and L. Solero, "Stability and Accuracy Evaluation of LCL Coupling Networks for PMSM Emulation PHIL," 2022 IEEE Energy Conversion Congress and Exposition (ECCE), Detroit, MI, USA, 2022, pp. 1-7.

- [46] K. K. Nzimbakani, A. K. Lusala, J. M. M. Ndeko and J. Gyselinck, "Design and Implementation of a Low-Cost FPGA Based Real-Time Simulator for a Three-Phase Grid Emulator Including Neutral," 2023 International Conference on Electrical, Computer and Energy Technologies (ICECET), Cape Town, South Africa, 2023, pp. 1-6.
- [47] T. -F. Wu, Y. -H. Chang, C. -C. Hung and J. -Y. Chiu, "Three-Phase Four-Wire Inverter for Grid Emulator Under Wide Inductance Variation to Evaluate the Performance of Distributed Generator," in IEEE Open Journal of Industry Applications, vol. 4, pp. 260-268, 2023.
- [48] L. M. Tolbert et al., "Reconfigurable Real-Time Power Grid Emulator for Systems With High Penetration of Renewables," in IEEE Open Access Journal of Power and Energy, vol. 7, pp. 489-500, 2020.
- [49] Z. Li et al., "Power-Hardware Design and Topologies of Converter-Based Grid Emulators for Wind Turbines," in IEEE Journal of Emerging and Selected Topics in Power Electronics, vol. 11, no. 5, pp. 5001-5017, Oct. 2023.
- [50] P. S. Niklaus, J. A. Anderson, D. Bortis and J. W. Kolar, "Ultra-High Bandwidth GaN-Based Class-D Power Amplifier for Testing of Three-Phase Mains Interfaces of Renewable Energy Systems," 2019 8th International Conference on Renewable Energy Research and Applications (ICRERA), 2019, pp. 615-622.
- [51] J. Ye, S. Ji, G. Jie and S. Gao, "A Dead-Time Effect Elimination Method for Three-Phase Dual Inverters," 2024 6th International Conference on Energy Systems and Electrical Power (ICESEP), Wuhan, China, 2024, pp. 1539-1544.
- [52] A. I. Putri, A. Rizqiawan, T. Rachmilda, Y. Haroen and P. A. Dahono, "Suppressing dead-time effect in current-controlled three-phase PWM inverters by using virtual inductor," 2018 IEEE Applied Power Electronics Conference and Exposition (APEC), San Antonio, TX, USA, 2018, pp. 867-871.
- [53] Yan Liu, Hongqi Ben, Chunpeng Li and Daqing Wang, "Research of the dead-time compensation based on the three-phase grid-connected inverter," Proceedings of The 7th International Power Electronics and Motion Control Conference, Harbin, 2012, pp. 510-514.

- [54] D. -H. Lee and J. -W. Ahn, "A Simple and Direct Dead-Time Effect Compensation Scheme in PWM-VSI," in IEEE Transactions on Industry Applications, vol. 50, no. 5, pp. 3017-3025, Sept.-Oct. 2014.
- [55] T. Itkonen, J. Luukko, A. Sankala, T. Laakkonen and R. Pöllänen, "Modeling and Analysis of the Dead-Time Effects in Parallel PWM Two-Level Three-Phase Voltage-Source Inverters," in IEEE Transactions on Power Electronics, vol. 24, no. 11, pp. 2446-2455, Nov. 2009.
- [56] A. Lewicki, "Dead-Time Effect Compensation Based on Additional Phase Current Measurements," in IEEE Transactions on Industrial Electronics, vol. 62, no. 7, pp. 4078-4085, July 2015.
- [57] T. Boller and R. M. Kennel, "Virtual Machine - A hardware in the loop test for drive inverters," in 13th European Conference on Power Electronics and Applications, Barcelona, 2009.
- [58] L. Bigarelli, M. di Benedetto, A. Lidozzi and L. Solero, "Stability and Accuracy Evaluation of LCL Coupling Networks for PMSM Emulation PHIL," 2022 IEEE Energy Conversion Congress and Exposition (ECCE), Detroit, MI, USA, 2022, pp. 1-7.
- [59] W. Choi, W. Lee and B. Sarlioglu, "Effect of grid inductance on grid current quality of parallel grid-connected inverter system with output LCL filter and closed-loop control," 2016 IEEE Applied Power Electronics Conference and Exposition (APEC), Long Beach, CA, USA, 2016, pp. 2679-2686.
- [60] M. F. Cunha, C. B. Jacobina and N. B. de Freitas, "Grid-Connected Induction Motor Using a Floating DC-Link Converter Under Unbalanced Voltage Sag," in IEEE Transactions on Industry Applications, vol. 57, no. 2, pp. 1609-1618, March-April 2021.
- [61] L. Yang et al., "Development of converter based reconfigurable power grid emulator," 2014 IEEE Energy Conversion Congress and Exposition (ECCE), 2014, pp. 3990-3997.
- [62] J. Eloy-Garcia, J. C. Vasquez, and J. M. Guerrero, "Grid simulator for power quality assessment of micro-grids," IET Power Electronics, vol. 6, no. 4, pp. 700-709, April 2013.

- [63] V. Miskovic, V. Blasko, T. M. Jahns, A. H. C. Smith, and C. Romenesko, "Observer-based active damping of lcl resonance in grid-connected voltage source converters," *IEEE Transactions on Industry Applications*, vol. 50, no. 6, pp. 3977–3985, Nov 2014.
- [64] J. Lai et al., "Harmonic generation for renewable energy converter test," *IECON 2017 - 43rd Annual Conference of the IEEE Industrial Electronics Society*, 2017, pp. 2516-2521.
- [65] OPAL-RT, "Op8110 datasheet," OPAL-RT, Montreal, QC, Canada. [Online]. Available:https://www.opalrt.com/wpcontent/uploads/2019/08/OP8110_onepager_Mars2019_Final.pdf
- [66] Fuchs, Y. You and D. J. Roesler, "Modeling and simulation, and their validation of three-phase transformers with three legs under DC bias," in *IEEE Transactions on Power Delivery*, vol. 14, no. 2, pp. 443-449, April 1999.
- [67] M. A. Rahman, M. R. Islam, A. M. Mahfuz-Ur-Rahman, K. M. Muttaqi and D. Sutanto, "Investigation of the Effects of DC Current Injected by Transformer-Less PV Inverters on Distribution Transformers," in *IEEE Transactions on Applied Superconductivity*, vol. 29, no. 2, pp. 1-4, March 2019, Art no. 0602904.
- [68] Y. Pan, X. Yin, Z. Zhang, B. Liu, M. Wang, and X. Yin, "Three-Phase Transformer Inrush Current Reduction Strategy Based on Prefluxing and Controlled Switching," *IEEE Access*, vol. 9, pp. 38961-38978, 2021.
- [69] A. Alassi, K. H. Ahmed, A. Egea-Alvarez and C. Foote, "Transformer Inrush Current Mitigation Techniques for Grid-Forming Inverters Dominated Grids," in *IEEE Transactions on Power Delivery*, vol. 38, no. 3, pp. 1610-1620, June 2023.
- [70] M. Jaworski and J. Jaeger, "Sympathetic Transformer Inrush Detection and Relay Blocking During Power System Restoration," in *IEEE Transactions on Power Delivery*, vol. 38, no. 4, pp. 2408-2417, Aug. 2023.
- [71] J. H. Brunke and K. J. Frohlich, "Elimination of transformer inrush currents by controlled switching. I. Theoretical considerations," in *IEEE Transactions on Power Delivery*, vol. 16, no. 2, pp. 276-280, April 2001.
- [72] A. Kermanizadeh, M. T. Mercan and P. Pillay, "Thermal Model of a Soft Magnetic Composite EV Permanent Magnet Traction Motor," 2024 IEEE Transportation Electrification Conference and Expo (ITEC), Chicago, IL, USA, 2024, pp. 1-5.

- [73] AE Techron, "Aetechron-7548 datasheet," AE Techron, Inc., Elkhart, IN, USA, 201. [Online]. Available: [http://aetechron.com/pdf/7548spec sheet.pdf](http://aetechron.com/pdf/7548spec%20sheet.pdf)
- [74] <https://www.taraztechnologies.com/products/power-electronics/inverters-converters/>
- [75] IEEE Standard Test Procedure for Polyphase Induction Motors and Generators," in IEEE Std 112-2017 (Revision of IEEE Std 112-2004) , vol., no., pp.1-115, 14 Feb. 2018.
- [76] S. N. Afrasiabi, C. Lai and P. Pillay, "Dead Time Analysis of a Power-Hardware-in-the-Loop Emulator for Induction Machines," IECON 2021 – 47th Annual Conference of the IEEE Industrial Electronics Society, Toronto, ON, Canada, 2021, pp. 1-6.
- [77] A. Guha and G. Narayanan, "Impact of Undercompensation and Overcompensation of Dead-Time Effect on Small-Signal Stability of Induction Motor Drive," in IEEE Transactions on Industry Applications, vol. 54, no. 6, pp. 6027-6041, Nov.-Dec. 2018.
- [78] Seung-Gi Jeong and Min-Ho Park, "The analysis and compensation of dead-time effects in PWM inverters," in IEEE Transactions on Industrial Electronics, vol. 38, no. 2, pp. 108-114, April 1991.
- [79] L. Ben-Brahim, "The analysis and compensation of dead-time effects in three phase PWM inverters," IECON '98. Proceedings of the 24th Annual Conference of the IEEE Industrial Electronics Society (Cat. No.98CH36200), Aachen, Germany, 1998, pp. 792-797 vol.2.
- [80] V. M. Cardenas, S. Horta and R. Echavarria, "Elimination of dead time effects in three phase inverters," V IEEE International Power Electronics Congress Technical Proceedings, CIEP 96, Cuernavaca, Mexico, 1996, pp. 258-262.
- [81] N. Aizawa, M. Kikuchi, H. Kubota, I. Miki and K. Matsuse, "Dead-time effect and its compensation in common-mode voltage elimination of PWM inverter with auxiliary inverter," The 2010 International Power Electronics Conference - ECCE ASIA -, Sapporo, Japan, 2010, pp. 222-227.
- [82] Q. Yan, X. Yuan, X. Wu and Y. Geng, "Analysis and Compensation of Dead-Time Effect in SiC-Device-based High-Switching-Frequency Inverters," 2018 International Power Electronics Conference (IPEC-Niigata 2018 -ECCE Asia), Niigata, Japan, 2018, pp. 619-625.

- [83] Hengbing Zhao, Q. M. J. Wu and A. Kawamura, "An accurate approach of nonlinearity compensation for VSI inverter output voltage," in *IEEE Transactions on Power Electronics*, vol. 19, no. 4, pp. 1029-1035, July 2004.
- [84] B. C. Neagu, G. Grigoraş and F. Scarlatache, "The influence of harmonics on power losses in urban distribution networks," 2016 International Symposium on Fundamentals of Electrical Engineering (ISFEE), 2016.
- [85] J. Ye, S. Huang, L. Liu, L. Li, J. Xu and A. Shen, "Accurate Harmonic Calculation for Digital SPWM of VSI With Dead-Time Effect," in *IEEE Transactions on Power Electronics*, vol. 36, no. 7, pp. 7892-7902, July 2021.
- [86] Bose, B. K. "Base/Gate Drive Suppression of Inactive Power Devices of a Voltage-Fed Inverter and Precision Synthesis of AC Voltage and DC Link Current Waves," *IEEE-IECON Conf. Rec*, vol. 2. pp.1030-1040. 1990.
- [87] S. Huang, J. Xu, J. Ye and A. Shen, "Generalized Accurate Harmonic Calculation Method Based on Discretized Double Fourier Series to Solve Double-Pulse Phenomenon," in *IEEE Transactions on Industrial Electronics*, vol. 70, no. 6, pp. 5651-5661, June 2023.
- [88] E. Oggier, G. G. Oggier, F. Botteron and G. O. García, "Closed-Form Harmonic Compensation Using Resonant Controllers Applied to Four-Leg VSI," in *IEEE Journal of Emerging and Selected Topics in Power Electronics*, vol. 11, no. 4, pp. 3853-3863, Aug. 2023.
- [89] M. Elghonimy, M. Fawzi, A. E. Kalas and G. A. Azeem, "Proportional resonant controller with resonant harmonic compensators for three-phase static frequency converter feeding nonlinear loads," 2017 Nineteenth International Middle East Power Systems Conference (MEPCON), Cairo, Egypt, 2017, pp. 308-313.
- [90] B. K. Bose, "Neural network applications in power electronics and motor drives—An introduction and perspective," *IEEE Trans. Ind. Electron.*, vol. 54, no. 1, pp. 14–33, Feb. 2007.
- [91] A. Kaymanesh, M. Babaie, A. Chandra and K. Al-Haddad, "PEC Inverter for Intelligent Electric Spring Applications Using ANN-Based Controller," in *IEEE Journal of Emerging and Selected Topics in Industrial Electronics*, vol. 3, no. 3, pp. 704-714, July 2022.

- [92] W. Geng, Z. Zhang and Q. Li, "Analysis and Experimental Verification of a Conventional Inverter With Output LC Filter to Drive Ironless Stator Axial-Flux PM Motor," in IEEE Transactions on Transportation Electrification, vol. 7, no. 4, pp. 2600-2610, Dec. 2021.
- [93] S. N. Afrasiabi and C. Lai, "Investigation of LC Filter Unbalance in an Inverter-Fed Permanent Magnet Synchronous Machine Drive," 2020 23rd International Conference on Electrical Machines and Systems (ICEMS), Hamamatsu, Japan, 2020.
- [94] M. R. Baiju, K. K. Mohapatra, R. S. Kanchan and K. Gopakumar, "A dual two-level inverter scheme with common mode voltage elimination for an induction motor drive," in IEEE Transactions on Power Electronics, vol. 19, no. 3, pp. 794-805, May 2004.
- [95] A. Zingariello, Z. Zhang and I. G. Griepentrog, "Analysis of leakage current paths in the power cable and reduction of shield common-mode current through common-mode choke," 2022 IEEE International Conference on Industrial Technology (ICIT), Shanghai, China, 2022.